

## ***Contents — K through L***

---

Martian Global-scale Seasonal CO <sub>2</sub> Change: Comparison of Geodetic Observations and Numerical Simulations <i>Ö. Karatekin, V. Dehant, and O. de Viron</i> .....	3172
Analysis of Atmospheric Mesoscale Models for Entry, Descent and Landing <i>D. M. Kass, J. T. Schofield, T. I. Michaels, S. C. R. Rafkin, M. I. Richardson, and A. D. Toigo</i> .....	3251
Winter Polar Conditions in the Mars Upper Atmosphere at Both the North and South Poles <i>G. M. Keating, M. Theriot, R. Tolson, S. Bougher, F. Forget, M. Angelats I Coll, and J. Forbes</i> .....	3282
Preliminary Thickness Measurements of the Seasonal Polar Carbon Dioxide Frost on Mars <i>N. J. Kelly, W. V. Boynton, K. Kerry, D. Hamara, D. Janes, I. Mikheeva, T. Prettyman, W. C. Feldman, and the GRS Team</i> .....	3244
“Breathing Soils” of Mars as Indicators of Subsurface Environment <i>A. Kereszturi</i> .....	3038
Isidis, Argyre and Hellas: Subsurface Indicators of Climate Changes <i>A. Kereszturi</i> .....	3082
Paleodischarge Estimation from Morphometry for Ancient Channels <i>A. Kereszturi</i> .....	3039
Gravity Evidence for Extinct Magma Chamber Systems on Mars <i>W. S. Kiefer</i> .....	3252
Behavior of Solid CO <sub>2</sub> on Mars: A Real Zoo <i>H. H. Kieffer</i> .....	3158
The Miniaturized Mössbauer Spectrometer MIMOS II of the Athena Payload for the 2003 MER Missions <i>G. Klingelhöfer, R. V. Morris, P. A. de Souza Jr., B. Bernhardt, and the Athena Science Team</i> .....	3132
Planetary Micro-End Effectors <i>S. M. Ko, T. C. Ng, K. L. Yung, C. H. Yu, and C. C. Chan</i> .....	3043
Morphology of the High-Latitude Mantle in Northern Plains on Mars <i>V.-P. Kostama, M. A. Kreslavsky, and J. W. Head</i> .....	3011
Enigmatic Surface Features of the South Polar Layered Deposits <i>M. R. Koutnik, S. Byrne, Z. Crawford, and B. C. Murray</i> .....	3134
Can Shoreline Processes on Mars Constrain Its Past Climate? <i>E. R. Kraal, E. I. Asphaug, and R. D. Lorenz</i> .....	3115
Methane Production by Methanogens in the Andromeda Environmental Chamber Under Conditions Approaching Those of the Martian Environment <i>T. A. Kral, D. W. G. Sears, P. H. Benoit, and M. S. Kareev</i> .....	3135

Mars Photochemistry: Weak Points and Search for Solutions <i>V. A. Krasnopolsky</i> .....	3002
Spectroscopy of Mars Atmosphere from Orbiting and Ground-based Observatories: Recent Results and Implications for Evolution <i>V. A. Krasnopolsky</i> .....	3003
North-South Slope Asymmetry on Mars <i>M. A. Kreslavsky and J. W. Head</i> .....	3010
Pressure Balance at Mars and Solar Wind Interaction with the Martian Atmosphere <i>A. M. Krymskii, N. F. Ness, D. H. Crider, T. K. Breus, M. H. Acuna, and D. Hinson</i> .....	3123
Volumetric/Morphometric Analysis of Impact Craters in the Northern Hemisphere Lowlands, Mars <i>K. Kurita and Y. Ogawa</i> .....	3096
Cerberus Plains Volcanism: Constraints on Temporal Emplacement of the Youngest Flood Lavas on Mars <i>P. D. Lanagan and A. S. McEwen</i> .....	3215
A Study of Meridiani Planum, Mars, Using THEMIS Data <i>M. D. Lane, P. R. Christensen, W. K. Hartmann, and the THEMIS Science Team</i> .....	3122
In Situ Neutron Spectroscopy on the Martian Surface: Modeling the HYDRA Instrument for Different Mission Scenarios <i>D. J. Lawrence, R. C. Elphic, W. C. Feldman, K. R. Moore, T. H. Prettyman, and R. C. Wiens</i> .....	3109
A Three-Dimensional Photochemical-Transport Model of the Martian Atmosphere <i>F. Lefèvre, S. Lebonnois, and F. Forget</i> .....	3114
Wind and Water at the Surface of Mars <i>C. B. Leovy and J. C. Armstrong</i> .....	3200
Non-Equilibrium Thermodynamic Chemistry and the Composition of the Atmosphere of Mars <i>J. S. Levine and M. E. Summers</i> .....	3055
4-D Model of CO <sub>2</sub> Deposition at North and South of Mars from HEND/Odyssey and MOLA/MGS <i>M. L. Litvak, I. G. Mitrofanov, A. S. Kozyrev, A. B. Sanin, V. Tretyakov, D. E. Smith, M. T. Zuber, W. V. Boynton, D. K. Hamara, C. Shinohara, R. S. Saunders, and D. Drake</i> .....	3040
Rationale for Seismic Measurements on Mars by a Single Station <i>Ph. Lognonné and W. B. Banerdt</i> .....	3225

**MARTIAN GLOBAL-SCALE SEASONAL CO<sub>2</sub> CHANGE: COMPARISON OF GEODETIC OBSERVATIONS AND NUMERICAL SIMULATIONS.** Ö. Karatekin, V. Dehant, O. de Viron, Royal Observatory of Belgium, 3 Avenue Circulaire, 1180 Brussels Belgium. (o.karatekin@oma.be).

**Introduction:** The Martian atmosphere exhibits an annual cycle in the CO<sub>2</sub> concentration; as much as 30% of the atmosphere takes part in seasonal exchange of mass between the atmosphere and the seasonal polar caps. The signature of this global-scale annual cycle can be found in the variation of gravitational field. This information can be used to estimate the global-scale seasonal mass and atmospheric pressure variations. With recent Mars Global Surveyor mission, global scale CO<sub>2</sub> change in polar caps has been estimated by several authors [1], [2], [3]. Although similar geodetic data are used, the results vary due to the differences in the approximations made. In the present study, these approaches are discussed and the polar mass changes are estimated. The results are compared with the values given by two Martian Global Circulation Models (GCM) as well as observations.

**Geodetic observations and Seasonal CO<sub>2</sub> Changes:** At seasonal time scales, the distribution of mass at the planet's surface varies because of atmospheric circulation and condensation/sublimation of polar caps. Time variation of zonal coefficients of gravity field can be estimated from Mars Global Surveyor (MGS) mission [3], [4]. In the present study, seasonal variations of the gravity field (expressed in dimensionless zonal harmonics of degrees 2 and 3, namely,  $\Delta J_2(t)$  and  $\Delta J_3(t)$  calculated from the MGS, pathfinder and Viking Lander data according to [3]), are employed.

Any variation in mass distribution gives rise to a change in the gravity field. From geodetic measurements, the variation of gravity field coefficients can be estimated. Changes in zonal harmonics are directly linked to the variations in surface mass density distribution ( $\Delta\sigma$ ) [5] by:

$$\Delta J_\ell(t) = -\frac{R^2}{M} \int \Delta\sigma(\Omega, t) P_\ell(\mu) d\Omega$$

In the equation above, R and M correspond to the mean radius and mass of the planet, P is the Legendre's polynomial of degree  $\ell$ ,  $\mu$  is the sine of latitude, and  $\Omega$  is the solid angle representing the colatitude and the latitude.

On the other hand, the mass change on each polar cap can be obtained from  $\Delta\sigma$ , by using the geometry of polar cap and its mass distribution.

**Results:** Seasonal polar mass changes and surface pressure variations are estimated. The outputs of GCM of Laboratoire de Météorologie Dynamique (LMD) [6]

and NASA Ames [7] are used as a comparison with the present results.

**Polar Cap Mass Change Estimation:** In figures 1 and 2, estimated seasonal CO<sub>2</sub> mass changes are plotted together with the outputs of GCMs. These preliminary results show fairly good agreement in general, despite the high uncertainties in geodetic measurements and the assumptions made on the geometry of polar caps [1]. The most important discrepancy occurs on the North Pole, during the summer season ( $90^\circ < L_S < 180^\circ$ ). Moreover, the CO<sub>2</sub> on the North Pole from GCMs starts to accumulate later with respect to the results derived from geodetic observations.

**Surface Pressure Estimations:** From the estimated total mass change in polar caps, global scale atmospheric pressure variation can be calculated. In figure 3, estimated mean surface pressure variation by the present method is compared with the GCM results of LMD. In agreement with the previous results, the comparison is fairly good, except for the northern summer season.

**Conclusions:** Seasonal mass change between the polar caps can be estimated by geodetic measurements. The preliminary results are in fairly good agreement. According to these results, the most important discrepancy occurs on the northern summer season. These discrepancies will be discussed in the paper.

**References:** [1] Karatekin O., Duron J., Rosenblatt P., Dehant, V. (2003), *EGS Abstract#06709*. [2] Smith D. and Zuber M. (2003) *EGS Abstract#07285*. [3] Yoder C. F., Konopliv A. S., Yuan D. N., Standish E. M., Folkner W. M., (2003) *Science*, 300, 299-303. [4] Smith D., Zuber M., Neumann A., (2001) *Science*, 294, 2141-2146. [5] Chao B. F. and Rubincam D. P. (1990) *JGR*, 95, B9, 14755-14760. [6] Forget F., Hourdin F., Fournier R., Hourdin C., Talagrand O., Collins M., Lewis S., Read P., Huot J.-P. (1999) *JGR*, 104, E10, 24155-24176. [7] Smith D., Zuber M., Haberle R. M., Rowlands D., Murphy J. (1999). *JGR*, 104, E1, pp. 1885-1896.

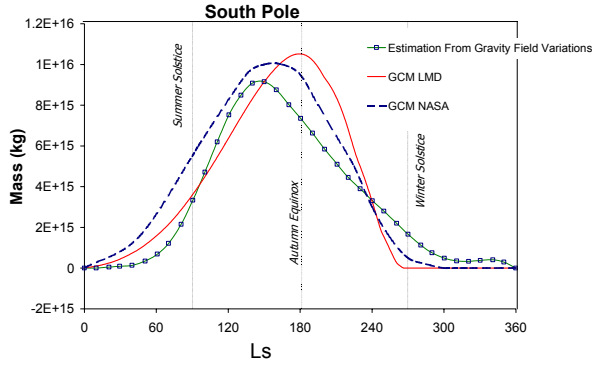


Figure 1. Seasonal mass change in south polar cap.

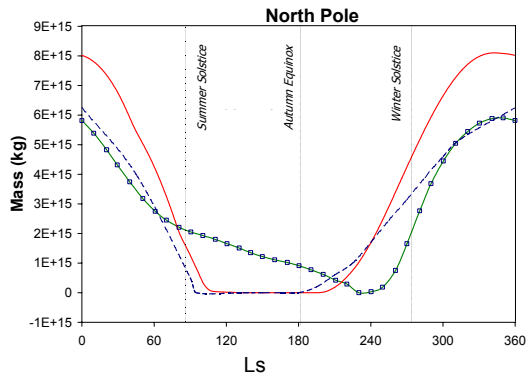


Figure 2. Seasonal mass change in north polar cap (Legend is given in Figure 1).

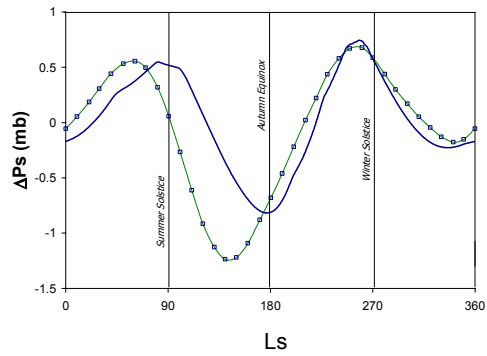
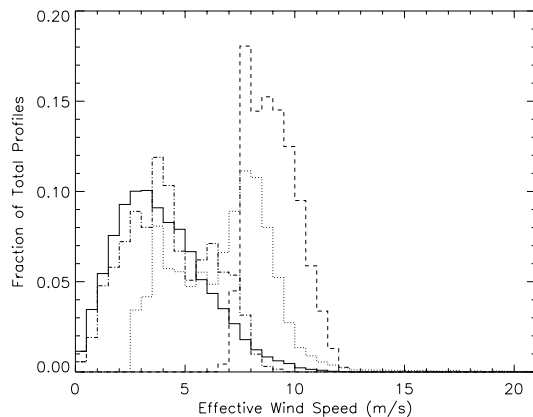


Figure 3. Mean surface pressure variation (Legend is given in Figure 1).

**ANALYSIS OF ATMOSPHERIC MESOSCALE MODELS FOR ENTRY, DESCENT AND LANDING.** D. M. Kass, J. T. Schofield, *Jet Propulsion Laboratory, California Institute of Technology, Pasadena, California, USA*, T. I. Michaels, S. C. R. Rafkin, *Southwest Research Institute, Boulder, Colorado, USA*, M. I. Richardson, *California Institute of Technology, Pasadena, California, USA*, A. D. Toigo, *Cornell University, Ithaca, New York, USA*.

Each Mars Exploration Rover (MER) is sensitive to the martian winds encountered near the surface during the Entry, Descent and Landing (EDL) process. These winds are strongly influenced by local (mesoscale) conditions. In the absence of suitable wind observations, wind fields predicted by martian mesoscale atmospheric models have been analyzed to guide landing site selection. Two different models were used, the MRAMS model [1] and the Mars MM5 model [2]. In order to encompass both models and render their results useful to the EDL engineering team, a series of statistical techniques were applied to the model results. These analyses cover the high priority landing sites during the expected landing times (1200 to 1500 local time). The number of sites studied is limited by the computational and analysis cost of the mesoscale models.

Four primary statistical measures were computed. They concentrate on the mean wind speed and on the vertical structure of the horizontal winds. Both aspects are potentially hazardous to the MER landing system. In addition, a number of individual wind profiles from the mesoscale model were processed into a form that can be used directly by the EDL Monte-Carlo simulations.



**Figure 1.** Model Mean Wind Speed Histogram. This figure shows a histogram of the effective wind speed (m/s) distribution for some of the landing sites. These are shown in 0.5 m/s bins as a fraction of the total number of profiles analyzed. The solid line is for the Meridiani Planum, the dotted line for the Gusev Crater site, the dashed line for the Isidis Basin site and the dash-dotted line for the Elysium Planitia site.

The effective mean wind speed is a measure of the horizontal speed the winds impart on the lander during its descent. It is computed for each wind velocity component (or direction) independently and then the two are combined to get the wind

speed. The effective mean wind is a weighted mean between  $\sim 300$  m and  $\sim 5$  km. An exponential weighting function that peaks at the bottom of the integral and decays with a  $\sim 2.5$  km scale height is used. The integration range and scale height are chosen to match the MER landing system. Figure 1 shows the binned statistics for the four prime candidate landing sites.

The vertical structure was studied in three ways. The first statistic was used to measure the long wavelength shear. A spacial Fourier transform of each profile from the surface to 5 km was performed. The mean ratio to an engineering standard was calculated for wavelengths between 5 km and 350 m. The second statistic studied was the mean TKE (Turbulent Kinetic Energy) over the turbulent boundary layer. This scaled and used as a proxy for the higher frequency shear not represented directly in the model profiles. The third and simplest statistic was to calculate the average thickness of the turbulent boundary layer at each landing site.

In order for the engineers to use the wind information in their EDL Monte-Carlo simulation, it was necessary to prepare actual wind profiles. This was done by randomly selecting mesoscale wind profiles from within the landing ellipse and extending them vertically to 50 km by using a profile from the Ames MGCM [3]. A high frequency turbulence component, whose magnitude and vertical structure were controlled by the TKE field of the specific profile, was also added via a Monte-Carlo type process. This was done to insure the effects of these higher frequencies would be captured in the engineering simulations.

The statistical and engineering analyses indicates that the Meridiani Planum and Elysium Planitia landing sites are probably safe. While the wind regimes are different at the two sites, they are equally safe within the uncertainty of the modeling. The winds at the Gusev Crater and Isidis Basin sites are more dangerous to the landing system. But they appear to be within the capabilities of the MER landing system. Finally, while there are some differences in the two models, the winds at the Melas Chasma landing site (and presumably other Valles Marineris landing sites) appear likely to be quite dangerous.

While the statistical parameters selected for these studies were primarily of engineering and landing safety interest, the techniques are potentially useful for more general scientific analyses. One interesting result of the current analysis is that the depth of the convective boundary layer (and thus the resulting energy density) appears to be primarily driven by the existence of a well organized mesoscale (or regional) circulation—primarily driven by large scale topographic features at Mars.

**References:** [1] Rafkin S. and T. Michaels, (in press) *JGR*. [2] Toigo A. and M. Richardson, (in press) *JGR*. [3] Joshi M. *et al.* (2000), *JGR* 105, 17,601-17,615.

## WINTER POLAR CONDITIONS IN THE MARS UPPER ATMOSPHERE AT BOTH THE NORTH AND SOUTH POLES

G. M. Keating, M. Theriot and R. Tolson, *George Washington Univ. Campus at NASA Langley, Hampton, VA, USA* ([g.m.keating@larc.nasa.gov](mailto:g.m.keating@larc.nasa.gov)), S. Bougher, *Univ. of Michigan, Ann Arbor, MI, USA*, F. Forget and M. Angelats i Coll, *Univ. of Paris, Lab. de Meteorologie Dynamique, Paris, Fr.*, and J. Forbes, *Univ. of Colorado, Boulder, CO, USA*.

The Mars Global Surveyor (MGS) z-axis accelerometer has obtained over 1600 vertical structures of thermospheric density, temperature, and pressure, ranging from 110 to 170 km, between Sept. 1997 and March 1999, compared to only three previous such vertical structures from Viking 1, 2, and Pathfinder (Tolson, et al., 1999). In November 1997, a regional dust storm in the Southern Hemisphere triggered an unexpectedly large thermospheric response at mid-northern latitudes, increasing the altitude of thermospheric pressure surfaces there by as much as 8 km and indicating a strong global thermospheric response to a regional dust storm (Keating, et al., 1998).

From analysis of the MGS accelerometer data, enormous planetary scale waves have been detected in the Martian thermosphere between 60°N and 60°S. Fourier analysis of the wave structure reveals high amplitude waves 2 and 3 which appear to remain at nearly constant longitude between  $\pm 60^\circ$  latitude when viewed near 3 PM (Keating, et al., 2001, Bougher, et al., 2001). However, measurements near 3 AM show evidence of essentially a phase reversal in wave 2 (Keating, et al., 2001). Taking into account the near sun-synchronous orbit it appears that these waves are principally non-migrating tides propagating to the east. Studies by Wilson et al. (Wilson, 2002) and Forbes et al. (Forbes, et al., 2002) indicate the wave 2 component is principally an eastward propagating diurnal wave 1 which rotates around Mars in the opposite sense of the sun once per day (the wave 1 Kelvin wave, which principally results from the interaction of tides and topography). Analysis of Thermal Emission Spectrometer (TES) MGS data near 30 km (Wilson, 2002) indicates a similar phase to this wave at 30 km (Wilson, 2002) and thus the wave appears to propagate up from below into the thermosphere. The observed wave 3 may be a combination of an eastward propagating, semi-diurnal wave 1 and the eastward propagating, diurnal wave 2 (basically the wave 2 Kelvin wave). Both the observed wave 2 and wave 3 maximize near the equator. These results give further evidence of coupling between the lower and upper atmosphere.

The Mars Odyssey 2001 (M01) Spacecraft was placed into orbit about Mars in September 2001. Aerobraking was performed from then until January

2002 to circularize the M01 orbit. The spacecraft carried triaxial accelerometers, which were used to safely perform aerobraking and to continue exploration of the detailed properties of the upper atmosphere, which had begun with the Mars Global Surveyor accelerometer measurements. The accelerometers were used to measure atmospheric density, and from the vertical structures measured on both inbound and outbound trajectories the scale height, temperature and pressure were determined. Altogether 600 vertical structures were obtained ranging from 95 km to above 170 km. Measurements were obtained for the first time near the North Pole and also the first measurements were obtained on the night-side in the Northern Hemisphere. Temperatures near 110 km were discovered to increase with latitude maximizing near the North winter pole, apparently due to dynamical heating (Keating, et al., 2002). This result is contrary to the MarsGram and MTGCM models used for Odyssey aerobraking, where model temperatures are predicted to minimize near the winter pole. For example, maximum temperatures near the North winter pole at 100 km were observed to be near 200 K while MTGCM temperatures were predicted to be near 100 K. However, a winter polar warming is predicted by the European Mars GCM (Forget, et al., 1999) at both the North and South Poles in local winter at high altitudes. The altitudinal variations and high latitude diurnal variations of temperature near the North Pole also appear to be in fair accord with the Forget et al. model. Apparently the upper atmosphere North polar winter warmings may result from adiabatic heating from the subsiding branch of the cross-equatorial meridional circulation from the Southern Hemisphere summer. The only measurements of the Southern Hemisphere winter polar upper atmospheric temperatures were obtained from accelerometers aboard the Mars Global Surveyor. These measurements do not show winter polar warmings, but minimum temperatures near the winter South Pole more in accord with radiative equilibrium, and more in accord with the MTGCM model. Apparently the summer-to-winter cell supplying dynamical heating to the North winter pole near perihelion is much stronger than the summer-to-winter cell supplying dynamical heating to the South winter pole

near aphelion. The stronger dynamical heating during the North polar winter may result from being near perihelion where the closer sun and stronger dust activity may strengthen the meridional cell.

Previously, intense warming of the winter polar atmosphere was observed in the lower atmosphere (~25km) by the Infrared Thermal Mapper Instrument (IRTM) aboard the Viking orbiters during the onset of the 1977b global dust storm at northern hemisphere winter solstice (Jakosky and Martin, 1987; Wilson, 1997). The 2001 global dust storm had nearly subsided before the Odyssey aerobraking period and occurred closer to equinox than solstice and yet North winter polar warming occurred in the upper atmosphere (~100km). Therefore, the warmings may be more related to the season near perihelion.

Figure 1 shows the complementary nature of the Mars Global Surveyor and Mars Odyssey 2001 accelerometer measurements and the measured global latitudinal/seasonal and diurnal variations in the Martian upper atmosphere at 130 km. The data points in green represent a 35 point running mean of the MGS Phase 1 data (fall/winter, Northern Hemisphere). The data points in blue represent MGS Phase 2 data (spring/summer Northern Hemisphere and fall/winter Southern Hemisphere). The data points in red represent the Odyssey 2001 data (fall/winter near North winter pole). Minimum densities at highest latitudes occur in winter near aphelion.

Table 1 shows various systematic variations which we have now detected from the accelerometer experiments aboard Mars Global Surveyor and Mars Odyssey.

Table 2 shows the number of in situ measurements which have been made of vertical structures of the Mars upper atmosphere.

## References

S.W. Bougher, G.M. Keating, et al., The upper atmosphere wave structure of Mars as determined from Mars Global Surveyor Accelerometer, EOS, Trans, AGU, supplement, page F717, 2001.

J.M. Forbes, G.M. Keating, et al., Nonmigrating tides in the thermosphere of Mars, In Press, J. Geophys. Res., Planets, 2002.

F. Forget, et al., Improved general circulation models of the Martian atmosphere from the surface to above 80 km, J. Geophys Res., 104, 24155, 1999.

B.M. Jakosky and T.Z. Martin, Mars:North-polar atmospheric warming during dust storms, Icarus,72,528,1987.

G.M. Keating, et al., The structure of the upper atmosphere of Mars: In Situ accelerometer measurements from Mars Global Surveyor, Science, 279, 1672, 1998.

G.M. Keating, et al., Persistent planetary-scale wave-2 and wave-3 density variations observed in Mars upper atmosphere from MGS accelerometer experiment, Proceedings of European Geophysical Society, 78, 229, March 2001.

G.M. Keating, et al., Detection of North Polar winter warming from the Mars Odyssey 2001 accelerometer experiment, Proceedings of the 34<sup>th</sup> Scientific Assembly of the Committee on Space Research (COSPAR) and the World Space Congress, 142, 2002.

R.H. Tolson, G.M. Keating, et al., Application of accelerometer data to Mars Global Surveyor aerobraking operations, J. of Spacecraft and Rockets, 36, No. 3, 1999.

R.J. Wilson, A general circulation model simulation of the Martian polar warming, Geophys. Res. Lett., 24 (2), 123, 1997.

R.J. Wilson, Evidence for nonmigrating thermal tides in the Mars upper atmosphere from the Mars Global Surveyor accelerometer experiment, Geophys Res. Lett., 29, (7), 10.1029 GL013975, 2002.

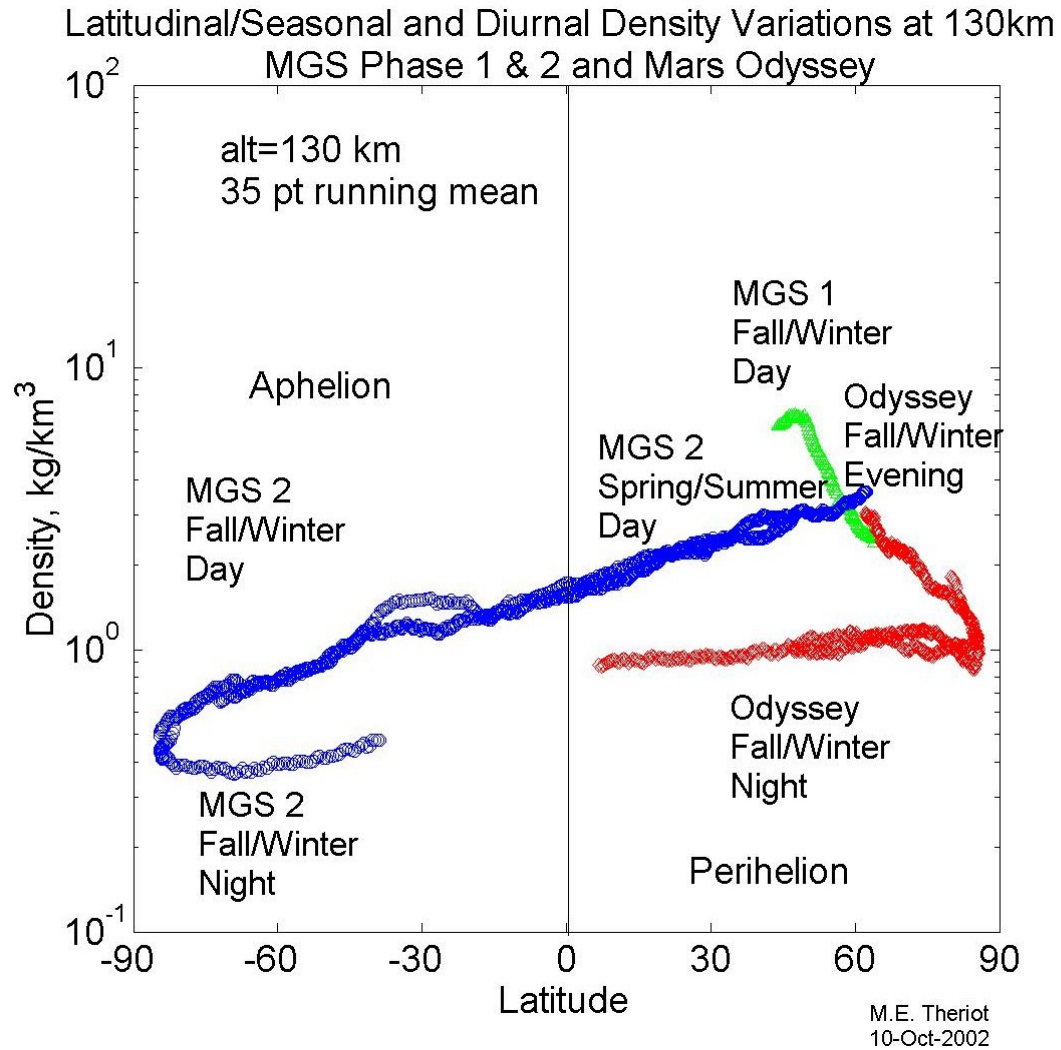


Figure 1

## Systematic Thermospheric Variations Detected From MGS and Mars Odyssey Accelerometer Experiments

- Latitudinal/Seasonal
- Planetary Scale Waves (Including Wave 1 Kelvin Wave)
- Dust Storm Response
- Northern vs. Southern Hemisphere
- Aphelion vs. Perihelion
- North Winter Polar Warming
- Diurnal
- Global and Vertical Temperature and Density Structure

Table 1

## EXPLORING THE MARS UPPER ATMOSPHERE

<u>Spacecraft</u>	<u>Vertical Structures</u>
Viking 1	1
Viking 2	1
Pathfinder	1
Mars Global Surveyor Accelerometer	1600
Mars Odyssey Accelerometer	600

Table 2

**PRELIMINARY THICKNESS MEASUREMENTS OF THE SEASONAL POLAR CARBON DIOXIDE FROST ON MARS.** N. J. Kelly<sup>1</sup>, W. V. Boynton<sup>1,2</sup>, K. Kerry<sup>1</sup>, D. Hamara<sup>1</sup>, D. Janes<sup>1</sup>, I. Mikheeva<sup>1</sup>, T. Prettyman<sup>3</sup>, W. C. Feldman<sup>3</sup> and the GRS team. <sup>1</sup>Lunar and Planetary Lab, Univ. of Arizona, Tucson AZ 85721, <sup>2</sup>Department of Planetary Science, Univ. of Arizona, Tucson AZ 85721, <sup>3</sup>Los Alamos National Laboratory, Los Alamos N.M.

### Introduction:

The exchange of carbon dioxide between the atmosphere and the polar caps on Mars creates a seasonal cycle of growth and retreat of the polar caps. CO<sub>2</sub>, the major component of the Martian atmosphere, condenses in the polar regions of the planet during the winter seasons, precipitating as CO<sub>2</sub> frost. It then sublimates during the spring and summer seasons in response to solar radiation. Nearly 30% of the atmosphere takes part in this seasonal process [1]. While the northern seasonal CO<sub>2</sub> frost appears to dissipate completely, the south pole has a thin, permanent cover of dry ice over the residual cap. The underlying residual caps are believed to contain large quantities of water ice. We have attempted here to quantize the time-dependence, spatial extent, and thickness of the polar carbon dioxide frost through the use of gamma-ray data measured by the Gamma-Ray Spectrometer (GRS) instrument suite on Mars Odyssey. After launch on April 7, 2001, Mars Odyssey reached Mars for orbital insertion and began mapping several months later on February 18, 2002. The study discussed here includes data received from solar areocentric longitude (L<sub>s</sub>) 329° through 135° (February, 2003). Measurements and analyses have been done for the north and south poles, for latitudes poleward of ±65°, using the hydrogen neutron-capture gamma-ray line at 2.223 MeV.

The concentration of an element within the top few tens of centimeters of the surface is proportional to the flux of the gamma-rays emitted at the element's characteristic energy [2]. Variations in the thickness of the carbon dioxide frost over time can be approximated by observing the attenuation of this signal caused by increases and decreases in CO<sub>2</sub> coverage throughout the Martian seasons.

To first order, we can estimate the seasonal frost thicknesses by assuming that the intensity of hydrogen gamma-rays at the surface of the regolith does not vary with thickness of CO<sub>2</sub> frost above it. This allows us to employ the Beer-Lambert Law, which states that the radiation absorbed per unit length in a medium depends at any wavelength only on the incident radiation intensity:

$$\frac{dI(\lambda)}{dx} = -\mu I(\lambda) \quad \text{or} \\ I_t = I_0 e^{-\mu t}$$

t: thickness of attenuator (CO<sub>2</sub> polar cap frost)

μ: attenuation/absorption coefficient, dependent on wavelength (from photon cross-section database)

I<sub>0</sub>, I<sub>t</sub>: initial (incident) and final (transmitted) intensities

The attenuation coefficient (μ) for the 2.223 MeV hydrogen line through carbon dioxide is 0.0420 cm<sup>2</sup>/g. Using this value and the gamma-ray flux observed for a frost-free versus CO<sub>2</sub>-covered surface, we obtain an approximation of the seasonal polar frost thickness in g/cm<sup>2</sup>. (Note that depths are given in terms of the mass abundance of the column of CO<sub>2</sub> above the surface to avoid assumptions regarding the density of the column.) Additionally, we employ a model of the change in atmospheric thickness with time based on the Ames Research Center Global Circulation Model (ARC GCM), and we correct the hydrogen gamma-ray flux for the modeled change in the atmosphere.

The results can be compared to information about the polar environment previously inferred from the ARC GCM and to data accumulated one Martian year earlier by the Mars Orbiter Laser Altimeter (MOLA) aboard the Mars Global Surveyor (MGS) [3].

### Data Processing and Analysis:

The process by which we go from counts in the GRS instrument [4] to elemental concentrations on the surface of Mars and then from concentration variations to seasonal carbon dioxide frost thicknesses is somewhat complicated. The flux of gamma-rays (as well as neutrons) depends on the subsurface composition of the regolith, and the signal is detected from a median depth of approximately 20 g/cm<sup>2</sup>. Every 19.2 seconds, the GRS returns a gamma spectrum (along with several neutron spectra) collected along 59 kilometers of orbital arc, or one degree of motion, over the surface of Mars. Statistics are improved by binning the data over regions of interest.

Since converting from gamma-ray counts directly to surface concentrations is not possible, we perform a series of forward calculations that predict expected gamma-ray counts based on a priori assumed planetary abundances and compare these model results to observed results to derive a measure of elemental concentrations. We use a Monte Carlo Neutral Particle code (MCNPX) to predict the gamma-rays leaving the surface of Mars [5], [6]. These predictive models initially assume that Mars has the composition of the soil measured by the Mars Pathfinder Alpha Proton X-Ray Spec-

trometer (APXS) [7]. We further assume that the signal comes from a large footprint defined as the circular region on Mars from which 99.9% of the signal would come when approximating the planet as a sphere with uniform atmosphere and no topography. Within each footprint, a grid of 0.5 degree cells is defined over the surface to allow the specification of various compositions, altitudes, and atmospheric thicknesses. On the order of 10,000 cells are processed for each spectrum yielding expected gamma-ray counts. We then compare measured counts to predicted counts and determine relative concentrations for various elements as functions of latitude and longitude on the planet.

From the concentration profiles, attenuation effects due to the seasonal CO<sub>2</sub> frost can be investigated. Although we can obtain approximations from the basic Beer-Lambert Law calculations mentioned above, the effect of the CO<sub>2</sub> can increase the flux of thermal neutrons [3], and we cannot necessarily assume that the flux of gamma-rays under the frost does not vary with the frost thickness. Incorporating various models for the flux of hydrogen gamma-rays through a range of different thicknesses of CO<sub>2</sub> frost covering the regolith, we can plot the ratio of flux through a range of thicknesses of CO<sub>2</sub>-frost to that when no CO<sub>2</sub> frost is present (i.e. intensity ratio) to obtain the equations below.

*Northern model:*

$$\text{Intensity ratio} = e^{-0.042633 * \text{thickness}} \quad \text{or} \\ \text{Thickness (g/cm}^2\text{)} = -54.0094 * \log(\text{intensity ratio})$$

*Southern model:*

$$\text{Intensity ratio} = e^{-0.048288 * \text{thickness}} \quad \text{or} \\ \text{Thickness (g/cm}^2\text{)} = -57.6844 * \log(\text{intensity ratio})$$

These models take into account both the efficiency of the detector as a function of angle and the effect of peaking of the emission in the upward direction with thicker CO<sub>2</sub> frost, leading to the given relationships between carbon dioxide thickness and the attenuation ratio. These relationships hold for all thicknesses up to 80 g/cm<sup>2</sup> after which the gamma-ray flux is essentially completely attenuated.

### **Spatial and Temporal Dependence of the Seasonal Polar CO<sub>2</sub> Frost Caps:**

*Thickness versus latitude.* Preliminary plots incorporating hydrogen gamma-ray (2.223 MeV) flux data binned over 5° by 360° latitude bands at both north and south poles are plotted in Figures 1a and 1b using the aforementioned procedure. Column density in g/cm<sup>2</sup> is plotted for latitudes poleward of approximately ±60°. Lower limit values, given by the triangular data points, are employed when error bars become excessively large due to near total attenuation of the transmitted

gamma-ray signal and signify the lowest value within the two-sigma range of calculated CO<sub>2</sub> seasonal frost thickness.

For the north pole, a weighted average of the hydrogen gamma-ray flux seen during the northern summer ( $L_s = 90^\circ - 135^\circ$ ) is taken as the basis for minimal/no frost coverage. The corresponding maximum 2.223 MeV line strength creates the basis for all attenuation ratio calculations. Similarly, a weighted average of data in the time interval:  $L_s = 345^\circ - 15^\circ$  during the southern summer creates the frost-free basis for all southern CO<sub>2</sub> frost thickness measurements.

As sublimation of carbon dioxide to the atmosphere occurs on one pole, the growth of the CO<sub>2</sub> cap occurs on the opposite pole. During the time period of this study, the retreat of the northern seasonal polar frost is observed, as the southern CO<sub>2</sub> cap continually grows. Retreat/growth takes place at a fairly constant rate as the seasons progress. As expected, greater frost depth is observed at increasingly poleward latitudes for both hemispheres.

For low values of column density, the most sensitive measurements are obtained from gamma-ray studies. As the thickness increases and the signal approaches full attenuation, epithermal neutrons provide the most effective frost measurements (see [3] for detailed CO<sub>2</sub> frost depth analysis using neutron data). In any event, the maximum frost depth inferred from GRS data before encountering this limit is approximately 75 g/cm<sup>2</sup> in the north, and 65 g/cm<sup>2</sup> in the south (lower bounds).

*Thickness versus  $L_s$ .* The growth and retreat of the seasonal carbon dioxide frost can also be plotted at specific latitudes as a function of  $L_s$ . Figures 2a and 2b show CO<sub>2</sub> thickness plotted for latitudes from ±62.5° poleward. Once again, triangular data points represent the lower limit within error bars of seasonal frost thickness, corresponding to near total attenuation of the H gamma-ray signal. Note that we reach this limit at lower column density values in the northern hemisphere than in the southern due to greater atmospheric thickness and attenuation over the northern lowlands.

As shown in the previous plots, frost depth at any given date increases as we move poleward. In addition, the CO<sub>2</sub> cap coverage continually decreases (increases) over time for any specific latitude band beginning at approximately  $L_s = 0^\circ$  in the north (south) pole.

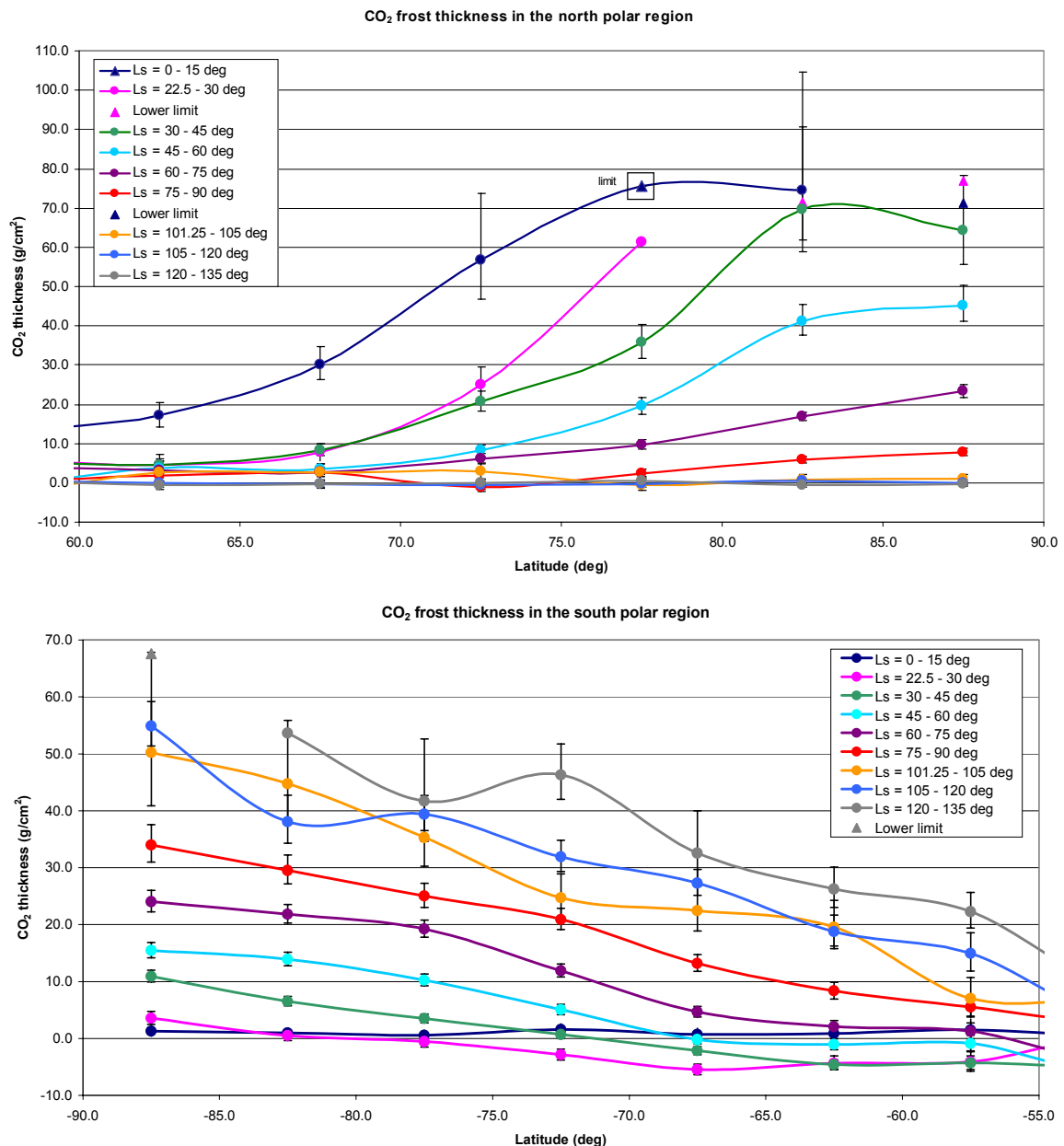
### **Future work:**

The data shown here represent our understanding and evaluation of the seasonal polar CO<sub>2</sub> frost cycle at the time of abstract submittal. By the July conference date, we expect to have accumulated and analyzed three more months of GRS data.

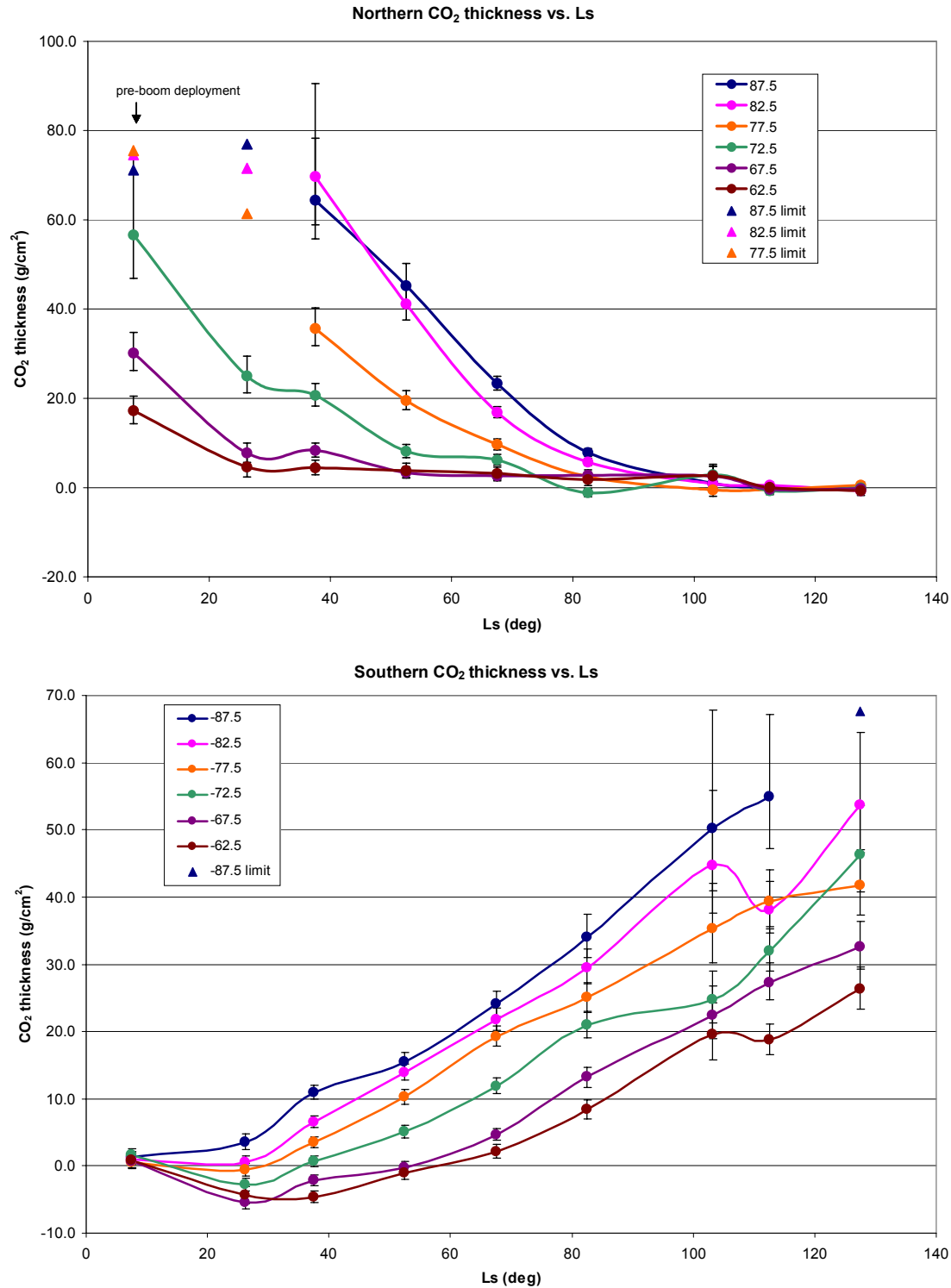
It is currently near the end of the northern summer, so during this time we anticipate observing the growth of seasonal  $\text{CO}_2$  frost on the north pole of Mars, as well as the corresponding sublimation of  $\text{CO}_2$  from the southern cap.

**References:** [1] James, P.B. et al, (1992) in *Mars*, Kieffer, H.H. et al, eds., 934-968. [2] Reedy, R.C. et al, Gamma-rays in a spectrum from the mars odyssey gamma-

ray spectrometer, abstract (2003). [3] Feldman, W.C. et al,  $\text{CO}_2$  frost thickness on Mars during Northern Winter and Spring, manuscript (2003). [4] Boynton et al, (2003) *Space Sci. Rev.*, in press. [5] Prettyman, T.H. et al, (2002) *LPSC XXXIII*, Abstract #2012. [6] Waters, L.S. Ed., (1999) MCNPX User's Guide, Los Alamos National Laboratory, document LA-UR-99-6058. [7] Wänke, H. et al, (2001) *Space Sci. Rev.*, 96, 317-330.



Figures 1a and 1b.  $\text{CO}_2$  seasonal frost thicknesses for various time intervals ( $L_s = 0^\circ - 135^\circ$ ) as a function of northern (fig.1a) and southern (fig.1b) latitudes. Values are derived from gamma-ray flux data (2.223 MeV) from  $5^\circ$  by  $360^\circ$  latitude bands. Lower limits designated by triangular data points are employed when uncertainty is large due to near total attenuation of the transmitted gamma-ray signal and represent the lowest thickness values within the error range.



Figures 2a and 2b. CO<sub>2</sub> seasonal frost thicknesses at specific northern (fig.2a) and southern (fig.2b) latitudes for Ls = 0° - 135° calculated from 5° by 360° latitude bands of 2.223 MeV hydrogen gamma-ray flux data. Lower limits designated by triangular data points are employed when uncertainty is large due to near total attenuation of the transmitted gamma-ray signal and represent the lowest thickness values within the error range.

**“BREATHING SOILS” OF MARS AS INDICATORS OF SUBSURFACE ENVIRONMENT.** A. Kereszturi<sup>1</sup>  
(<sup>1</sup>Department of Physical Geography, Eötvös Lorand University of Sciences, Pázmány sétány 1/C, Budapest, H-1088, Hungary, E-mail: krub@freemail.hu).

**Introduction:** Important information hides deep below the surface of Mars for planetology and astrobiology. Our knowledge would be greatly improved on the planetary evolution with physical and chemical informations from the subsurface especially on the proposed deep water layer, hydrothermal systems, possible subsurface habitats, volatile reservoirs, paleoclimate. Because the impossibility of deep drill on Mars in the next decades we suppose one unexpensive method for the analysis of subsurface environment. In this work the theoretical bases and the possible results are summarized of the “breathing process”.

**The model of the “breathing”:** Our model is based on the isothermal volume changes of subsurface gases because of climatic variations in the atmospheric pressure. This can cause expansion and contraction of the subsurface gas and gas currents. We analysed the possibility and extent of this “breathing” process with the following factors:

*I. Pressure change:* We have data on the annual surface pressure variations from the Viking landers, and daily variation data from Vikings and MPF. These are local observations and differences can take place for various latitude and height. The observed pressure changes according to the surface landers are: Viking-1 6,7-8,8 mbar Viking-2: 7,5-9,7 mbar (annually), MPF observed values between 6,4-6,8 mbar (daily) [1]. The day to day pressure variability is low during summer and high during fall and winter, because of atmospheric fronts [2,3]. During great dust storms the daily pressure variation is higher because of the temperature increase by the absorbing of dust.

*II. The subsurface porosity:* We have only indirect informations on the subsurface porosity. Based on the martian meteorites we have porosity values: Nakhla 5,7%, Chassigny 3,2%, shergottites 2,7-2,1%. [3]. Based on the waterice estimation from the GRS on Mars Odyssey at high latitude there is 60%±20% of water ice by volume [4]. The water ice content can hint to the porosity of the near surface matters if we suppose that most of the ice is physically bounded in the regolith. Viking-1 density estimations for drift material without water ice content are suggest 54±6%, for blocky material 36±16% of pore volume [5]. The meteoritic bombardment during the Noachian have been gardened the upper crust. The porosity strongly depends on the later unknown cementation processes which can reduce the original porosity. For the “breathing” we can use only effective porosity (vol-

ume of interconnected pores) which could be smaller than absolute porosity, see examples below from the Earth:

Rock types	Eff. porosity
Sandstone	0.1-0.35
Limestone	0.1-0.5
Shale	0.5-0.8
Clay	0-0.05
Silt	0.03-0.19
Medium sand	0.15-0.32
Fine sand	0.01-0.35
Course gravel	0.15-0.30
Mafic rocks, fissured, weathered	0.01-0.4
Crystalline rocks	0.0005

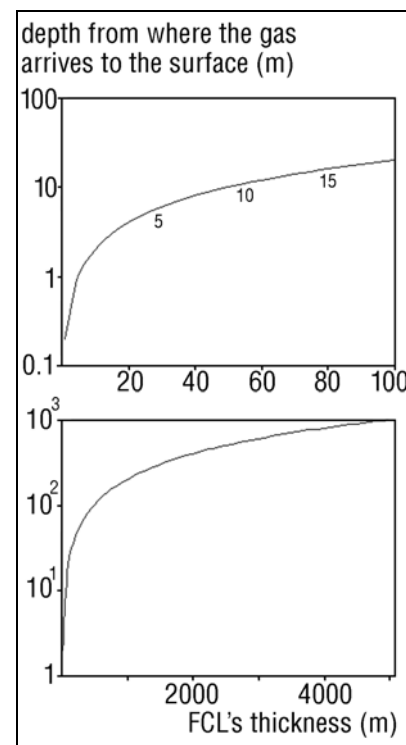


**Fig. 1.**

#### Depth from where gas arrives to the surface

In generally inside unweathered mafic rocks the effective porosity is around 0.19-2.77% [6]. We used in our model different values for the volumes of the communicating pores. We marked with FCL (“freely communicating layer”) that regolith layer which is in free contact with the atmosphere (Fig. 1.).

*III. Volume variations of the gases:* We modeled the volume variations of the gases with ideal gas law and isothermal volume changes under constant temperature taken to be equal to the surface average temperature (temperature changes due to insolation could be low below the surface, because of the low heat transport capacity especially at the dust covered places). The geothermal gradient for Mars could be near to 0.015 K/m [7]. We excluded the annually and daily temperature variability in the subsurface zones.

*IV. Atmosphere-subsurface communication:* We suspected that the atmosphere communicates freely with the subsurface gas phase (free intergranular continuous down- and upward tracks) and did not take into account any friction between the moving gas and the solid intergranular surfaces of the regolith.

*V. Supposed gas currents:* Because of the volume changes we suppose periodic gas currents exist inside the regolith, downward currents during surface pressure increase and upward currents during decrease.

*VI. Possible errors in the model:* 1. The vertical distribution of the effective porosity has strong effect on the velocity of the gas current at certain observing point. In the case of homogeneous effective porosity distribution the gas current's velocity is the smallest at any point. When the near surface effective porosity is low (deep below is greater) gas current's speed near the surface will be substantially higher – although the total volume of the wandering gas is the same. 2. We have no information on the effective porosity which is very important factor. The greatest uncertainties we meet at the possible subsurface chemical cementation.

**Discussion:** 1. The observed *annual pressure variation* on the surface is around 2.5 mbar. The subsurface gas increases its volume up to 1.25 times of the smallest volume during one martian year and contracts to the original volume. Because the condensing out volume of the atmospheric CO<sub>2</sub> differs on the two hemispheres we have two periods of up- and two downward gas currents during one martian year. The most intensive currents happen during Mars approaches perihelium when the upper mentioned change realizes during about 100 days. In the case of 1.25 times expansion or contraction, in homogeneous porosity distribution we can find that during the lowest surface pressure the gas arrives to the surface originated from 80% of the depth of the FCL. The depth depends on the FCL's thickness and not on the effective porosity. Values for different FCL's thickness values are visible on Fig. 1. The values can be extrapolated to greater and less homogeneous FCLs too. The gravity driven compaction probably decreases the porosity about 25-30% of that measured in 200-400 m depth, but this is very uncertain. 2. *Daily pressure*

*variation:* Based on the observations the daily variation is up to 0.5 mbar causing about max. 5% volume changes resulting weaker breathing which could not be neglected. 3. *Long term pressure variation:* It is supposed that Mars had undergone strong climate changes when gas previously stored in the subsurface outgassed into the atmosphere. During this periods the existence of the fluctuation depends on the asymmetry of polar caps in the past which is little known. The volume of the gas which takes part in the periodic current is visible on Fig. 2.

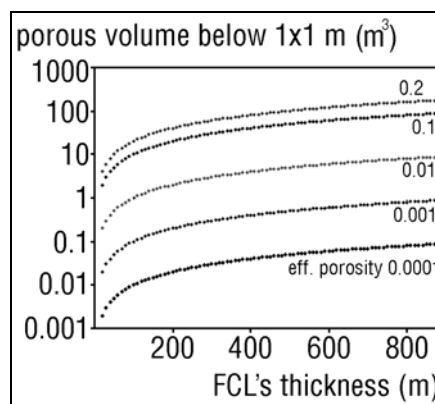


Fig. 2. Volume of gas takes part in the currents

**Supposed observing method:** We suppose the following in-situ methods for the analysis. All of the analysis would be carried out at least at two places at the same time: above the surface (at 1-2 cm height) and with a drilled probe 60-100 cm below the surface. The probe have be able to measure the pressure, temperature, gas composition, oxygen and carbon isotope ratios. It is possible that with a special vertical channel in the probe to measure vertical gas current speed. The measurement should be realized at least two martian years for control measurements too. We suggest the following places for the analysis where loose and weakly confined matter can be present: 1. Ancient talus slopes, lacustrine deltas and other water related sediments, because of their high primary porosity (if great cementation have not happened) and the possibility to find gas producing sediments. 2. Locations with low height to get as near as it is possible to any deep subsurface water layer. We think the best place is the bottom of Hellas where water related sediments could be accumulated under relative great geothermal gradient and have direct contact with the atmosphere.

**Possible results:** Theoretically we can account on the following phenomena and their observations:

1. *Transport of the oxidants:* It is supposed that the aggressive oxidants in the martian soil are produced mainly by solar UV radiation. The downward gas cur-

rent takes any kind of gas phase oxidants far below the surface, producing a thickened weathered layer.

2. *Volatile transport, evaporation and condensation:* during the upward gas current because of the geothermal heat the gas arrives into somewhat colder environment. Near to the surface the surface temperature have effect on the condensation too. During the downward track because of the somewhat growing temperature of the gas became more and more dry and can cause sublimation again. These can cause periodic sublimation-condensation and small vertical lifting which can take part in the homogenization of chemistry. Gas currents dries the upper part of the regolith, the transported volatile mass depends on the temperature and saturation of the gas which can hint on the characteristics of the subsurface sinks [8]. Chemical changes because of the migration of differently saturated gas volumes can realize in the subsurface. Based on a theory the photochemically produced  $\text{CO}$ ,  $\text{O}_2$ ,  $\text{H}_2$  can be the energy source of subsurface habitats [9]. The “breathing” can take these downward too.

3. *The composition differences* can suggest to subsurface differences in the chemistry. It can be supposed that the near surface environment is somewhat different in chemistry than the surface because of the differences in the weathering.

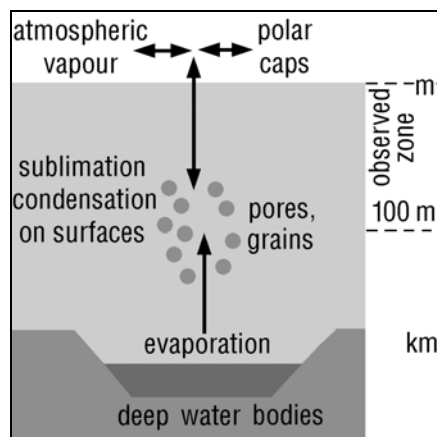


Fig. 3. Possible sinks and locations of fractionation

5. *Isotop analysis* can help in the reconstruction of volatile transport, groundwater/ice dating and paleoclimate. Isotopic fractionation was observed under Mars-like p/T laboratory environment [10,11]. The supposed repeated climate changes could cause differences in the isotopic ratio between the atmospheric, surface, subsurface ice and possible subsurface liquid water. During the vertical gas currents the gas transports volatiles from differently fractionated reservoirs (Fig. 3.). Because of the vertical gas currents in the regolith no distinct isotopic layering is probable but

diffuse, thick layers. The reconstruction of the source region is difficult but not impossible because the deep regions can taken to be closed system. Differences in the oxygen isotope ratios between the atmosphere and the gas originated from deep below the surface could show to the presence of deep water layer and the depth of it – as a very rough approach. It is a basic question to determine standard values for isotope ratios like on Earth (SMOW, PDB), the current ratio in the atmosphere and SNC meteorites could be an important standard anyway. [12,13,14].

**Observations in the near future:** With the following spaceprobes it is possible to try to observe some aspects of the supposed “breathing” 1. On Beagle-2 the GAP of Mole can analyse the presence of methane and C isotopes [15]. 2. The MARSIS radar sounding experiment can hint to the subsurface ice distribution. This coincides with the depth analysed by the breathing method and help in the better determination of certain subsurface ice layers [16]. Observation of the “breathing” could have information on the origin of the volatiles in gullies and dark slope streaks [17]. We suggest tests with the current martian soil simulation chambers for gas driven transport of the volatiles [19,20]. A long term operating subsurface gas analyser with duration at least one or two martian years with already tested experiments could be an inexpensive step toward future deep drill activity.

**Acknowledgment:** This work was supported by the Polaris Observatory and the Hungarian Astronautical Association.

**References:** [1] Barnes J.R., Bennett S. (1997) *JGR*, 90, 1151-1154. [2] Tillman, J.E. et al. (1993) *JGR* 84, 10963-10971 [3] Frédéric H. et al. (1993) *Journal of Atm. Sci.* 50, 3625-3640. [4] Annual Meeting of the GSA (2002) No. 32-4. [5] Boyton W.V. et al. (2002) *Sci. Express* 30<sup>th</sup> May 2002 1-10. [6] Moore H.J., Jakosky M.B. (1989) *Icarus* 81,164. [7] Porosity characteristics of mineralized and nonmineralized rocks, Geol. Surv. of Canada, Current Res. 2001-C3. [8] Clifford S.M., Hillel D. (1983) *JGR* 88, 2456-2474. [9] Weiss B.P et al. (2000) 97. 1395-1399. [10] Pollack J.B. et al. (1987) *Icarus*, 71. 203-224. [11] Eiler J.M., Kitchen N. (1999) LPSC XXX<sup>th</sup>#1309. [12] Rahn T., Eiler J.M, (2000) LPSC XXXI<sup>th</sup>#1933. [13] Emiliani, C. (1966) *Science* 154: 851-57. [14] Kendall C., McDonnell J.J. (Eds.) *Isotope Tracers in Catchment Hydrology* (1998), Elsevier Science B.V., Amsterdam. [15] Eiler J.M. (2000) *Geochem. et Cosmochem Acta* 64, no. 4: 733-746. [16] Richter L. et al. (2003) *Geophys. Res. Abs.* Vol 5. 11735. [17] Schmidt E. et al. (1999) *ESA Bulletin* Vol 98. June 1999. [18] Motazedian T. (2003) LPSC XXXIV<sup>th</sup> #1840. [19] Sears D.W.G. et al. (2003) LPSC XXXIV<sup>th</sup> #1035. [20] Allen C.C. et al. (2002) *Planet. Space Sci.* 50. 821.

**ISIDIS, ARGYRE AND HELLAS: SUBSURFACE INDICATORS OF CLIMATE CHANGES.** A. Kereszturi<sup>1</sup> (<sup>1</sup>Department of Physical Geography, Eötvös Lorand University of Sciences, Pázmány sétány 1/C, Budapest, H-1088, Hungary, E-mail: krub@freemail.hu).

**Introduction:** The Mars Express and Beagle-2 lander gives possibility for detailed orbital analysis of the subsurface ice at the great basins with GPR, and in-situ analysis at the Early-Noachian aged Isidis Planitia [1]. In this work we summarize implications for the subsurface ice distribution and one possibility to use it as indicator of the last great climate change. This could hold information on planetary evolution [2,3].

**Basic aspects:** Isidis planitia is interesting among the great basins on Mars because of the following reasons: 1. The basin is closed in the subsurface zone based on its contact toward the Northern Plains. 2. Isidis is nearly same sized like Argyre but filled with basaltic cover. 3. At the edge of the basin two stratigraphic units are in visible contact: the old cratered upland and the younger basaltic lowland. 4. Isidis had collected the subsurface and surface runoff water from a significant area. 5. Depth of the Noachian aged subsurface crust: Argyre's depth is 5200-4000 m below its great circular fault, the same value for Isidis is around 2900-3900 m (measuring the elevation difference between the circular fault and the top of the basalt infill). These are minimal values because Isidis is somewhat greater in size. We can assume max. 1-2 km thick basaltic cover at Isidis Planitia. Another approach is based on the outcrops of the blocks near to the edge of the basin. We had assumed that blocks had formed by similar process like ones at the edge of the southern uplands north of Isidis. The height of these blocks are max. 650-700 m. The distance of the outcrops of blocks at Isidis are max. 100 km from the edge of basalt cover. This suggest min. 1.2° slope angle for the outer part of the basalt cover. The max. vertical elevation of "small" peaks around Isidis are 1500 m above the surrounding, which suggest slope angle of 2.6°. This gives important information on the thickness of basalt cover near to the edge but very uncertain results for the whole basins' depth which could be smaller than 3-4 km. Taken the upper depth values the possible pressure below the lava sheet are in the order of 100 atmosphere which can cause decomposition of ancient sediments below the lava sheet. These sediments could have been shielded by the basaltic cover from the aggressive atmosphere, and pressure driven chemical alterations could have happened. The possible escaping gas could be observable with Beagle-2 lander, and the suspected mud volcanoes could be the result of this

process too [4]. Based on analogy from the Earth the effective porosity on basaltic lava flows are low except between individual flows which cause horizontal porous layers as possible sinks of subsurface volatiles with great permeability [5].

**Theory waiting for test:** Great question is the consequence of the supposed climate changes [6,7,8] on the subsurface temperature and pressure. Theoretically we can divide into two kinds the global warming periods of Mars: the "*internal induced*" warming when subsurface heat source results melting of cryosphere and volatile release. In this case the cryosphere melts from the bottom toward the top at the location of the intrusion. The other one is the "*external induced*" where the atmosphere gets volatiles first from surface sinks (polar cap). In both cases global warming begins with atmosphere thickening and growing of greenhouse effect. Beside the location of any volcanic center, during the global warming the surface gets warmer, and the heat is slowly conducted downward. Because of differences in the thermal conductivity of flood basalt and highland material (which is basaltoid too) and their ice content, the isotherms sink with somewhat different speed at different locations. There is difference in the permeability too: the highland material probably has greater while flood basalt has smaller and good permeability in horizontal oriented layers. Based on the upper mentioned, theoretically we can account on the phenomena visible in Fig. 1. Global warming begins (A), heat gets below the surface by conduction and isotherms sink while isobars rise, if we account on free intergranular gas contact between the subsurface and the atmosphere. Liquid water appears at that locations where the required temperature and pressure frontiers overlap (C). The consequences are: 1. liquid water first appears below the surface, 2. the aquifer is closed from below by the ice filled layer (we suspect non zero value for effective porosity too which make the case somewhat different from simple closed situation). 3. The final shape of the ice surface depends on the draw down of groundwater flow, on the topography and on the effect of the length and temperature of the warm period (E1, E2). In reality the process may be far more complicated and several other parameters have effect on the shape of the final ice surface than mentioned here.

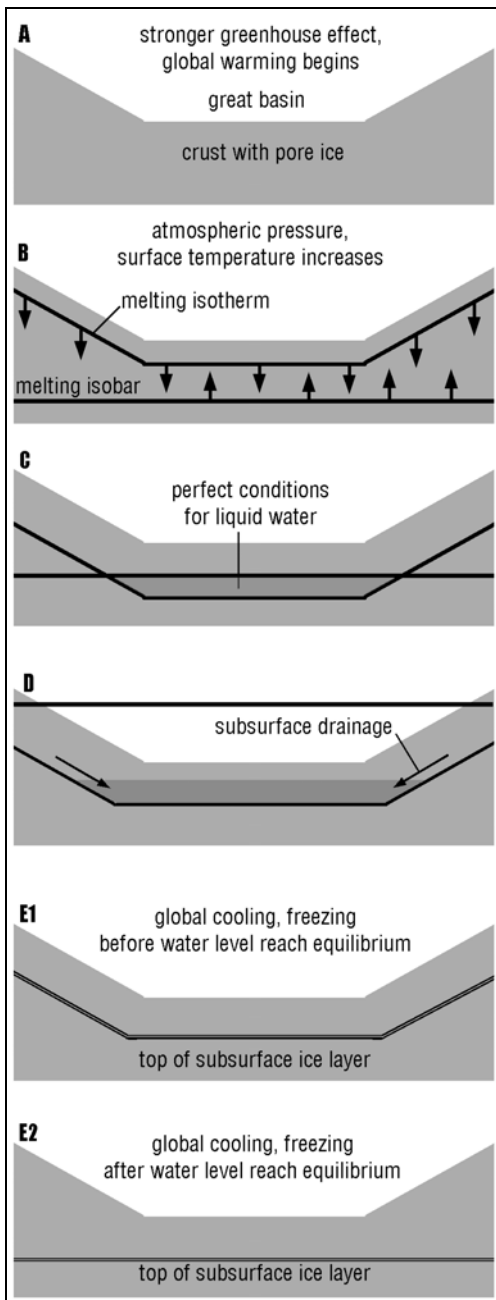


Fig. 1.

**Conclusion:** We suppose that the subsurface ice layers' surface and its relation to the topography hints on the characteristics of the last warm period. The best locations for this analysis are at undulating topography with great height differences, at great basins or at the frontier between lowlands and uplands. In the case of Isidis Planitia we can observe the effect of regional slopes, a transitional case at the contact with the northern uplands, and in-situ surface analysis. The differently elevated basins inside the southern upland (Fig. 2.) can point out differences in the height of subsurface ice layers and help in the reconstruction of the offset of the last great warming. These can help to answer the following questions: Does global climate changes effect the subsurface volatiles first – or the surface signs liquid water is the result of release from surface reservoirs (polar caps, impact location)? Can Mars have two liquid water layers during global warming (one is heated from the surface, the other is the heated by geothermal heat)?

**Observable signs of subsurface structures:** 1. GPR and topography correlation would point to the style of the last great warming on Mars. 2. Beagle-2's Mole gives the possibility to observe subsurface gas environments. Any possible fluvial or limnic sediments below the basaltic lava cover may contain gas/water bearing minerals like clathrates and can steam to the surface. On the Earth the upward migration of the products of hydrate decomposition can take part in the mud-volcanism [9].

**References:** [1] Chicarro A. F. (1999) 5<sup>th</sup> Int. Conf. on Mars #6111. [2] Leuschen C., S. P. Gogineni, Clifford S.M., Raney R.K.; (2001) *Proceedings of the 2001 Int. Geosc. and Remote Sensing Symp.* (IGARSS '01); Sydney, Australia. [3] Paillou P. et al. (1999) 5<sup>th</sup> Int. Conf. on Mars #6061. [4] Head J.W., Bridges J.C. (2001) LPSC XXXII<sup>th</sup> #1236. [5] Wozniak, Karl C., GSA Meeting, 2002, #35095. [6] Nakamura T., Tajuka E. (2003) LPSC XXXIV<sup>th</sup> #1286. [7] Bruce G. Bills (1999) 5<sup>th</sup> Int. Conf. on Mars #6208. [8] Tillman J. E. (1999) 5<sup>th</sup> Int. Conf. on Mars #6156. [9] Robertson A. H. F. et al. (1998) *Proc. Of the Ocean Drilling Program*, Vol. 160, 569-574.

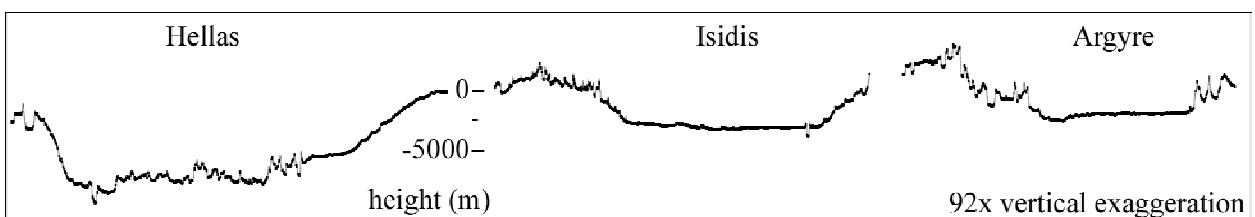


Fig. 2.

### PALEODISCHARGE ESTIMATION FROM MORPHOMETRY FOR ANCIENT CHANNELS.

A. Kereszturi<sup>1</sup> (<sup>1</sup>Department of Physical Geography, Eötvös Lorand University of Sciences, Pázmány sétány 1/C, Budapest, H-1088, Hungary, E-mail: krub@freemail.hu).

**Introduction:** The mass/volume of water was present at or near to the surface of Mars during the planetary evolution is an important question. The runoff valleys are thought to have formed by sapping [1,2,3], the outflow channels by water or cryoclast flows [4,5,6]. The exact style of the flows, the sediment load, the discharge and many other factors are not fully understood [7,8,9]. In this work we outline a possible easy morphology based paleodischarge estimation method for martian channel, which is not able to give exact values, only row estimations, but could be easily used because of its simplicity in many cases as a secondary method together with other ones.

**Bases of the method:** It is known based on examples from the Earth that with the meandering rivers the dimensions of the meanders are determined by the maximal discharge [10]. The method could be used for ancient riverbeds in the paleodischarge estimation. Because on Mars we have only ancient channels (beside the newly discovered small gullies at certain slopes) the method could be useful in the paleodischarge estimation. We had showed in a previous work that there are connections between the dimensions of the meanders (amplitude, radius, wavelength) and the channel width (the later probably proportional to the paleodischarge) (Fig. 1.). We analysed meanders of 120 channels for amplitude, wavelength and radius determination. This suggest that there is similar discharge/morphometric relation on Mars like on Earth. The correlations for all channels are:  $R=0.954$  (amplitude/width),  $T=0.736$  (radius/width),  $R=0.935$  (half wavelength/width); for only runoff channels are 0.875, 0.672, 0.648 respectively. In the following we would like to connect absolute discharge parameters to the morphometric data. We measured the horizontal dimensions based on images of the Viking orbiters [12], channel cross section and slope measurement by MOLA results.

**Uncertainties and errors:** During the process of the measurement the following factors caused uncertainties and errors: 1. The resolution of the MOLA data was high enough but we used only some representative values for certain channels not integration and average from "all values". 2. We modelled the shape of the channels' cross sections with triangles or trapezoids instead of the real cross section. 3. The hydraulic behaviour of the water flows under the surface gravity of

Mars differs from that we know on the Earth where the Manning equation is used for discharge estimation. 4. The solid matter content is unknown too which can cause differences in the viscosity and flow velocity. 5. The greatest errors could arise from the unknown water depth and later sedimentary infill. This could be greatest at the case of the oldest runoff channels because their channel width are probably equal to the width of the valley.

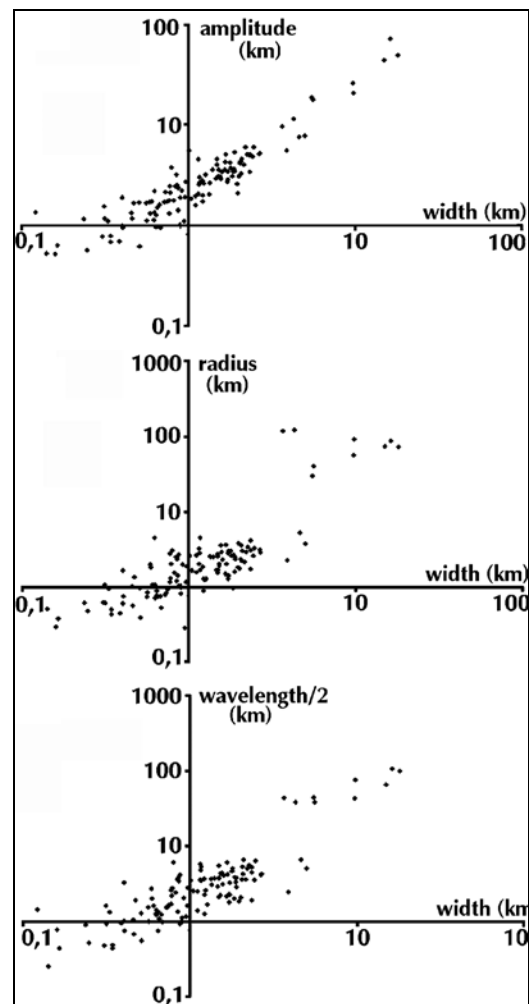


Fig. 1.  
Meander/channel width correlations

**Meandering and the origin of channels:** Several styles of formation was supposed for the runoff and outflow channels. No matter what was the original

solid matter content of the flows (“clean” water, high mud concentration, submarine turbidity flows, CO<sub>2</sub> driven cryosclastic flows etc. the hydraulic behaviour can result such morphology which is in connection with the discharge of the fluid (or fluid like matter). It is known from the Earth that meandering can be observed at not only rivers but turbidity flows or atmospheric currents.

**Results:** We have estimated the paleodischarge values based on the Manning equation modified to account Mars lower gravity [13] with  $n=0.075$  for runoff and outflow channels. Fretted channels were excluded except that cases where originally the channel was formed by meandering fluvial erosion obviously based on the sinuous appearance. Some outflow channels was excluded too because their unusual slope direction does not coincide with the supposed flow direction based on morphology [14]. The correlation between the discharge values and the meanders’ parameters is lower than that ones between the channel width and the meanders’ parameters. The discharge values computed from Manning equation versus the meanders’ radius are visible in Fig. 2. (*A*: for all analysed channels, *B*: only runoff channels, *C*: circum-Chryse and circum-Hellas are emphasized, *D*: correlation for runoff and outflow channels without circum-Hellas ones) The weaker correlation can be caused by the uncertainties of the depth of water had flowed in the channel. There are special cases for the channels around Hellas. Their discharge values are too large comparing to the sizes of meanders which could be the result of differences in the sedimentation on the bottoms’ of the channels and/or in the hydraulic behaviour of the fluid.

**Conclusions:** 1. The strong correlation between the width and meandering parameters suggest correlation between the paleodischarge and morphometry. 2. The correlation between the estimated paleodischarge (based on Manning equation) and meandering parameters is weaker possibly because of the uncertainty in the estimation of the original water depth. The correlation excluding the circum Hellas channels is  $R=0.933$  and including circum Hellas channels is  $R=0.487$ . This suggest great differences between the circum Hellas and circum Chryse channels in the hydraulics and/or in the sedimentation. For the runoff channels the estimated discharges are highly variable at the same meandering parameters. The meandering method can be useful in the cases when no topographic data is available. In the case of buried outflow channels was discovered around Chryse Planitia based on their

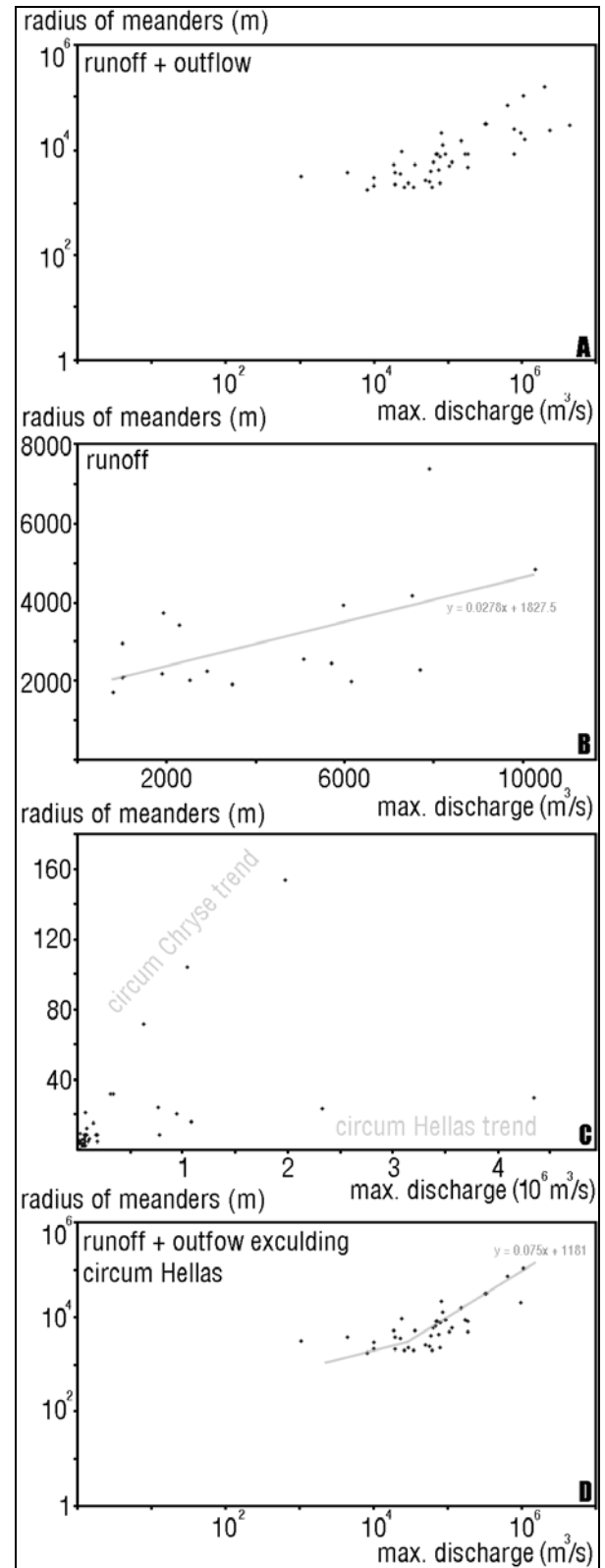


Fig. 2. Meander/paleodischarge correlation

gravity anomaly. No obvious meanders are visible but done detailed future data may reveal meander like phenomena and would be able to estimate paleodischarge for buried channels too. The method can be used for the discharge changes at the same channel, see Fig. 3. for an example (top: morphology, different meander generations marked with numbers, bottom: morphometric connection).

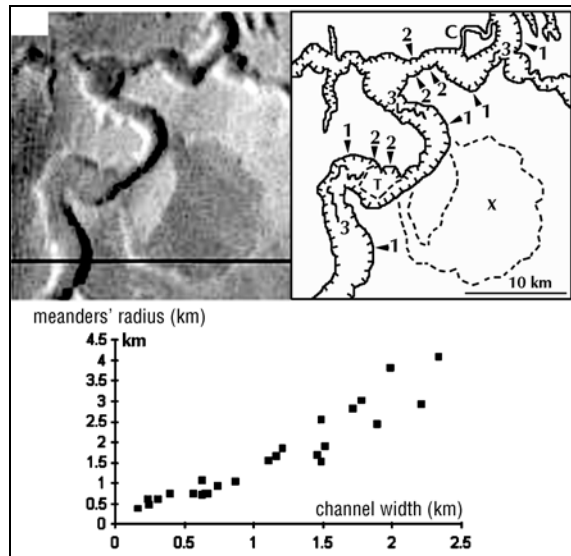


Fig. 3. Meander generations

**References:** [1] Carr M. H. 1981. The surface of Mars, Yale University Press, [2] Carr M. H. (1986) *Icarus* 65/187-202, [3] Carr M. H. (1999) *5<sup>th</sup> International Conference on Mars #6030*. [4] Skinner J. A., Tanaka K. L. (2000) *LPSC XXX. #2076*, [5] Baker V. R. et. al. (1987) *Geol. Soc. Of Am. Vol. 2. 403-467*, [6] Komar P. D. (1983) *Geology Vol. 11. 651-654*, [7] Lee P., Rice J. W. (1999) *5<sup>th</sup> International Conference on Mars #6237*. [8] Chapman M. G., Tanaka K. L. (2000) *LPSC XXX. #1256*, [9] Cabrol N. A. (1999) *LPSC XXIX #1022*, [10] Gábris Gy. (1995) *Földrajzi Értesítő, XLIV. 1-2, 101-109*. [12] Planetary Data System [13] Carr M. H. (1979) *JGR 84. 2995-3007*. [14] Williams E. M., Phillips R. J. *5<sup>th</sup> International Conference on Mars #6035*.

**Acknowledgment:** This work was supported by the Hungarian Astronomical Association and the Pólaris Observatory.

**GRAVITY EVIDENCE FOR EXTINCT MAGMA CHAMBER SYSTEMS ON MARS.** Walter S. Kiefer, *Lunar and Planetary Institute, Houston TX 77058-1113, USA (kief@lpi.usra.edu, http://www.lpi.usra.edu/science/kiefer/, (281) 486-2110).*

The *Mars Global Surveyor* mission has vastly improved our knowledge of the topography and gravity of Mars [1,2,3], permitting detailed geophysical modeling of subsurface structures such as magma chamber systems for the first time. In this work, I describe gravity models for Syrtis Major [4], Tyrrhena Patera, and Hadriaca Patera as well as preliminary results for Amphitrites Patera. In each case, flexurally supported surface topography can not explain the observed gravity anomaly. High density, buried material is required at each volcano, most likely as dense cumulate minerals in extinct magma chamber systems. These results provide our first look at the magmatic plumbing of Mars.

#### Model

The gravity models are calculated for spherical harmonic degrees 2 through 50, corresponding to a half-wavelength spectral resolution of 213 km. This ensures that the signal-to-noise ratio remains high and thus that the observed gravity anomalies are robustly determined. The RMS uncertainty in the gravity models is 10-13 mGal [2], which is a small fraction of the observed peak amplitudes for the study regions. Flexural support of the surface topography is calculated using a spherical thin-elastic shell model [5] with elastic constants and a load density appropriate for basalt.

I model the subsurface structures as buried vertical cylinders. Bounds on the cylinder radius,  $R$ , are determined from the width of the gravity anomaly. The depth of the cylinder,  $D$ , and the density contrast between the cylinder and the surrounding crust,  $\delta\rho$ , are adjusted to fit the anomaly amplitude. Models with multiple cylinders sometimes improve the fit to the observations. The cylinders are assumed to be uncompensated to set a lower bound on the required density contrast between the cylinder and the surrounding crust. The density contrast inside the cylinder is tapered smoothly to zero at its outer edge to avoid problems with Gibbs phenomenon in the spherical harmonic expansion. The vertical integration over the cylinder's depth is performed numerically using a 1 km step size. The total model gravity anomaly is the sum of the contributions from the topographic and buried loads.

Some of the martian meteorites, such as Nakhla and Chassigny, are pyroxene or olivine cumulates and provide analogs for the material that may be present in the magma chambers. Densities of up to  $3300 \text{ kg m}^{-3}$  (pyroxene dominated) or  $3600 \text{ kg m}^{-3}$  (olivine dominated) are petrologically reasonable [6,7]. If the magma chamber is a network of intrusive material within a matrix of pre-existing crust, the net magma chamber density would be smaller than these values. Because  $D$  and  $\delta\rho$  can not be separately determined, in this work I report minimum values of  $D$  based on the petrologically likely maximum values of  $\delta\rho$ .

#### Results

*Syrtis Major:* Syrtis Major has basaltic flow morphologies, a basal diameter of 1100 km, and is about 1 km high [8]. The topographic caldera is 150x250 km, elongated north-

south, and is up to 2 km deeper than the rim. The gravity anomaly is 100 mGal at spherical harmonic degree 40 and 126 mGal at degree 50.

I have recently presented a gravity model for Syrtis Major [4] and showed that the gravity data requires the presence of a buried, high-density body. The spatial association between the caldera and the buried structure indicates that the subsurface structure is most likely due to dense cumulate minerals in an extinct magma chamber system. The Syrtis Major magma chamber is approximately 300 by 600 km across, broader than the topographic caldera but narrower than the overall volcanic edifice. Like the caldera, the magma chamber is elongated in the north-south direction. The minimum magma chamber thickness is 3.6 km (olivine dominated) to 5.8 km (pyroxene dominated). Assuming a 10% density change from melt to solid, solidification of the magma chamber can account for only a few hundred meters of caldera relief. Thus, most of the caldera's depth must be accounted for by removal of magma from the magma chamber and subsequent caldera collapse. The best fitting elastic lithosphere thickness is 10-15 km for a crust density of  $\rho = 2800 \text{ kg m}^{-3}$ .

*Tyrrhena Patera:* Tyrrhena Patera is 215 by 350 km across with a maximum relief of 1.3 km. The summit caldera complex is 41 by 55 km across [9]. Tyrrhena is primarily Hesperian in age, and based on its morphology is interpreted as forming primarily by pyroclastic flows [10].

Figure 1a shows the gravity anomaly across Tyrrhena. There is excellent agreement in shape and amplitude between models MGM1025 and MGS85F, which are based on the same Doppler tracking data but independent data processing and inversion. The anomaly is robustly determined, with a peak amplitude of 145 mGal at spherical harmonic degree 40 and 165 mGal at degree 50. Figure 2 shows an east-west profile through the Tyrrhena gravity anomaly. A model based on flexurally supported surface topography (lithosphere thickness 15 km, short dashed line) is a poor fit to the observations, so buried high density material is required in this region.

The long-dashed line is a model with both flexurally supported surface topography and a buried cylinder (108 East, 22.5 South,  $R=300$  km). The cylinder radius is constrained to a value between 275 and 300 km by the width of the observed gravity anomaly. Assuming a maximum density contrast of  $\delta\rho = 800 \text{ kg m}^{-3}$  (for an olivine-dominated magma chamber), the minimum thickness of the cylinder is 2.9 km. For a pyroxene-dominated magma chamber of  $\delta\rho = 500 \text{ kg m}^{-3}$ , the minimum cylinder thickness is 4.7 km. The buried structure is roughly twice the diameter of the surface volcanic edifice, and the total buried mass is roughly an order of magnitude larger than the mass of the volcanic edifice and its subsurface root. Tyrrhena is surrounded by more than 1 million square kilometers of Hesperian age lava plains [11]. Some of these plains are explicitly identified as flows associated with Tyrrhena (units Htf and AHtp of [12], unit HNre of [13]).

## EXTINCT MAGMA CHAMBER SYSTEMS ON MARS: W. S. Kiefer

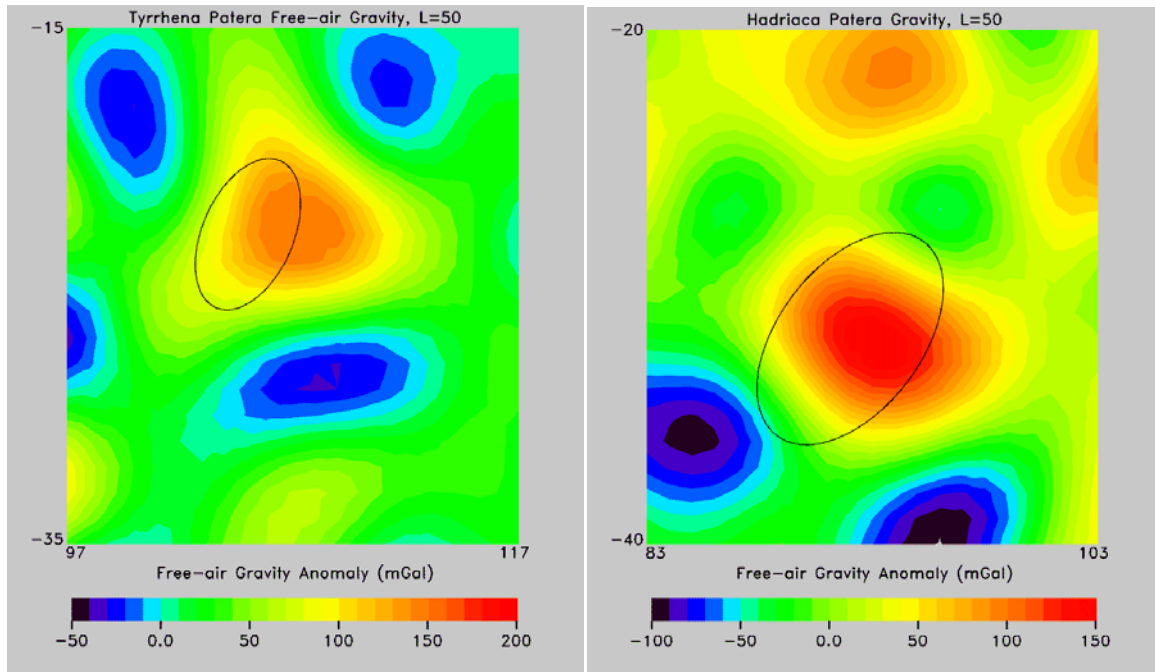


Figure 1: The spherical harmonic degree 50 free-air gravity anomaly at Tyrrhena Patera (left) and Hadriaca Patera (right). The ellipses shows the location of the volcanic edifices.

Much of the lava in these plains must have been processed through the magma chamber system imaged by the gravity anomaly.

**Hadriaca Patera:** Hadriaca Patera is 330 by 550 km across with a maximum relief of 1.1 km [9]. The summit caldera is nearly circular, with a diameter of 77 km. Hadriaca is primarily Hesperian in age, and based on its morphology is interpreted as forming primarily by pyroclastic flows [14].

Figure 1b shows the gravity anomaly across Hadriaca. The peak gravity anomaly at Hadriaca is 141 mGal at spherical harmonic degree 40 and 154 mGal at degree 50. A model using just flexurally supported surface topography is a poor fit to the observations over the volcano (Figure 3, 93 East, 33 South), so a buried high density load is required. The topographic high north of Hadriaca (Figure 3b, 20-25 South) is well fit by flexurally supported topography alone with an elastic lithosphere of 15 km.

An excellent fit to the data can be achieved using two buried cylinders in addition to the flexurally supported topography. Cylinder 1 (93.5 East, 32.5 South,  $R=250$  km) has a minimum thickness of 4.7 km (olivine dominated) to 7.8 km (pyroxene dominated). Cylinder 2 (98.5 East, 32.5 South,  $R=150$  km) is about 80% as thick as cylinder 1, assuming that the two cylinders have the same  $\delta\rho$ . As at Tyrrhena Patera, much of the lava plains surrounding Hadriaca Patera probably passed through the magma chamber system revealed by the gravity data. Assessing the volume and hence mass of these plains is difficult because Hadriaca is located on the

topographic slope into the Hellas impact basin.

**Amphitrites Patera:** Amphitrites Patera and Peneus Patera are calderas that form a single volcanic complex on the southwest rim of the Hellas basin. Lava flow morphologies are obscured by aeolian mantling, but the caldera morphology resembles Syrtis Major [15]. Each caldera is 120-135 km across. The overall edifice is 600-700 km across, with a topographic relief of 0.5-1.5 km [9,15].

The gravity anomaly is 133 mGal at spherical harmonic degree 40 and 185 mGal at spherical harmonic degree 50, centered on the Amphitrite caldera at 61 East, 59 South. This anomaly is one of the largest known in the southern hemisphere of Mars [2]. Based on its large amplitude and the volcanic morphology, it seems likely that Amphitrites and Peneus are another example of a large, buried magma chamber. Detailed models of this anomaly are presently in development.

#### Implications

Magma chamber systems have now been observed at three volcanos on Mars, Syrtis Major, Tyrrhena Patera, and Hadriaca Patera. Amphitrites Patera is probably a fourth example. It is highly unlikely that errors in the gravity field determination would produce large gravity anomalies over each volcano. Similarly, it is also unlikely that high density material unrelated to the volcanos would occur beneath the each volcano by chance. Thus, the overall suite of results reported here greatly strengthens the case for buried magma chamber systems at each location.

The minimum magma chamber thicknesses inferred in

EXTINCT MAGMA CHAMBER SYSTEMS ON MARS: W. S. Kiefer

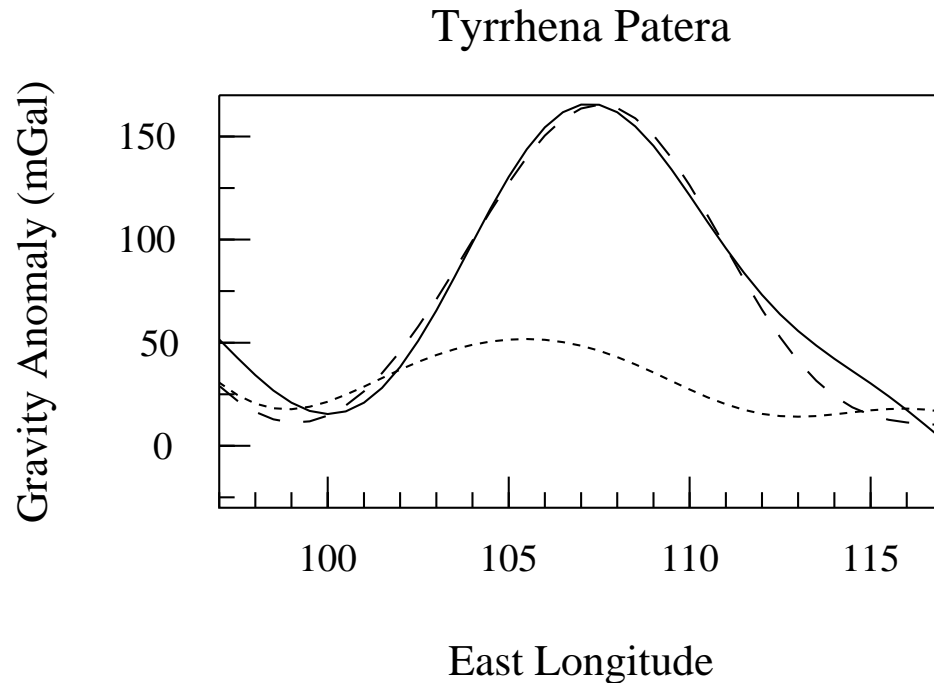


Figure 2: Gravity profiles across Tyrrhena Patera at 22.5 South Latitude. The solid line is the observed gravity anomaly (model MGM1025, spherical harmonic degrees 2-50), the short dashed line is a model based on flexurally supported topography, and the long dashed line is a model that includes both flexurally supported topography as well as the buried, high-density load.

this study range from 2.9 to 4.7 km for olivine-dominated systems and 4.7 to 7.8 km for pyroxene-dominated systems. Although olivine may contribute to these cumulate systems, it is unlikely that the required cumulate mass could be explained by olivine alone. Thus, the minimum chamber thicknesses are probably closer to the pyroxene-dominated thicknesses. However, considerably thicker chambers are permitted by the gravity data. Because of the large horizontal extent of the magma chambers and the likelihood that much of the lava in the surrounding plains flowed through these chambers, thicker chambers with correspondingly smaller values of  $\delta\rho$  are likely. Because these structures formed as cumulates, probably over long periods of time, the entire thickness of the system did not need to be molten at any given time.

#### Terrestrial Analogs

A number of possible terrestrial analogs exist for these large-scale magmatic structures on Mars. Several large igneous provinces (the Deccan Traps, Kerguelen, the North Atlantic Volcanic Province, and Ontong Java) exceed  $10^6 km^2$  in area and range from  $6 \cdot 10^6$  to  $7 \cdot 10^7 km^3$  in volume [16]. These are not primarily cumulate structures, although the small volume Skaergaard layered intrusive complex is a part of the North Atlantic Volcanic Province [17]. Seismic reflection and gravity data define a dense, subcrustal intrusive complex beneath Hawaii that is 200 km across and up to 6 km thick [18]. Gravity modeling of Iceland has recently been used to infer abnormally dense lower crust that is several hundred kilometers across [19].

#### Future Observations: Mars Reconnaissance Orbiter

The limiting factor in the spatial resolution of the martian gravity field is the spacecraft altitude. *Mars Global Surveyor* operated at a periapsis altitude of 370 km [2], whereas the *Mars Reconnaissance Orbiter* is currently planned to have a periapsis altitude of 250 km. This should permit roughly a 50% increase the gravity field resolution, with a geophysically interpretable resolution of about harmonic degree 80. This will permit tighter limits on the allowed cylinder radii in these models. In turn, this will also place tighter bounds on the required magma chamber thickness and density contrast, improving our overall knowledge of the magmatic plumbing system of Mars.

[1] Smith et al., JGR 106, 23,689-23,722, 2001. [2] Lemoine et al., JGR 106, 23,359-23,376, 2001. [3] Yuan et al., JGR 106, 23,377-23,401, 2001. [4] Kiefer, EPSL, submitted, 2003. [5] Turcotte et al., JGR 86, 3951-3959, 1981. [6] Consolmagno and Britt, MAPS 33, 1231-1241, 1998. [7] Britt and Consolmagno, MAPS, in press, 2003. [8] Schaber, JGR 87, 9852-9866, 1982. [9] Plescia, LPSC 33, abstract 1854, 2002. [10] Greeley and Crown, JGR 95, 7133-7149, 1990. [11] Greeley and Guest, USGS Map I-1802B, 1987. [12] Leonard and Tanaka, USGS Map I-2694, 2001. [13] Gregg et al., USGS Map I-2556, 1998. [14] Crown and Greeley, JGR 98, 3431-3451, 1993. [15] Plescia, LPSC 34, abstract 1478, 2003. [16] Coffin and Eldholm, Rev. Geophys. 32, 1-36, 1994. [17] Ernst and Buchanan, pp. 483-575 in *Mantle Plumes: Their Identification Through Time*, GSA Special Paper 352, 2001. [18] ten Brink and Brocher, JGR 92, 13,687-13,707, 1987. [19] Gudmundsson, EPSL 206, 427-440, 2003.

## EXTINCT MAGMA CHAMBER SYSTEMS ON MARS: W. S. Kiefer

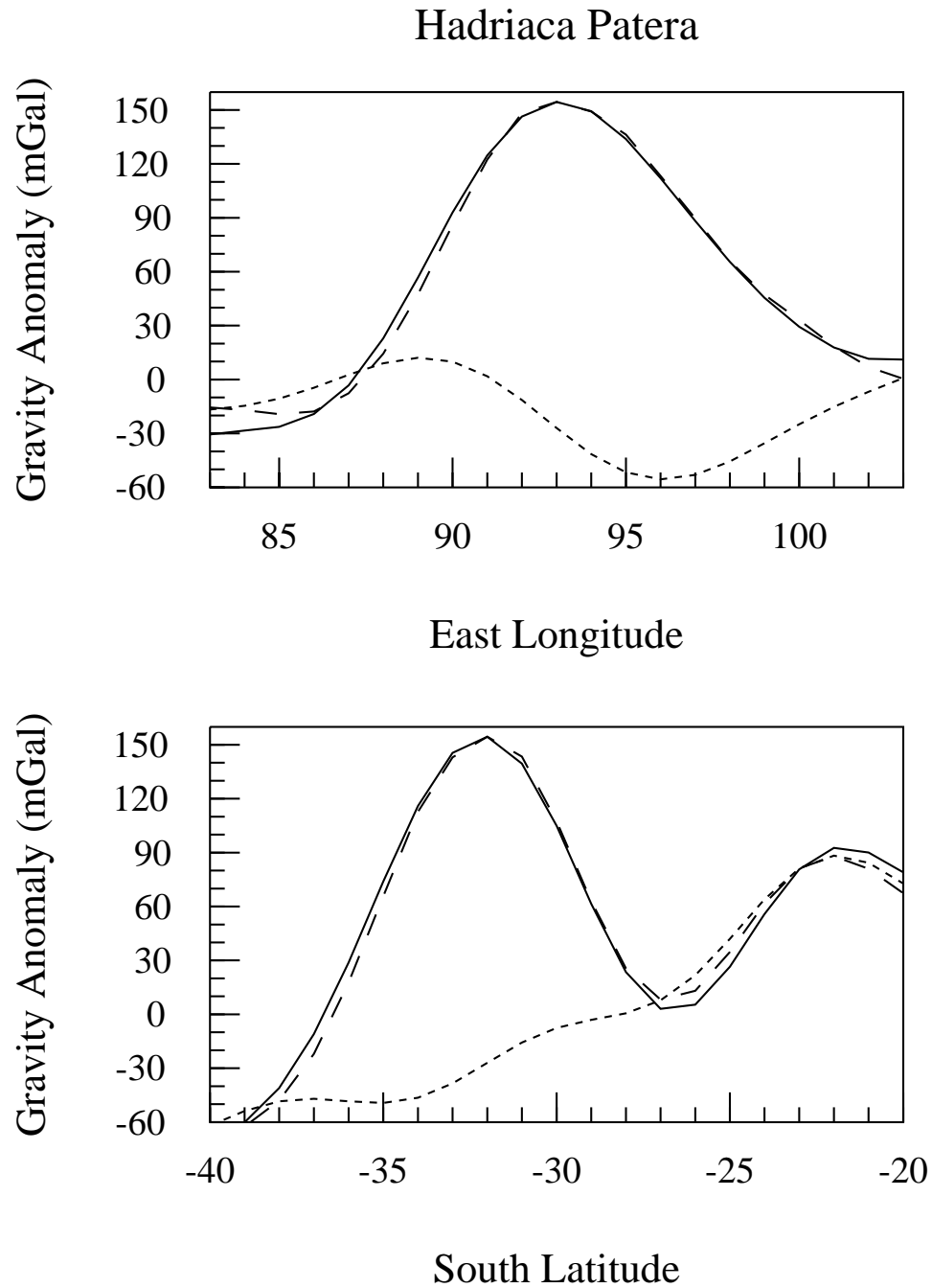


Figure 3: Gravity profiles across Hadriaca Patera. Top: East-West across 32 South latitude. Bottom: North-South across 93 East longitude. The solid lines are the observed gravity anomalies (model MGM1025, spherical harmonic degrees 2-50), the short dashed lines are models based on flexurally supported topography, and the long dashed lines are models that includes both flexurally supported topography as well as buried, high-density loads.

**BEHAVIOR OF SOLID CO<sub>2</sub> ON MARS: A REAL ZOO.** Hugh H. Kieffer, *U. S. Geological Survey [Emeritus], Flagstaff, AZ 86001, USA, (hkieffer@uneeedspeed.net).*

Observations of the martian polar caps by TES, THEMIS and MOC have revealed several unexpected things: now informally known as cryptic material, Dalmatian spots, black spiders, oriented fans and fried eggs. These result from the characteristics and behavior of solid CO<sub>2</sub> on Mars, which is unlike anything on Earth. I will attempt to explain this zoo qualitatively in terms of the interaction of CO<sub>2</sub> and dust with the solar and thermal radiation fields on Mars. Some of these concepts have been published [11, 10, 14].

## 1 CO<sub>2</sub> Surface Condensation Modes

The condensation of the predominant gas in an atmosphere by radiative cooling yields the prominent seasonal polar caps on Mars. This process has no terrestrial analogy, which limits our intuition. This process is difficult to impossible to simulate in the laboratory because the natural force that allows condensation at a location other than at the coldest boundary (which sets the radiation balance) is gravitation, yielding a characteristic scale-height on Mars of 7 km. A practical laboratory scale would require a physical barrier that is completely transparent to thermal radiation,

The altitude at which CO<sub>2</sub> condenses in the martian winter has been largely clarified by TES observations. This problem was studied by Forget et al.[2]. They found that significant condensation occurs in the atmosphere initially with small grain sizes, which then rapidly grow to the order of 100 μm. However, the large grain sizes implied by the TES observations in many areas in the polar night indicate that most of the condensation occurs at the Martian surface. TES spectra in the 25 μm region indicate that the “**cryptic**” regions of cold-dark polar material consist of a CO<sub>2</sub> non-scattering slab composed of indeterminately large grains.

For condensation of a nearly pure gas by radiative loss there can be two end-member solutions for the form of the solid. If the abundance of non-condensing gases is negligible, so that a diffusion gradient of the condensing material is not involved, then a thick slab can form. This is particularly true when the amount of gas between the condensation site and the low-radiation background (space) is large enough that significant path lengths in the solid are needed to generate appreciable emissivities outside the bands in which the gas absorbs. In this case, which holds for Mars, the dominant radiative loss of the condensate is from inside the bulk material. Growth perturbations outward from a planar solid interface, such as a crystal spike growing upward, have a poor conductive path to the bulk solid which, in turn, can radiate away the latent heat of condensation. Lacking a diffusion gradient at the tip of such a spike, the condensation rate is limited by conductive heat loss, not by abundance of molecules in the gas phase, and this tip is at a disadvantage for condensation relative to the bulk solid. Thus these perturbations do not grow, and the expected steady state form is a thick slab with a smooth surface. Such slabs are observed to grow in laboratory conditions of

pure condensing gases [8], although in those cases the thermal gradient internal to the slab results from conduction to a cold substrate rather than by radiative cooling.

In the presence of some amount of non-condensing gas, e.g., the 5% of N<sub>2</sub> plus Ar on Mars, at the micro-physical level there will be some diffusion gradient of the condensing gas toward the condensation sites. If one assumes that both the temperature gradient and the concentration gradient of the condensate are linear across this layer, as would be expected for steady state conditions, then, because of the nonlinear dependence of saturation pressure upon temperature, the partial pressure will be above the saturation pressure throughout this layer. Under this condition, if there is adequate heat conduction down the spike into the substrate (from which radiation is efficient), then spikes sticking up into this diffusion gradient become the favored site of condensation and they will grow more rapidly than locations deeper into the diffusion gradient. The steady state solution for the form of such a growing deposit is long columnar crystals oriented along the diffusion gradient. Such deposits also are observed to form in laboratory conditions of substrate cooling when small amounts of non-condensing gas are introduced into the chamber [8, 9]. This process of growth in a diffusion gradient gives rise to the beautiful H<sub>2</sub>O hoar frost crystals which can be seen on calm terrestrial winter mornings.

Although it has been shown that enriched layers of the non-condensing Martian gases (nitrogen and argon) would be dynamically unstable [5], this process likely occurs at the micro-physical level, e.g., at the scale of frost grains. The requirement to address this process is a model of the stability of a gravitationally unstable diffusion gradient at the scale of millimeters or less when the primary gas is condensing with net flow downward toward the surface.

TES observations indicate that both the slab growth and deposition of fine-grain CO<sub>2</sub> condensates occur in the polar night and that different condensation processes are dominant in different locations. Also, fine-grained CO<sub>2</sub> condensates (frost) can undergo rapid metamorphism into a nonporous (and hence non-scattering for a non-birefringent material such as solid CO<sub>2</sub>) polycrystalline layer[1]. The reason for the geographic distribution of the cryptic material is unknown.

## 2 Radiation Balance in a Pure Solid CO<sub>2</sub> Slab

During the polar night, the radiative balance of surface CO<sub>2</sub> will be negative (barring an extraordinarily warm atmosphere). With the Sun above the horizon, solar radiation penetrates deeply into pure CO<sub>2</sub>. The relative absorption lengths for solar and thermal energy become important.

Using the optical properties of solid carbon dioxide [4], the penetration of solar energy into a slab of CO<sub>2</sub> can be calculated as

$$\int_0^{\infty} S_{\lambda} e^{-p/l_{\lambda}} d\lambda \quad (1)$$

where  $S_{\lambda} = S_{\odot}(1 - R_{\lambda}) \cos i/U^2$  is the sunlight that is refracted into the slab surface,  $R_{\lambda}$  is the Fresnel reflection coefficient,  $i$  is the incidence angle (measured from zenith),  $U$  the heliocentric distance in Astronomical Units,  $p$  is the path length from the surface along the refracted path and  $l_{\lambda} = \lambda/(4\pi n_i/n_r)$  is the absorption length;  $n_r$  and  $n_i$  are the real and imaginary parts of the complex index of refraction.

A similar calculation at thermal wavelengths replacing  $S_{\odot}/U^2$  with the Planck function (with  $i = 60^{\circ}$  to represent the upper hemisphere) yields the effective visibility of space to thermal energy within the slab.

For typical polar summer conditions (incidence angle of  $65^{\circ}$ ,  $U = 1.5$ ), 2/3 of the solar energy penetrates 1m into pure solid  $\text{CO}_2$ , whereas thermal flux is reduced to 50% in 3.7 mm. The top 2 mm of the slab are in net radiative loss; below that absorption of insolation results in net heating.

### 3 Dirty $\text{CO}_2$ Ice

Mars atmosphere is generally dusty with particles of radius on the order of  $2 \mu\text{m}$  [7, 15]. During the  $\text{CO}_2$  condensation season, atmospheric dust grains probably act as condensation nuclei; perhaps first for  $\text{H}_2\text{O}$  and then for  $\text{CO}_2$ . The proportion of dust in the  $\text{CO}_2$  cap has not been measured, but is reasonably assumed to be near the average abundance of dust in the atmosphere. Using an average visual opacity of the atmosphere of 0.5 yields a dust abundance of about  $1.5 \times 10^{-3} \text{ kg m}^{-3}$  or roughly  $2 \times 10^{-5}$  by mass. Because the particle size is smaller than thermal wavelengths, the presence of embedded dust will make little change to the thermal radiation environment, but will shorten substantially the solar absorption lengths, narrowing or removing entirely the surficial layer with net radiation loss.

Using the above values, and densities of dust grains and solid  $\text{CO}_2$  of  $2300$  and  $1600 \text{ kg m}^{-3}$ , respectively, corresponds to a mean dust grain separation of  $\sim 130 \mu\text{m}$ . If a seasonal cap budget of  $1000 \text{ kg m}^{-2}$  is adopted [11], the mass of dust in the cap is  $0.02 \text{ kg m}^{-2}$  and the geometric opacity of the dust in the cap is  $\sim 1.6$ . The visual opacity of dust in the slab at sunrise will be roughly the average opacity of the southern atmosphere during the condensation season times the ratio of slab to atmospheric mass, or  $\sim 3.3$ , in agreement with the geometric opacity if the scattering efficiency is taken as 2.0, as expected from Mie theory.

### 4 $\text{CO}_2$ Self Cleaning by Entrained Dust Movement

A first approximation is that for a dirty  $\text{CO}_2$  slab, all of the solar energy is absorbed by the dust grains. However, because the surrounding  $\text{CO}_2$  is isothermal, this radiation absorbed by the grains must go into sublimation of solid  $\text{CO}_2$ . If the local material is impermeable, a high-pressure pocket of gas will form around the grain and local elastic deformation will increase the pressure in the solid  $\text{CO}_2$ , allowing some heat to

be absorbed without sublimation; no quantitative calculations of this process have been done. The warmer grain cannot be in direct contact with the  $\text{CO}_2$ , but must rest on a microscopic layer of gas at the bottom of its vapor prison. If the local gas bubble does not rupture, there will be a downward migration of the bubble through the solid as vapor re-condenses on the roof of the bubble, the location most distant from the grain and hence coolest, and the grain will "burrow" downward as sublimation continues under the grain. Thus, a sealed finite vertical columnar hole will travel downward with the grain. When the grain reaches the bottom of the impermeable layer, it will be ejected downward. This self-cleaning, self-annealing process will tend to reduce the amount of dust in the ice through the spring. Because the net solar flux is greater toward the top of the slab, the uppermost particles will move most rapidly, resulting in concentration of dust as a descending "curtain" in the slab, leaving clean ice above.

A quantitative model of the vertical migration velocity of a grain and its sealed gas envelope is wanting.

If the environment is permeable, or if the bubble fractures, the grain may be carried along in the streaming gas. The gas velocity in a tube must be higher than the regional sublimation wind; that net vertical gas velocity is related directly to the regional albedo and is easily computed ([11] section 12.2). Bright ( $A = 0.8$ ) and dark ( $A = 0.25$ ) regions can loft grains smaller than  $\sim 2$  and  $\sim 7 \mu\text{m}$  radius, respectively. Thus, dust grains which entered the seasonal cap from the atmosphere can be carried out of a  $\text{CO}_2$  slab.

### 5 Development of Pathways and Vents

The net positive radiation divergence near the surface of pure  $\text{CO}_2$ , as described above, will tend to seal small holes in the surface layer. Porosity will generally be sealed in a region that grows downward from the surface. Thus, the gas formed by springtime sublimation generally cannot diffuse upward through the  $\text{CO}_2$  deposit. The gas resulting from net sublimation below the surface must escape somewhere and will hold open some set of larger holes. Because the gases in these vents will have some entrained dust, they can continue to absorb solar radiation, transfer energy to the vent walls, and remain open and grow. Also, gas under an impermeable  $\text{CO}_2$  slab could reach pressures several times the atmospheric surface pressure. The saturation temperature under a  $1000 \text{ kg m}^{-2}$  slab would be 162K, enhancing the ability of venting gas to enlarge the pathways. Because higher velocities are possible and because of the  $r^2$  heat flow versus the  $r^1$  circumference, larger holes/paths will grow at the expense of smaller ones.

To the extent that solar energy penetrates to the bottom of the seasonal  $\text{CO}_2$  slab, gas will be released beneath the slab and must find some path to the open atmosphere. It may travel laterally underneath the slab to vents, cracks, or even to the edge of the seasonal deposit. It is difficult to predict the spacing of such vents, but they collectively must carry the total sublimation gas flux of about  $10 \text{ kg m}^{-2}$  /day. It seems likely that the spacing between major pathways would be no more than a couple orders of magnitude greater than the thickness of the slab, or a few hundred meters. This is what is actually

observed.

As the effective vents are separated by substantially more than the slab thickness, gas velocities will become far greater than required to suspend dust particles, and any sub-slab lateral transport may begin erosion of underlying loose material. Once the velocity exceeds the fluid threshold [3], erosion will begin, although the details of saltation versus suspension may be quite different in a thin layer confined both below and above than for the normal condition of a free upper boundary.

The sub-slab lateral gas velocity will depend upon the geometry of the flow; the average velocity must initially decrease away from the vent. It seems likely that the circularly symmetric case of gas radially converging to a vent is not stable and that channels will develop. Because the soil thermal inertia of the Cryptic region is low, it is likely that the surface material is incohesive and that channelized flow will develop by scouring, beginning near the vents and radiating outward. Although velocities on the order of 10 m/s are required to initiate transport of fine material by saltation [16, 3], injection of dust released from the CO<sub>2</sub> into the lateral flow may initiate motion and scouring at lower velocities; 2 mm/s vertical velocity is adequate to maintain atmospheric dust in suspension. Also, the initial gas flow is likely to be diffuse flow through the soil (versus stream flow above the soil in classic saltation), and small soil grains may begin to move well before saltation threshold velocities.

Dark radially converging dendritic patterns are visible in MOC images of some portions of the spring polar cap, these have been termed "**black spiders**" by the MOC team [6]. In this model, these patterns represent channels formed by sub-slab channelized flow of the sublimation gas toward the vents. Increasingly large particles could become entrained closer to the vent.

The velocity in the vents will be approximately  $.005X^2$  m/s, where  $X$  is the ratio of vent separation to vent diameter. For example, for vents 1 m in diameter spaced by 100 m, the gas velocity would be 50 m/s. When the jets exhaust into the atmosphere and velocities decrease, the coarser entrained material will fall out in the prevailing downwind direction. In this model, the oriented dark **fans** seen in the MOC images are caused by this process. This is an exotic model that agrees with observations thus far. It predicts that the dark fans will be oriented into the prevailing wind, that they are seasonal and will disappear with, or shortly after, the CO<sub>2</sub> is gone, and that the "black spiders" will be found only in the Cryptic region.

Once a vent has grown to a radius larger than the slab thickness, wall erosion by warm venting gases becomes relatively less important, and the growth of the dark (hence warmer) spot by local re-radiation and by warming of the atmosphere immediately over the bare ground, which can waft over the neighboring frosts, will cause the defrosted areas to grow, much as terrestrial spring snow cover recedes by the growth and combination of many small defrosted spots.

Darks vents are generally, but not exclusively, associated with dunes. Vents can progress into dark spots (**Dalmatian spots**) which grow monotonically until they coalesce. Dark halos commonly develop around the Dalmatian spots; these have been termed ("**fried-eggs**" based on their symmetry and proportions. Many MOC images of the seasonal cap in summer-

time show great variegation of reflectance, interpreted to be incomplete solid CO<sub>2</sub> cover [13]. Sequences of images show the development of evenly-distributed circular dark spots, which may represent the evolution of vents, commonly spaced by order 100 m, that gradually expand to consume the seasonal cap.

This model has been supported by a survey of the location of "spiders" in MOC imaging which shows that they are largely confined to the Cryptic region and their centers generally correlate with the location of fans[12]. Spiders commonly persist as low relief features through the summer[12].

Most of this story has been developed from observations of the south polar cap. The north and south caps seem to be somewhat different in terms of the abundance of these features; e.g., spiders have not yet been identified in the north.

## 6 Summary

Deep in the martian polar night, there is some CO<sub>2</sub> snowfall, but most of the solid CO<sub>2</sub> takes the form of a uniform, continuous, non-scattering slab with embedded dust (and H<sub>2</sub>O ice) grains. Following seasonal sunrise, in some areas the ice brightens due to fracture or surficial frosting, but in other areas the slab persists to form the **cryptic** regions. The solar energy is largely absorbed by the dust grains, which either burrow downward or escape upward, cleaning the CO<sub>2</sub> slab which anneals small holes near its surface. Sunlight then penetrates to the bottom of the slab, warming the soil and subliming ice from the bottom. Widely spaced vents develop that allow the gas to escape. As the sub-slab gas converges toward the vents, it scours the soil surface along ragged channels (**spiders**). Dust entrained in the jetting gas falls out downwind to form **fans**. The vents enlarge to become **Dalmatian spots**, some of which form **fried-egg** halos; these enlarge to consume the seasonal cap. Only the topographic ghosts of the spiders persist through the summer.

Here is a short list of remaining known puzzles, it seems sure to grow!:

- The basis for the geographic distribution of cryptic terrain.
- Why do cryptic regions repeat year to year?
- The basis for the location and spacing of the fans and spiders.
- The causal process for the dark halo "fried eggs".
- Quantitative theory of the formation and velocities of dust bubbles.

THEMIS thermal images of the evolution of this menagerie are expected to be quite helpful in elucidating the processes.

## References

- [1] J. Eluskiwicz. On the microphysical state of the Martian polar caps. *Icarus*, 103:43–48, 1993.
- [2] F. Forget, F. Hourdin, and O. Talagrand. CO<sub>2</sub> snowfall on Mars: Simulation with a general circulation model. *Icarus*, 131:302–316, 1998.
- [3] R. Greeley, N. Lancaster, S. Lee, and P. Thomas. Martian aeolian processes, sediments, and features. *Mars, edited*

- by H.H. Kieffer et al., Univ. of Ariz. Press, Tucson, pages 730–766, 1992.
- [4] G. B. Hansen. The infrared absorption spectrum of carbon dioxide ice from 1.8 to 333 micrometers. *J. Geophys. Res.*, 102:21569–21587, 1997.
- [5] S. L. Hess. Static stability and thermal wind in an atmosphere of variable composition. *J. Geophys. Res.* 84, 2969-2973, 1979.
- [6] A. P. Ingersoll. personal communication. 2000.
- [7] R. A. Kahn, T. Z. Martin, R. W. Zurek, and S. W. Lee. The Martian dust cycle. *Mars*, edited by H.H. Kieffer et al., Univ. of Ariz. Press, Tucson, pages 1017–1053, 1992.
- [8] H. H. Kieffer. Near infrared spectral reflectance of simulated Martian frosts. *Ph.D thesis*, Calif. Inst. Tech, 1968.
- [9] H. H. Kieffer. Spectral reflectance of CO<sub>2</sub>-H<sub>2</sub>O frosts. *JGR*, 75:501, 1970.
- [10] H. H. Kieffer. Annual punctuated CO<sub>2</sub> slab-ice and jets on Mars. In second International Conference on Mars polar science and exploration, 2000. Reykjavik, Iceland. LPI Contribution no. 1057.
- [11] H. H. Kieffer, T. N. Titus, K. F. Mullins, and P. Christensen. Mars south polar spring and summer behavior observed by TES: Seasonal cap evolution controlled by frost grain size. *J. Geophys. Res.*, 105(E4):9653–9699, 2000.
- [12] S. Piqueux, S. Byrne, and M. Richardson. The sublimation of Mars' sputern seasonal CO<sub>2</sub> ice cap and the formation of spiders. *J. Geophys. Res.*, submitted, 2003.
- [13] P. C. Thomas, R. Sullivan, A. P. Ingersoll, B. C. Murray, G. E. Danielson, K. E. Herkenhoff, L. Soderblom, M. C. Malin, K. S. Edgett, and P. B. James. The residual polar caps of Mars: Geological differences and possible consequences. In *Second International Conference on Mars Polar Science and Exploration*, page 172, aug 2000.
- [14] T. N. Titus, H. H. Kieffer, and K. F. Mullins. Slab ice and snow flurries in the Martian polar night. *J. Geophys. Res.*, 106(E10):23,181–23,196, 2001.
- [15] M. G. Tomasko, L. R. Doose, M. Lemmon, P. H. Smith, and E. Wegryn. Properties of dust in the martian atmosphere from the imager on Mars Pathfinder. *J. Geophys. Res.*, 104:8987–9008, 1999.
- [16] R. W. Zurek, J. R. Barnes, R. M. Haberle, J. B. Pollack, J. E. Tillman, and C. B. Leovy. Dynamics of the atmosphere of Mars. *Mars*, edited by H.H. Kieffer et al., Univ. of Ariz. Press, Tucson, pages 835–933, 1992.

**THE MINIATURIZED MÖSSBAUER SPECTROMETER MIMOS II OF THE ATHENA PAYLOAD FOR THE 2003 MER MISSIONS.** G. Klingelhöfer<sup>1</sup>, R.V. Morris<sup>2</sup>, P.A. de Souza Jr.<sup>3</sup>, B. Bernhardt<sup>1</sup>, and the Athena Science Team, <sup>1</sup>Institut f. Anorganische u. Analytische Chemie, Joh. Gutenberg-Universität, Staudinger Weg 9, D-55099 Mainz, Germany (klingel@mail.uni-mainz.de), <sup>2</sup>ARES, NASA Johnson Space Center, 77058 Houston, TX, USA, (richard.v.morris@nasa.gov), <sup>3</sup>Departamento de Pelotização, Companhia Vale do Rio Doce, 29090-900 Vitória, ES, Brazil, (paulo.antonio.souza@cvr.com.br)

**Introduction:** A first-order requirement of space-craft missions that land on Mars is instrumentation for in situ mineralogical analysis. Mössbauer Spectroscopy is a powerful tool for quantitative analysis of Fe-bearing materials. The Athena Mössbauer spectrometer MIMOS II on the martian surface will provide (1) identification of iron-bearing phases (e.g., oxides, silicates, sulfides, sulfates, and carbonates), (2) quantitative measurement of the distribution of iron among its oxidation states (e.g., Fe<sup>2+</sup>/Fe<sup>3+</sup> ratio), and (3) quantitative measurement of the distribution of iron among iron-bearing phases (e.g., the relative proportions of iron in olivine, pyroxene, and magnetite in a basalt) in rocks and soils. Mössbauer data will also be highly complementary with chemical analyses from the APXS and the Mini-TES compositional data. Mars is a particularly good place to do Mössbauer mineralogy because its surface is iron rich (~20% Fe as Fe<sub>2</sub>O<sub>3</sub> [1-3]). Mössbauer spectrometers that are built with backscatter measurement geometry require no sample preparation, a factor important for in situ planetary measurements.

**The Mössbauer Effect:** Iron Mössbauer spectroscopy makes use of the resonance absorption of 14.4 keV  $\gamma$ -rays (the Mössbauer effect) by <sup>57</sup>Fe nuclei (2.2% natural abundance) in a solid to investigate the splitting of its nuclear energy levels that is produced by interaction with the surrounding electronic environment. <sup>57</sup>Co, which decays to the proper excited state of <sup>57</sup>Fe, is normally employed as the source of the  $\gamma$ -rays. In general, the nuclear energy level structure of the absorber will be different from that of the <sup>57</sup>Co source (because of different oxidation states, chemical environments, and/or magnetic order), which requires modulation of the energy of the source  $\gamma$ -rays to achieve resonance. This is done using the Doppler effect, by mounting the <sup>57</sup>Co source on a velocity transducer and moving it with respect to the absorber. A backscatter (transmission) Mössbauer spectrum is the relative number of  $\gamma$ -rays per second re-emitted from (passing through) an absorbing sample as a function of the relative velocity between the source and sample. Phase and oxidation state identification are determined from peak locations in the Mössbauer spectrum, and peak areas are measures of concentration. The Mössbauer parameters are temperature dependent, and therefore the Mössbauer spectrum will

depend on the measurement temperature. In addition the properties of the absorber may vary as a function of temperature and therefore the MB spectrum.

**The MIMOS Instrument:** The MIMOS II Mössbauer spectrometer system, which is designed and fabricated at the University of Mainz (e.g.[4]), was originally developed for inclusion on the Russian Mars 98 rover mission. Since then, it has gone through several generations of evolutionary prototypes, finally emerging in the built of the flight units for the NASA Mars-Exploration-Rover 2003 twin-mission and the ESA Mars-Express-Beagle-2 2003 lander mission. In preparation of these missions a prototype MIMOS II instrument was successfully tested (data taken under semi-real conditions) on the Rocky-7 Mars prototype rover during the May, 1997, field tests in the Mojave desert [1], and on the FIDO rover during the May 1999 field tests at Silver Lake, California. The MIMOS II system is intrinsically simple, rugged, and has sufficient radiation shielding to protect personnel and other instruments. For Athena, the instrument is split into two parts: the detector head is mounted on a robotic arm and the printed circuit board, which has the circuitry for the instrument control, data acquisition and storage, and communications, is located in the rover's warm electronics box. The main components of the detector head are the <sup>57</sup>Co radiation source and shielding, velocity transducer (drive), and silicon PIN diode radiation detectors and their pre- and main-amplifiers. The <sup>57</sup>Co source is embedded in a solid rhodium metal matrix which is attached to a titanium holder. The drive has a unique miniature double voice coil electromechanical design. The total weight of the MIMOS II is about 500 g (400 g for the detector head and 100 g for the printed circuit board, not including the harness). The dimensions of the instrument are about 90mm x 50mm x 40mm for the sensor head, and 160mm x 100mm x 25 mm for the electronics board. The power consumption is in the order of 2 W. The instrument has been fully tested over the expected temperature range (operating: -120°C to +40°C Sensor head; -50°C to +40°C electronics board).

## MINIATURIZED MÖSSBAUER SPECTROMETER MIMOS II: G. Klingelhöfer et al.

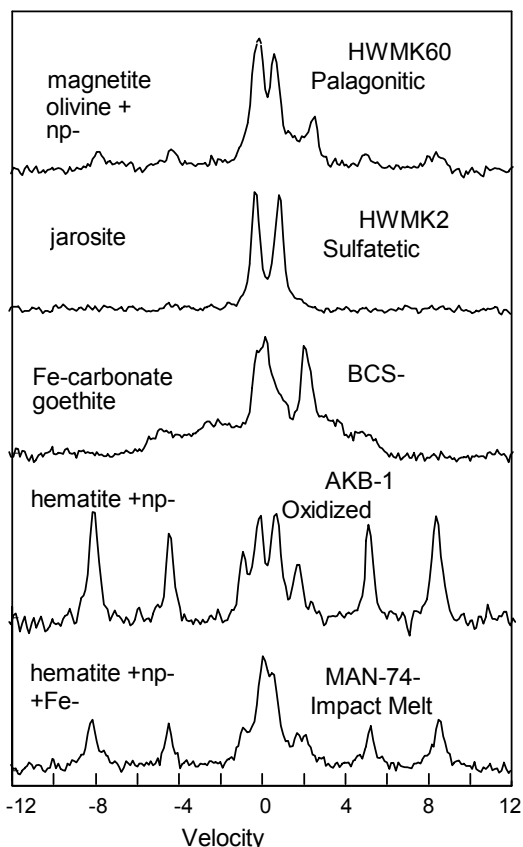


Figure 1. Backscatter Mössbauer spectra ( $\sim 290$  K) obtained with the MIMOS II instrument for Martian surface analogues (after [5]).

The  $^{57}\text{Co}$  radioactive Mössbauer source intensity of about 300 mCi at launch will give a 6-12 hr time for acquisition of a standard MB spectrum on Mars, depending on total Fe content and which Fe-bearing phases are present. Measurements will be done by placing the detector head against the rock or soil to be analyzed. Physical contact is required to minimize possible microphonic noise on the velocity-modulated energy of the emitted  $\gamma$ -rays. The field of view of the instrument is circular (diameter  $\sim 1.5$  cm). The average information depth for Mössbauer data is 200 to 300  $\mu\text{m}$ , assuming basaltic rock composition. The instrument monitors temperature, and adjusts integration periods to assure that the variation in ambient surface temperature during acquisition of a single spectrum is not larger than about  $\pm 10$   $^{\circ}\text{C}$ , minimizing spectral smearing associated with temperature-dependent mode. Figure 1 shows backscatter Mössbauer spectra obtained with the MIMOS II instrument in the laboratory for five Martian surface analogue samples [5]. Figure 2 and 3 show some of the spectra obtained with the flight instrument during the Athena payload integrated systems test in May 2000 at JPL.

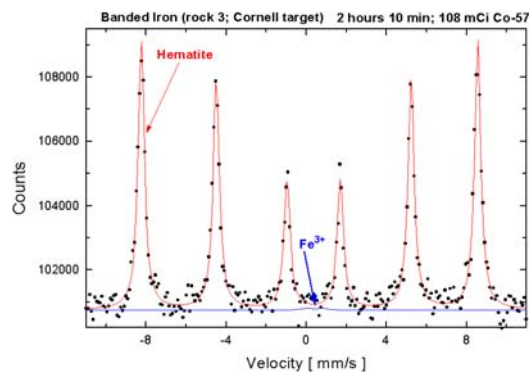


Figure 2. Backscatter Mössbauer spectrum ( $\sim 290$  K) of a sample of Banded Iron Formation (BIF), obtained with the MIMOS II flight unit during APEX system test May 2000. The spectrum is dominated by the hematite signal (red six line pattern). A minor contribution (close to zero) of a  $\text{Fe}^{3+}$  doublet component might be present.

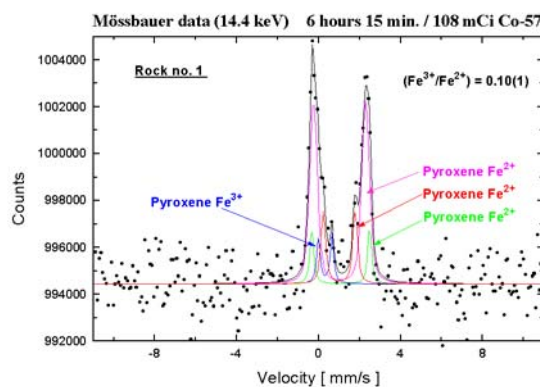


Figure 3. Backscatter Mössbauer spectrum ( $\sim 290$  K) of a sample of a rock composed of 40% Fe-rich pyroxene, obtained with the MIMOS II flight unit during APEX system test May 2000. The spectrum is dominated by a pyroxene signal ( $\text{Fe}^{2+}$ ), with a 10% (whole spectrum area) contribution of an  $\text{Fe}^{3+}$  doublet component, also belonging probably to the pyroxene mineral.

**Calibrations:** Comparison of Mössbauer spectra (293 K) in backscatter and transmission geometries for Martian analogue samples were performed. An example is depicted in Figure 4. Backscatter spectra (512 velocity channels folded to 256 channels) were obtained using a prototype MER spectrometer, and transmission spectra (1024 velocity channels folded to 512 channels) were obtained using a laboratory spectrometer. HWMK600 and HWMK24 are the  $< 1$  mm

## MINIATURIZED MÖSSBAUER SPECTROMETER MIMOS II: G. Klingelhöfer et al.

size fractions of palagonitic and jarositic tephra from Mauna Kea Volcano (Hawaii). AKB-1 and BCS-301 are an amygdaloidal basalt (Michigan) and an iron ore (Lincolnshire, England). MAN-74-342A is an impact melt rock from Manicougan Crater (Quebec, Canada). Mössbauer spectra depicted in Figure 4 are adapted from Morris et al. [6-9].

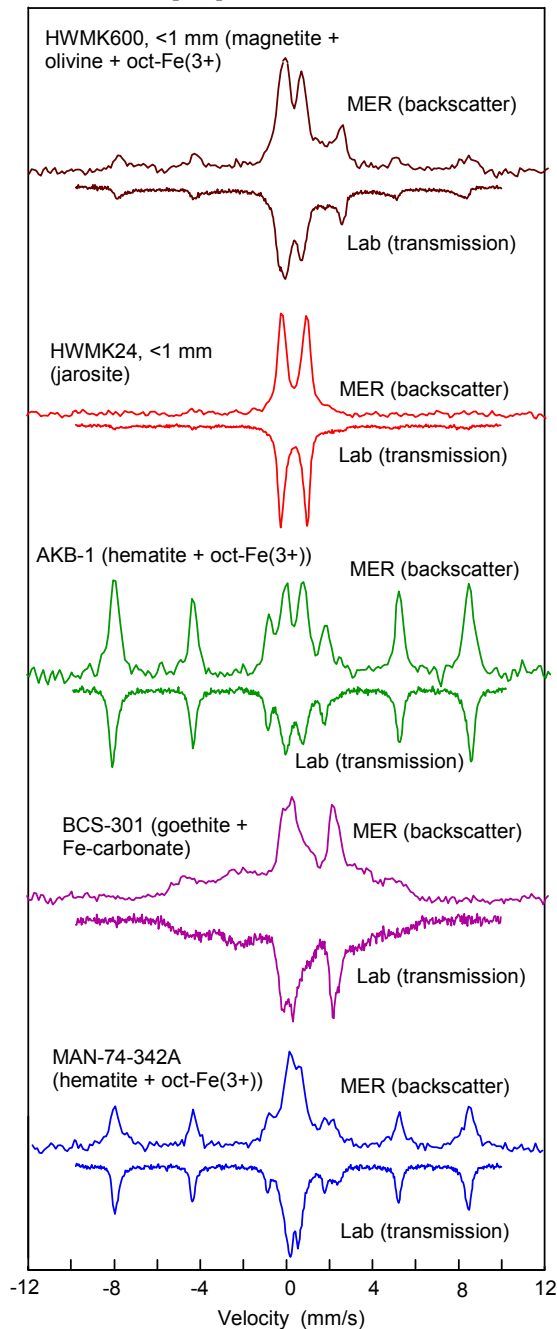


Figure 4. Comparison of Mössbauer spectra (293 K) in backscatter and transmission geometries for Martian analogue samples.

**Data Analysis:** A very specific Mössbauer data base were build taking into consideration the needs of

the Mars Missions. The information published at the literature were carefully analyzed. The most relevant variables that may lead to changes of the Mössbauer parameters of each mineral were reported in the data base records. The stored Mössbauer parameters were used to train an artificial neural network making possible a fast and save mineral identification from its measured Mössbauer parameters [10, 11]. Before the first Mössbauer spectrum being obtained on Mars surface, early in 2004, several and exhaustive tests are planed to be carried out.

**References:** [1] Arvidson, R.E., et al., *J. Geophys. Res.*, 103, 22671-22688, 1998. [2] Clark, B. C., et al., *J. Geophys. Res.*, 87, 10059-10067, 1982. [3] Rieder, R. et al. (1997) *Scienc*, 278, 1771-1774. [4] Klingelhofer, G., et al., *Planet. Space Sci.*, 44, 1277-1288, 1996. [5] Morris, R. V., et al (1998) *Lunar and Planetary Science XXIX*, Abstract # 1326. [6] Morris, R. V., Ming, D. W., Golden, D. C., and Bell III, J. F. (1995) in *Mineral Spectroscopy: A Tribute to Roger G. Burns*, edited by M. D. Dyar, C. McCammon, and M. W. Schaefer, pp. 327-336, The Geochemical Society, Special Publication No. 5, Houston. [7] Morris, R. V., Golden, D. C., Bell III, J. F. and Lauer Jr., H. V. (1995) *J. Geophys. Res.*, 100, 5319-5328. [8] Morris, R. V., Squyres, S. W., Bell III, J. F., Economou, T., Klingelhofer, G., Held, P., Haskin, L. A., Wang, A. Jolliff, B. L., and Rieder, R. (1998) *Lunar Planet. Sci. [CD-ROM], XXIX*, abstract # 1326. [9] Morris, R. V., Golden, D. C., Bell III, J. F., Shelfer, T. D., Scheinost, A. C., Hinman, N. W., Furniss, G., Mertzman, S. A., Bishop, J. L., Ming, D. W., Allen, C. C. and Britt, D. T. (2000) *J. Geophys. Res.*, 105, 1757-1817. [10] De Souza Jr. P. A. (1999) *Lab. Rob. Autom.* 11, 3-23. [11] De Souza Jr. P. A. and Klingelhöfer, G. (2001) *MAPS*, 36, Suppl. A, 139.

**Acknowledgments:** This work is funded by German Space Agency (50QM92081). Support by CAPES (PAJS 142-1999), CST Steelwork and CVRD are acknowledged. The authors wish to thank D. Rodionov, J. Foh, E. Kankeleit, R. Gellert, Ch. Schroeder, S. Linkin, E.Evlanov, B.Zubkov, O. Prilutski, P. Guetlich, W. Tremel, B. Fegley, Jr. And Steve Squyres (PI, MER mission) for their valuable contributions to this work.

**PLANETARY MICRO-END EFFECTORS**

S.M. Ko<sup>1</sup>, T.C. Ng<sup>2</sup>, K.L. Yung<sup>1</sup>, C.H. Yu<sup>1</sup>, and C.C. Chan<sup>3</sup>

<sup>1</sup>The Hong Kong Polytechnic University (mfsuimko@inet.polyu.edu.hk, mfklyung@inet.polyu.edu.hk, icchyu@inet.polyu.edu.hk) <sup>2</sup>Dentist (holinser@vol.net), <sup>3</sup>SolidWorks Corporation (ccchan@solidworks.com.hk).

**Abstract:**

The Micro-End Effectors (MEE) system was developed by The Hong Kong Polytechnic University covers all aspects of planetary explorations.

All sampling tools can be divided into six catalogues:

- 1) Surface sampling
- 2) Subsurface sampling
- 3) Surface coring
- 4) Subsurface coring
- 5) Zero gravity sampling
- 6) Rind Grinding

It is designed for long hauled missions with low payload. e.g. Titan- Europa Planets with exobiology values and Mars Rock Corer is responsible for the world 1<sup>ST</sup> planetary rock coring in our solar system for ESA 2003 Beagle 2 Mars Lander.

For more information,  
please visit <http://www.hkmars.net>

## MORPHOLOGY OF THE HIGH-LATITUDE MANTLE IN NORTHERN PLAINS ON MARS.

V.-P. Kostama<sup>1</sup>, M. A. Kreslavsky<sup>2,3</sup> and J. W. Head<sup>2</sup>, <sup>1</sup>Astronomy, Dept. of Physical Sciences, University of Oulu, Oulu, FIN-90014, Finland; <sup>2</sup>Dept. Geological Sci., Brown University, Providence, RI 02912-1846, USA; misha@mare.geo.brown.edu, <sup>3</sup>Astronomical Institute, Kharkov National University, Kharkov, Ukraine.

**Introduction:** The complex of polar deposits (the polar cap, its icy outliers and dune fields) at the North pole of Mars is surrounded by vast generally flat geologically homogeneous plains. These plains at high latitudes ( $>55^\circ$ ) are covered with a thin geologically young mantle with specific decameter-scale surface texture [1, 2] containing much water ice [3, 4]. High-resolution MGS MOC images [1] showed many circular features interpreted to be mantled craters [1] (see Fig. 118, 119 there). Our objective is to access geological processes that occurred in the region during the Amazonian, and the relative and absolute time scales of these processes, including those related to the origin of the shallow subsurface ice. To approach this goal, we studied the size-frequency distributions of circular features of different morphology, as well as peculiarities of the surface texture. We are carrying out a systematic survey of the high-resolution MOC images in the region. This work is in progress; here we report some preliminary observations.

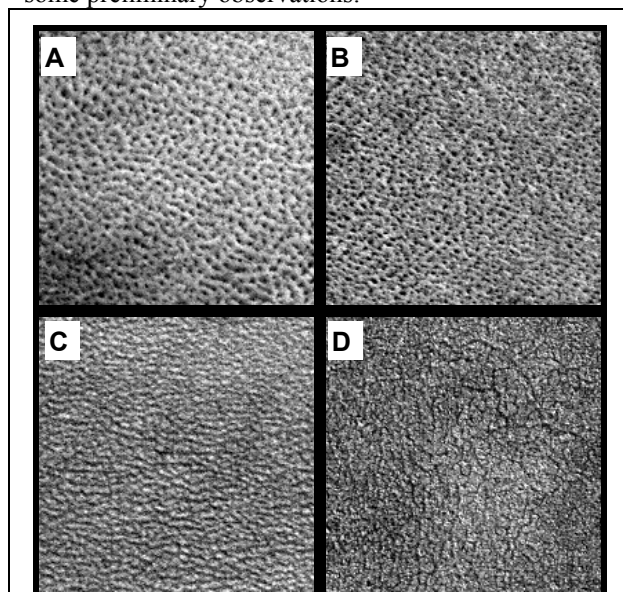


**Fig. 1.** Typical textures of the mantle in the northern plains: **A** - basketball texture, **B** - regular texture, **C** - wrinkle texture, **D** - polygonal texture. Portions of E01/01975, E04/00026, E01/01868, and E04/00028, respectively. Samples are 0.9 x 0.9 km, illumination is from lower left.

**Survey:** We systematically overview the mantle texture, study morphology and measure diameters of the circular features in the northern plains northward from  $55^\circ\text{N}$  using the narrow-angle MOC images. For the systematic survey we use images of 4.8 m/pix reso-

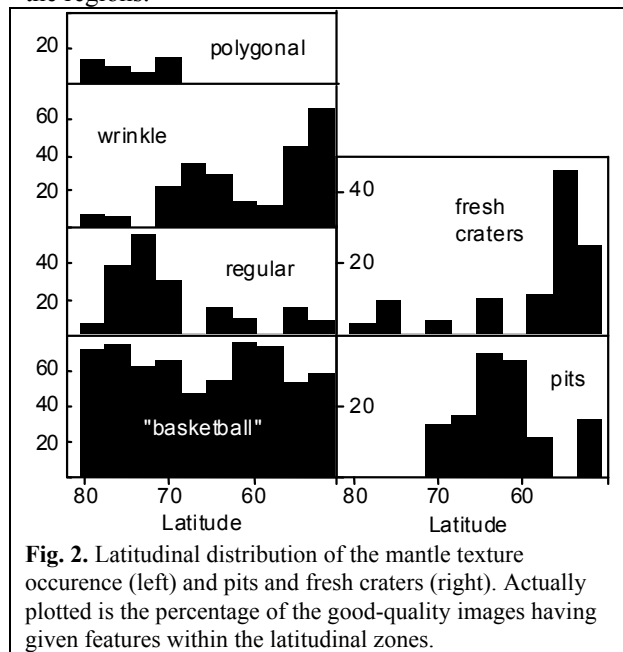
lution. This resolution was chosen because a large number of such images were taken during cycles from E01 to E05, when observational conditions in the region were mostly good. For each image, we register the morphological types of mantle texture present in the image, and classify and measure all circular features from 50 m to 1 km. Although we try to do the survey as homogeneously as possible, the ability to identify the features and textures differ from image to image due to the differences in atmospheric scattering, illumination geometry, presence of contrasting albedo features on the scene, electronic settings of the camera, etc. Consequently, analyzing the survey results, we should be aware of possible latitudinal (illumination) and regional (albedo pattern) biases. Nevertheless, we are sure, that in the surveyed images we identified all fresh features larger than 50 m that disrupt the mantle.

**Texture:** In the northern plains, the mantle has very distinctive decameter-scale surface textures seen in the images (**Fig. 1**). The "basketball" texture (**A in Fig. 1**; also Fig. 123 D in [1]) is the most typical and wide-spread one. The best highest-resolution (1.6 m/pix) low-sun images show that the knobs are dome-shaped, with the steepest slopes  $<6^\circ$ . In some places, the knobs forming the basketball texture are organized into highly coherent linear structures (**Fig. 1 B**, see also Fig. 123 E in [1]) forming a *regular texture*. The *wrinkle texture* (**Fig. 1 C**) is also very common. The *polygonal texture* (**D**) occurs rarely and in relatively small patches (several km). Spatial scale of the textures differs from site to site for a factor of 3; often it is smaller than shown in Fig. 1. The texture of the shortest spacing is often hardly distinguishable in the images. The polygonal texture of the mantle differs from polygons that are observed in a number of sites in the northern lowlands and have typical morphology and pattern of the terrestrial permafrost regions (e.g., Fig. 123 B in [1]). The latter polygons have an order of magnitude larger spacing and different morphology.

Local variations of the patterns are often modulated by kilometer-scale topography. More pronounced basketball texture tends to occur in local lows. The wrinkle texture on slopes of km-scale knobs has a radial orientation.

There are latitudinal variations in the patterns. Latitudinal occurrence of them is illustrated in Fig. 2. The regular texture tends to occur at higher latitudes. The polygonal texture occurs at high latitudes above  $70^\circ\text{N}$

only. Wrinkle texture is rare in this high-latitude zone. There are also some regional variations. They can be biased because of different observational conditions in the regions.



**Erosion:** The mantle is surprisingly continuous in 60-80° latitude zone. At the highest latitudes there are several examples where the mantle is eroded on steep slopes exposing its layered structure. Below 60° latitude the erosion is ubiquitous and occurs not only on slopes, but also on flat surfaces. Often erosion of the mantle produced specific dissected patterns described and surveyed in [6]. We saw clear examples showing that the typical dissection from [6] is dissection of the mantle with characteristic basketball texture. In many sites, however, the dissection does not take place, and the eroded edges of the mantle form lobate scarps.

**Modified circular features:** Circular features in the northern plains have a wide range of morphologies from well-expressed impact craters covered with the textured mantle (**Fig. 3A**) to hardly distinguishable circular chains of lineaments and/or arcuate albedo markings (**Fig. 3B** upper left). The ability to distinguish features of the latter type strongly depends on the observational conditions and the presence and nature of the albedo markings on the surface. In addition, for such features it is not clear what should be considered as the feature diameter. When circular lineament chains were observed, we used the outermost circle for diameter measurements. If only albedo markings were seen, we used the inner arcuate albedo contrast, because in many cases where both lineaments and markings are present, the markings were outside the lineaments. Impact origin of features of this type is not

completely clear. They are usually associated with local highs (gentle knobs forming the surface of the Vastitas Borealis Formation). We found a series of transitional morphologies between clearly expressed impact craters (**Fig. 3A**) and the subtle features, which can be considered as evidence for their impact origin.

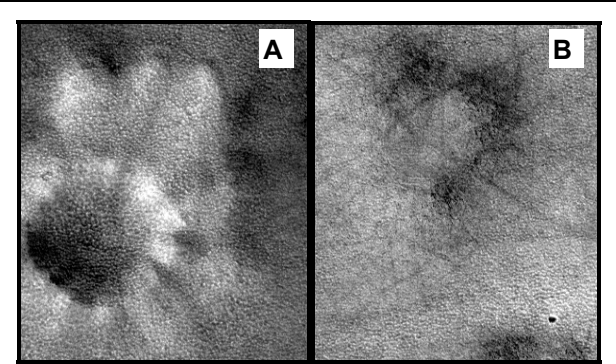


**Fig. 3.** Two portions of E02/01380, 1.4 km wide. Illumination is from lower left. B has 30% higher contrast than A. A, impact crater, covered with mantle. B, subtle circular feature in the upper left, fresh small impact crater (60 m) in the lower right.

The size-frequency distribution of all modified circular features is close to that should be expected for an accumulation population of the impact craters [5], with some shortage for small diameters, which is natural, taking into account strong degradation and alteration processes.

We are not sure, however, that all mantled circular features in the region are old modified impact craters. In some images they are apparently too clustered to represent randomly accumulating population. The clustering might result from regional variations of mantling and modifications; the clusters can be formed with secondary craters from large distant impacts; finally, the features could have endogenous origin.

**Pits:** In the 55°N -70°N zone there is a number of examples of small circular or quasi-circular depressions not similar to impact craters in their morphology. Some of such features clearly have collapse origin. There are several large clusters of pits, some of the pits in the clusters are fresh, but the majority of them are covered with the typically textured mantle (**Fig. 4**). Many pits have a form of concentric steps (**Fig. 4B**); the steps are probably related to several layers of the mantle. There are examples where the pits are covered with mantle with characteristic texture, while the small patch at the bottom looks fresh, which could mean reactivation of the collapse process. The size-frequency distribution of the pits in the clusters is steeper than the impact crater production function. This means that the pits can hardly be a result of the impact crater degradation.

**Fresh craters:** At the high latitudes ( $>70^{\circ}\text{N}$ ) the mantle is mostly intact, with some erosion and removal at the steepest slopes of large ( $>10$  km) impact craters. So far, we identified 4 small circular features, almost certainly impact craters superposed on the mantle and somewhat degraded.

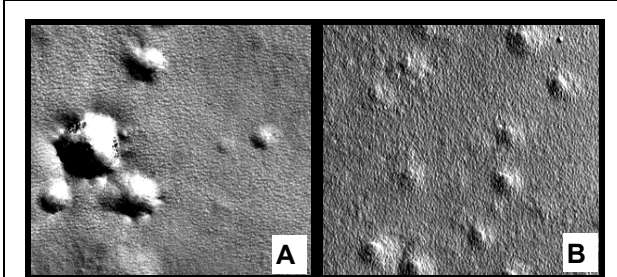


**Fig. 4.** **A.** Portions of E02/00200. A few pits; the largest one is a fresh collapse feature with steep slopes, others pits are covered with the mantle in different degrees. **B.** Portions of E02/01984. Pits covered with the mantle. Small sharp feature in the upper right corner could be a fresh impact crater (40 m). Both images are 1.4 km wide; illumination is from lower left.

Several images at latitudes  $<70^{\circ}\text{N}$  contain a set of small sharp circular depressions, apparently randomly scattered over the image; a few of them sometimes are larger than 50 m, other are smaller (see examples in **Fig. 3B, 4B**). This situation is very similar to that should be expected for an accumulating population of impact craters. There are a few tight pairs of small craters in such images, which is natural because of probable breakup of small projectiles in the atmosphere. The crater density calculated over several images with such probable impact crater population gives an age estimate on the order of 1 Myr, using the Neukum production function recalculated for Mars [5]. This estimate is highly uncertain, because (1) this is statistics of a few craters; (2) the recalculation of the production function is accurate within a factor of 2 [5]; (3) the extrapolation of the projectile flux established for 100s Myr time scale down to 1 Myr time scale is poorly grounded; (4) atmospheric attenuation of the projectile flux is uncertain.

There are many images in the lower latitudes ( $55^{\circ}\text{N}$  -  $60^{\circ}\text{N}$ ), where there are definitely no impact features. This observation suggests, that the crater retention age of the mantle in different locations differs at least by an order of magnitude. The crater retention age difference can be explained in two ways. (1) Mantle emplacement age can differ between high and lower latitudes, and between different areas at lower latitudes. This means that there were many episodes of the mantle emplacement. The contacts between mantles of different age may not be recognized as such because the MOC image coverage is too patchy. This

question about the presence of such boundaries can be addressed with Mars Odyssey THEMIS visible and day infrared images. (2) A large part of the mantle could be protected from impacts by a decameters-thick layer of icy deposits similar to the present polar cap outliers and persisted during long part of the mantle lifetime span. The polar cap contains much enough ice to provide necessary material for this coverage. Relatively recent sublimation of such protecting layer and migration of the ice to the northern polar cap can form hectometers-thick young layer on the cap and be responsible for its young crater retention age [e.g., 7]. Areas with accumulating population of fresh impact craters at lower latitudes can be due to gaps in the protecting ice sheet at lower latitudes.

Formation of the high-latitude mantle or its individual layers is probably attributed to periods of high obliquity [e.g., 2], when atmospheric water abundance and mobility were higher, and winds and dust lifting were more intensive. The accuracy of age determination with craters do not allow to distinguish between the most recent periods of moderately high ( $\sim 35^{\circ}$ ) obliquity about 0.3 Ma ago and extremely high ( $>40^{\circ}$ ) obliquity at earlier periods ( $>4$  Ma ago) [8].

**References:** [1] Malin M. C. and Edgett K. S. (2001) *JGR* 106, 23429-23570. [2] Kreslavsky M. A. and Head J. W. (2002) *GRL* 29, 10.1029/2002GL015392. [3]. Tokar R. L. et al. (2002) *GRL*, 29, 10.1029/2002GL015691. [4] Mitrofanov, I. G. et al. (2003) *LPS XXXIV*, Abstract # 1104. [5] Ivanov B. A. (2001) *Space Sci. Rev.*, 96, 87. [6] Mustard, J. F. et al. (2001) *Nature*, 412, 411-414. [7] Herkenhoff, K. E. and Plaut, J. J. (2000) *Icarus*, 144, 243-253. [8] Laskar, J. et al (2002) *Nature*, 419, 375-377.

**Enigmatic Surface Features of the South Polar Layered Deposits.** M. R. Koutnik<sup>1</sup>, S. Byrne<sup>2</sup>, Z. Crawford<sup>3</sup>, and B. C. Murray<sup>2</sup>, <sup>1</sup>University of Washington (Box 351310, Seattle, WA 98195, mkoutnik@geophys.washington.edu), <sup>2</sup>California Institute of Technology (shane@gps.caltech.edu, bcm@gps.caltech.edu), <sup>3</sup>University of Colorado (zane.crawford@colorado.edu).

**Introduction:** Data from the Mars Orbiter Camera (MOC) and the Mars Orbiter Laser Altimeter (MOLA) aboard the Mars Global Surveyor (MGS) mission have provided important new clues to the past history of the south polar layered deposits (SPLD). There are distinct features presented here that have been observed almost exclusively with these data sets and are unique to the south polar region of Mars. Crawford *et al.* [1] have studied these features initially and we now present the current perspective on this region after a period of detailed study. We present a descriptive discussion and provide evidence for different possible interpretations. Although we do not conclusively know the origin of these features, we consider that subglacial volcanism as well as strong surface winds may have been active in forming these features visible today.

**Regional Description:** Enigmatic large-scale grooved features, termed here the “Wire Brush” terrain, became evident from the MOLA topographic shaded relief map. The precise topography data was better suited to expose subtle surface features that were poorly resolved in visual images. This region can be identified in Viking coverage of this area (image f307a88) and shows that the grooves possibly have a connection with the current residual cap. This unusual area of grooved terrain occurs in the region 190° - 230° W, 85° - 87°S (no MGS coverage south of 87°), shown in Figure 1 and Figure 2. At the poleward tip of Chasma Australe is the only other location where we see this grooved pattern on Mars. The grooves are suggestive of erosion by an external agent that maintained a coherent pattern over several hundred km scale.

The overall grooved pattern is continuous for more than 300 km, though tracing of individual grooves is difficult to do with certainty for more than about 50 km. The grooves do continue linearly across local topography and are several hundreds of meters across with vertical relief of only a few tens of meters. The slope over the extent of the wire brush terrain is very slight and the grooves do not seem to be influenced by any larger scale topography. The grooves also seem to cut right across smaller topographic features, not deflected by them in local areas. This is shown in Figure 3. A feature observed using the MOLA data has been resolved in the MOC Narrow Angle (NA), showing how the linear grooves cut right over a circular feature (example image m1001286). Using the MOC NA images it is also possible to observe that individual grooves have undergone significant weathering (example image m1200517).

There are numerous, unique features in association with the Wire Brush that may provide other clues to origin and timing of formation of the large-scale grooves. There are sinuous positive features cross-cutting the Wire Brush which we have termed “Snakes”. The association of the Snakes with the Wire Brush Terrain is highlighted in Figure 2. The Snakes are as much as 2 km in width and tens of km long, though are only a few tens of meters in relief relative to

the surrounding terrain. The presence of such vertical features is unusual. It could imply an episode of deformation or fracturing that has been filled subsequently with more resistant material than the surrounding layered deposits. Individual snakes have differing structural properties and differing appearances in MOC NA image coverage. Some of the Snakes appear to expose many layers on one side and none on the other, whereas other Snakes seem to show no layering at all. The Snakes are found primarily within the Wire Brush region but do extend out from this region as well. One Snake extends into an adjacent elongated depression and can be seen to interact with layering in this adjacent chasma. The walls of the chasma are finely layered and these layers are continuous, traceable over tens of km through different MOC NA frames. The layers near the location where the Snake coincides with the wall of this chasma are highly deformed. MOC NA m1002701 illustrates this deformation of the layers by the Snake feature. This adjacent chasma is possibly a significant feature in association with the Wire Brush terrain. Unlike Chasma Australe, this chasma does not cut all the way through the layered terrains to the underlying basement rock and does not have an outlet. Given the positions of these two chasmas, on both sides of the Wire Brush Terrain, it is possible that all of these features have a similar origin.

Another interesting component of the Wire Brush and adjacent region is the presence of small, circular pits. They are found distinctly in the regions 190° - 230° W, 85° - 87° S and 135°-175° W, 85°-87° S. A search of the south polar layered deposits using MOC imagery data through extended mission 12 (e-12) has been done in the search area for impact craters designated by Koutnik, *et al.*[2]. Out of this entire search area, these potholes are found only within the two bounds listed above. Most interesting is that the potholes are predominantly found in association with the Wire Brush Terrain.

The distribution and morphology of these features is clear evidence that they are not impact craters. There are no large impact craters near these features and the organized clustering of the potholes indicates an endogenic origin. The distribution of these features has been mapped according to coverage in MOC NA images. The potholes are found in two distinct regions and can be roughly grouped by morphology and orientation. All of the individual polar potholes in both regions are approximately 50 – 100 m in diameter. The density of potholes over a given area in each image is variable, though these features are always seen in groupings of multiple features, never isolated. The potholes found within the Wire Brush region are circular, distinct forms. They are often observed with no particular orientation relative to each other or local topography. More interesting, potholes of the same morphology in the Wire Brush region are found to be located in regions of low topography or clustered in local circular depressions. Figure 4 shows the

groupings of potholes in areas of low topography. Figure 5 shows the larger circular depressions containing clusters of small potholes. The larger depressions are 150 – 500 m in diameter in this image and are not distinct features. It is apparent that some of the larger depressions are made up of one or more circular shapes. The entire population of potholes is found only on the south polar layered deposits and these clustered forms are only in the Wire Brush region.

**Interpretations:** The Wire Brush region and associated features could conceivably be the signature of unusual past winds, ancient ice sheet motion, or episodes of catastrophic flooding originating from beneath earlier residual caps. Each of these possible explanations has strong and weak points, though some features are better explained by certain processes than others. The Wire Brush grooves as a wind-formed feature offers a straightforward explanation. This requires an episode of extremely high winds (many tens of m/s) that lasts long enough to carve out these grooves and possibly contribute to the formation of the adjacent chasmas. A possible problem with the wind theory is the nature of the grooves cutting straight over local topography, in a way that seems inconsistent with wind action alone.

Interpretations involving ice motion require a past climate episode where higher temperatures would have allowed a process of this nature to occur. The grooved pattern is visually similar to such features on Earth as ice streams, though we are unable to determine as of now if the mode of formation might be similarly analogous. Evidence for ancient ice streams have been proposed by *Lucchitta* [3] for elsewhere on Mars.

The influence of water over this landscape could also have been important in creating some of the features we see in this region today, if there were a past episode where water was temporarily stable at the surface or near-surface. This could either have been a period of climatic warming or possibly a period of sub-surface volcanism. The presence of a number of peculiar mounds north of the Wire Brush Terrain may be supporting evidence for the influence of sub-surface heating on current topography, as may be the closed depressions of the adjacent chasma. Elsewhere in the south polar region, *Ghatan and Head* [4] have proposed a past episode of subglacial volcanism of Hesperian age. Given that characteristic grooves forming the Wire Brush terrain also appear at the poleward tip of Casma Australe, the formation of this feature might have the same origin. It has been proposed by *Howard* [5] that Casma Australe is a wind-formed feature and has also been proposed by *Anguita et al.* [6] as evidence of a past outburst flood, so there is support for both processes which we consider.

It is possible, perhaps even likely, that several different processes have acted on these unusual features at different times to produce composite results. We are beginning to piece together the connection between all these features in this region of the SPLD, in order to understand their origin. The unique location of all these features is evidence of a significant event in the Martian past that had a considerable influence on the SPLD.

**References:** [1] Crawford, Z., et al. (2002) AGU Fall Meeting. [2] Koutnik, M., S. Byrne, and B. Murray (2002) *J. Geophys. Res.* 107 (E11). [3] Lucchitta, B. (2001) *Geo-*

*phys. Res. Letters* 28, 3, 403-406. [4] Ghatan, G. and J. Head (2002) *J. Geophys. Res.* 107, E7, 2002. [5] Howard, A. (2000) *Icarus* 144, 267-288. [6] Anguita, F. et al. (2000) *Icarus* 144, 302-312.

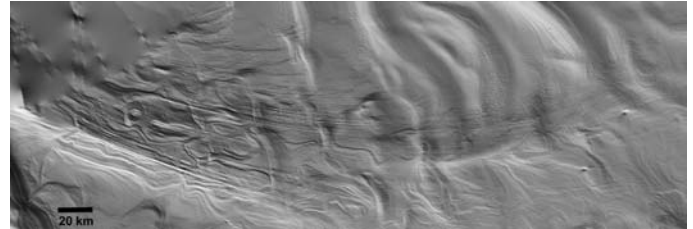


Figure 1. MOLA shaded relief map of the full extent of the Wire Brush Region, 190° - 230° W, 85° - 87°S.

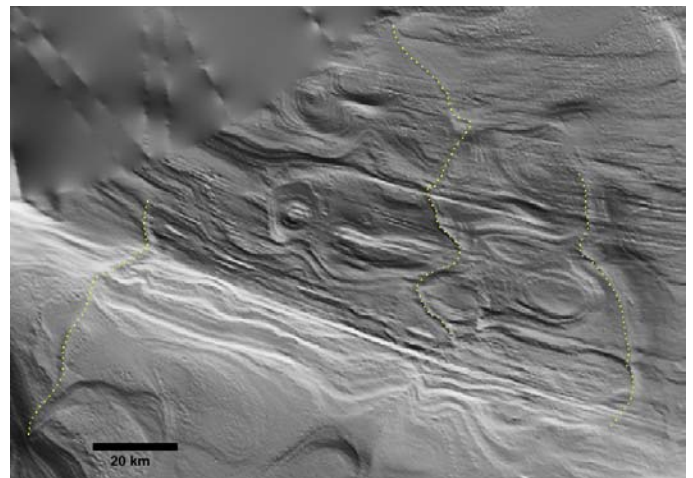


Figure 2. Further zoomed view of the Wire Brush terrain and outlines of the Snakes cutting through this region. The upper left corner is an area where there was no MGS data coverage.

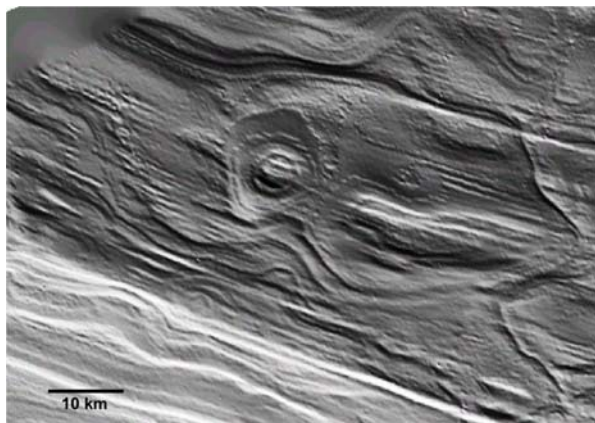


Figure 3. Close-up of topographic feature within the Wire Brush terrain where the grooves cut straight across. Also in the mid-right of this image is a close-up view of one of the Snake features.



Figure 4. MOC NA m1104171 showing the pothole features in the Wire Brush terrain and how they are grouped in regions of lower topography.

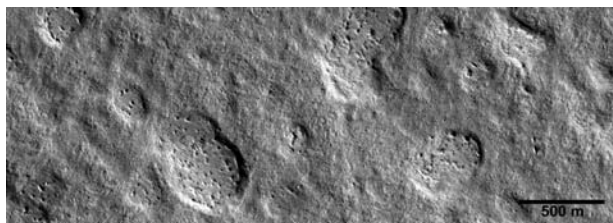


Figure 5. MOC NA m1102900 showing another distribution of potholes in the Wire Brush terrain that are grouped in larger circular depressions.

**CAN SHORELINE PROCESSES ON MARS CONSTRAIN ITS PAST CLIMATE?** E. R. Kraal<sup>1</sup>, E. I. Asphaug<sup>1</sup> and R. D. Lorenz<sup>2</sup>, <sup>1</sup>Department of Earth Science – University of California Santa Cruz (1156 High Street, Santa Cruz, California 95064, ekraal@es.ucsc.edu), <sup>2</sup>Lunar and Planetary Laboratory, (1629 E. University Blvd, Tucson, AZ, 85721).

**Introduction:** Significant past efforts have been devoted to the mapping of shorelines in Martian crater basins [e. g.1, 2-4] and the use of shoreline morphology to interpret the past Martian climate and hydrologic cycle[5-7]. If lacustrine geomorphology persists on Mars, it is a rich key to the Martian past. Yet, despite the wealth of imagery and increasing data return from THEMIS on Mars Odyssey, the interpretation of surface morphology lacks insight from a linked quantitative model. In this spirit, we propose to explore the geomorphic system of a crater lake on Mars and how it would respond to climate perturbations (from occasional filling to persistent lake levels and ice cover), keeping in mind the unique initial conditions of an impact structure to the extent that the initial lake bedrock, breccia and layered deposits can be modeled. *Our ultimate goal is to understand how shorelines might preserve a quantitative record of Martian climate.*

**Methods:** Shore erosion is a function of wave energy reaching the shore and the erodability of shoreline material. Wave energy is a function of climatic variables such as wind speed and variability as well as air pressure. While resistance of shore erosion is a function of bedrock. Through the use of geomorphic modeling, it may be possible to tease out these two variables and begin to understand the climate conditions present during the formation of possible shorelines.

For instance, a shoreline bench of height  $h$  and width  $w$  might turn out to be correlated to a lake drainage of  $h$  over a duration  $T$  with significant wave height  $A$ . In this example  $h$  and  $w$  are directly measured, and  $A$  is a proxy for wind speed and atmospheric pressure. The intensity and duration of climatic events may be recorded in crater lacustrine deposits and erosional forms. A primary goal of our forward modeling effort is, therefore, to determine whether Mars climate history is clearly captured in these erosional and depositional forms.

The modeling is separated into two parts. First, is the generation of waves. Second is the interaction of those waves with the shoreline.

**Wave Formation.** The general wave equations predict expected wave behavior. The velocity of a wave scales with gravity while wave height scales with the inverse of gravity. Therefore, waves produced in the lower gravity of Mars can be expected to grow taller but travel slower.

The energy of a wave is expressed by  $E=1/8\rho gH^2$ , where  $\rho$  is the fluid density ( $\text{gm/cm}^3$ ),  $g$  is planetary gravity ( $\text{m/s}^2$ ), and  $H$  is wave height (m). In order to estimate the amount of energy in the system over time, it is also important to know the wave period.

Empirical equations have been developed for the earth to calculate significant wave height ( $h_s$ ), the average height of waves in the upper one-third of the wave energy spectrum, and the average frequency ( $f_m$ ) of the significant waves. The two empirical relations are the Pierson-Moskowitz(PM) equation, which is only a function of wind speed, and the JONSWAP equation which is a function of wind speed and fetch [8]. This abstract will use the PM equation, which assumes a fully developed sea [9]. The PM equation for significant wave height is:

$${}_{PM} h_s = \frac{0.447 g \sqrt{\rho}}{\rho^2 f_m^2}$$

Where  $g$  is planetary gravity in  $\text{m/s}^2$ ,  $\alpha$  is an empirical constant equal to  $8 \times 10^{-3}$ , and  $f_m$  is the peak frequency. Peak frequency is a function of gravity and the wind velocity,  $u$ , in  $\text{m/s}$

$${}_{PM} f_m = 0.8772 \frac{g}{2 \rho u}$$

Peak period ( $t_m$ ) is  $1/f_m$ . Using these equations it is possible estimate wave energy arriving at Martian shorelines and to compare is to energies at equivalent conditions on Earth.

**Shoreline Development.** From our wave generation model we shall compute the amount of force available to erode a wave cut platform under Martian conditions. Waves provide mechanical energy to erode coastlines by water hammer, abrasion, and quarrying [10]. The highest pressures and erosive power are generally found at the mean water surface [11]. On Earth, the mean water surface is controlled by tides, while on Mars tides are negligible. Trenhaile [12] modeled formation of wave cut terraces on Earth and this method will be closely followed with consideration to Martian conditions.

The wave force ( $F_b$ ) at the point where the wave begins to break is defined as  $F_b = 0.5 \rho_w h_b^3$  (4), where  $\rho_w$  is the density of water and  $h_b$  is the breaking wave depth.  $F_b$  has units of  $\text{kg/m}^2$ . The wave height ( $H_b$ ) is related to  $h_b$  by the critical ratio  $H_b = 0.78 h_b$  (5), which occurs when the water particle velocity at the crest is equal to the wave phase velocity. Combining Eqs. (4) and (5) gives the force at the breakers related to wave

height. This wave force at the breakers must be distributed over the width of the surf zone ( $W_s$ ). Assuming a linearly sloped surf zone  $W_s = h_b / \tan \alpha$  (6) where  $\alpha$  is the slope of the surf zone, the surf force ( $S_f$ ) reaching the water line may be approximated using a decay function  $S_f = 0.5 \alpha_w (H_b/0.78) e^{-k W_s}$  (7). The attenuation rate of energy is represented by the constant  $k$  and is related to the roughness of the bottom. Even in some terrestrial situations this constant can be unknown. However, Trenhaile (2000) showed that a range of 0.1 to 0.01 was ample to model high and low surf attenuation. The wave platform is eroded using this wave force.

**Results:** As anticipated by the basic wave equations, waves produced by the same wind speed are taller on Mars than on Earth. Waves are slower on Mars than on Earth, arriving 3 times less frequently. While gravity varies between the planets, fluid density is assumed to be that of water (1000 g/cm<sup>3</sup>) in both cases. Because of the larger wave height, a given wind speed produces more energetic waves on Mars. Even though this relationship is slightly mitigated by the loss of gravitational potential energy on Mars, average energy per Martian wave is almost 3 times larger than terrestrial waves. However, once the wave period ( $t_m$ ) is converted to number of waves per hour and multiplied by energy per wave, the time averaged energy per wind speed is similar on both planets [13].

Empirical relationships developed on Earth indicate that, given similar wind speeds, the average energy arriving at a Martian shoreline could be comparable to terrestrial wave energy. This conclusion may, however, not be entirely accurate as a 1 bar atmosphere is implicit in the empirical relationship; lower atmospheric density on Mars would make energy transfer from wind to water less efficient. At present, wind wave generation theory based solely on first principles does not exist. It is, therefore, necessary to apply the available tools to make first-order quantitative assessments of the energy available for lacustrine erosion on Mars. Future research will focus on constraining the effects of different planetary conditions on wave field generation, e. g. how atmospheric pressure could be decoupled and thus made explicit for the purpose of general planetary conditions.

The wave fields estimated for various climate conditions (ie wind speed) will be an important input into the geomorphic model of shoreline erosion.

**Conclusions:** By applying terrestrial wave field models, to first order, wave energy on Mars and Earth may be similar. This would especially be true in an early ~1 bar epoch on Mars, when open water might have existed. The presence of open water and a relatively dense atmosphere could provide conditions nec-

essary to form lacustrine geomorphic features. However, more research on the influence of differing planetary conditions and modeling the lacustrine geomorphic processes associated with wave action is necessary and in progress.

This modeling is highly relevant to understanding Mars' water cycle, climate history and geology. Specifically, some aspects of the geologic history of Mars are uncertain because, due to the small size of the impact craters, and the especially small size of potential shoreline features, age dating via crater counting is difficult and controversial (e.g. Hartmann 2002). Although the age of impact crater lakes have been estimated, the error is significant because of their small surface area [6]. Though this model will not result in absolute ages of geomorphic features due to the estimated parameters (e. g. rock hardness and wind speed) we may gain insight into the time of formation; are the observed features likely formed in tens, thousands, or millions of years? The geologic history is inextricably linked to the climate history. The geomorphic modeling of lacustrine features may offer clues to the duration of 'warm, wet' periods.

**References:** [1] Cabrol, N.A. and E.A. Grin, *Distribution, classification, and ages of Martian impact crater lakes*. Icarus, 1999. **142**: p. 160-172. [2] Ori, G., L. Marinangeli, and A. Baliva, *Terraces and gilbert-type deltas in crater lakes in Ismenius Lacus and Memnonia (Mars)*. JGR, 2000. **105**(E7): p. 17629-17641. [3] Moore, J.M. and D.E. Wilhelms, *Hellas as a possible site of ancient ice-covered lakes on Mars*. Icarus, 2001. **154**(2): p. 258-276. [4] Irwin, R., et al., *A large paleolake basin at the head of Ma'adim Vallis, Mars*. Science, 2002. **296**(5576): p. 2209-2212. [5] Cabrol, N.A., et al., *Duration of the Ma'adim Vallis/Gusev Crater hydrogeologic system, Mars*. Icarus, 1998. **133**: p. 98-108. [6] Cabrol, N.A. and E.A. Grin, *The evolution of lacustrine environments on Mars: Is Mars only hydrologically dormant?* Icarus, 2001. **149**: p. 291-328. [7] Cabrol, N.A., E.A. Grin, and R. Landheim, *Ma'adim Vallis evolution: Geomorphology and models of discharge rate*. Icarus, 1998. **132**: p. 362-377. [8] Carter, D.J.T., *Predictions of wave height and period for a constant wind velocity using the JONSWAP results*. Ocean Engineering, 1982. **9**(1): p. 17-33. [9] Pierson, W.J. and L. Moskowitz, *A proposed spectral for fully developed seas*. JGR, 1964. **69**: p. 5181-5190. [10] Sunamura, T., *Geomorphology of Rocky Coasts*. 1992, New York: J. Wiley. [11] Trenhaile, A.S., *The Geomorphology of Rocky Coasts*. 1987, Oxford: Clarendon Press. 384. [12] Trenhaile, A.S., *Modeling the development of wave-cut shore platforms*. Marine Geology, 2000. **166**: p. 163-178. [13] Kraal, E.R., E.A. Asphaug, and R.D. Lorenz. *Wave energy on Mars and Earth: Considering lacustrine erosion*. in 34th LPSC. 2003. League City, Texas.

**METHANE PRODUCTION BY METHANOGENS IN THE ANDROMEDA ENVIRONMENTAL CHAMBER UNDER CONDITIONS APPROACHING THOSE OF THE MARTIAN ENVIRONMENT.** T. A. Kral, D. W. G. Sears, P. H. Benoit, and M. S. Kareev, Arkansas-Oklahoma Center for Space and Planetary Sciences, University of Arkansas, Fayetteville, AR 72701.

**Introduction:** Surface conditions on Mars are probably too hostile for life, as we know it, to exist [1, 2, 3]. Below the surface, however, is another matter. If subsurface liquid water is present [4, 5], then conditions may be conducive to the growth of methanogens. Methanogens, members of the domain Archaea, are microorganisms that are found deep below the surface of the Earth as well as deep within the oceans [6, 7, 8].

**Materials and Methods:** In an attempt to determine if species of methanogens can grow (or just survive) under conditions approaching those at the surface of Mars, we inoculated JSC Mars-1, a Mars soil simulant [9] with *Methanobacterium formicicum*, *Methanosarcina barkeri*, and *Methanothermobacter wolfeii* in the Andromeda Environmental Chamber at the Arkansas-Oklahoma Center for Space and Planetary Sciences. The Andromeda Chamber is a 4 m tall by 1 m wide vacuum cylinder that has been designed to simulate planetary surface conditions. Cultures were grown in their respective media [10, 11], washed and suspended in a standard carbonate buffer, and frozen in anaerobic culture bottles. The frozen cultures were placed inverted into the soil simulant that was in a stainless steel bucket. The bucket was lowered into the chamber, the chamber sealed, and the atmosphere replaced with equal volumes of carbon dioxide and molecular hydrogen at a pressure of 400 mbar. The atmosphere was replaced before the cultures melted in order to prevent the methanogens from coming in contact with atmospheric oxygen (methanogens are strict anaerobes). Palladium catalyst boxes were mounted on the top of the bucket to help re-

move residual oxygen. In some experiments, anaerobic 4.0 mM sodium sulfite solution was poured into the soil as an additional measure to remove residual oxygen [12].

**Results and Conclusions:** All three species survived a week under the described conditions, *M. wolfeii* showing the greatest increase and *M. formicicum* showing the smallest increase in methane production. Sodium sulfite additions resulted in even greater methane production. These experiments demonstrated methane production at reduced pressure, survival of the organisms after a freeze/thaw cycle, and the usefulness of the Andromeda Chamber.

**References:** [1] Klein H. P. (1978) *Icarus*, 34, 666-674. [2] Klein H. P. (1979) *Rev. Geophys. Space Phys.*, 17, 1655-1662. [3] Klein H. P. et al. (1992) *Mars*, 1221-1233. [4] Boynton W. V. et al. (2002) *Science*, Abstract #1073722v1. [5] McKay C. P. and Stoker C. R. (1989) *Rev. Geophys.*, 27, 189-214. [6] DiMarco A. A. et al. (1990) *Ann. Rev. Biochem.*, 59, 355-394. [7] Jarrell K. F. and Kalmokoff M. L. (1987) *Can. J. Microbiol.*, 34, 557-576. [8] Jones W. J. et al. (1983) *Arch. Microbiol.*, 136, 254-261. [9] Allen C.C. et al. (1998) *Space* 98, 469-476. [10] Boone D. R. et al. (1989) *Appl. Environ. Microbiol.*, 55, 1735-1741. [11] Xun L. et al. (1988) *Appl. Environ. Microbiol.*, 54, 2064-2068. [12] Rothe O. and Thomm M. (2000) *Extremophiles*, 4, 247-252.

**MARS PHOTOCHEMISTRY: WEAK POINTS AND SEARCH FOR SOLUTIONS.** Vladimir A. Krasnopolsky, Catholic University of America, Department of Physics, 200 Hannan Hall, Washington, D.C. 20064 (vkrasn@verizonmail.com).

Photochemical modeling is a powerful tool to study the chemical composition of a planetary atmosphere. Using densities of just two or three species near the surface of a planet, photochemistry makes it possible to calculate vertical density profiles for a few dozen species and describe chemical and physical processes that determine these profiles.

**Weaknesses of the Current Models of Mars Photochemistry:** The latest models of Mars photochemistry [1-5] were made a decade ago. There is an increasing disagreement between the recent experimental data and those models:

- 1) The standard gas-phase chemistry predicts too low abundances of CO and ozone;
- 2) All modifications in gas-phase chemistry suggested to agree the models with the observations have not been confirmed;
- 3) Recent measurements [6, 7] give even greater CO abundance than that in the modified models;
- 4) The detected H<sub>2</sub> abundance [8] is far below the model predictions;
- 5) MGS/TES mean H<sub>2</sub>O abundance [9] exceeds that used in the models;
- 6) The observed upper limit to H<sub>2</sub>O<sub>2</sub> [10] is smaller than the model predictions by an order of magnitude;
- 7) The observed low latitudinal variations of the O<sub>2</sub>(<sup>1</sup>Δ) dayglow at 1.27 μm [11] and ozone [12] disagree with the very strong variations of H<sub>2</sub>O [9] and question the basic concept of Mars photochemistry.

These facts show that the current models are inadequate, incomplete, and needs a significant updating.

**Global, Local, and General Circulation Models:** One-dimensional global-mean model is a traditional tool to solve basic photochemical problems. Eddy diffusion, which is uncertain within a factor of 3, substitutes atmospheric mixing in these models. The models reflect the global-mean values and are especially good for long-living species H<sub>2</sub>, O<sub>2</sub>, and CO on Mars.

Local models are adjusted to local conditions. The lifetimes of H<sub>2</sub>, O<sub>2</sub>, and CO are greater than the global atmospheric mixing time, therefore these species cannot be calculated by the local models. These abundances are the basic experimental constraints, and the chemistry adopted in the local models should be tested by the global models on the consistency with the measured H<sub>2</sub>, O<sub>2</sub>, and CO.

Photochemical GCMs may appear soon, and that will be a significant progress in photochemical model-

ing. However, there are two restrictions to those models. First, they do not cover atmospheric mixing at the scales, which are smaller than the model grid step. Therefore, these models either underestimate the atmospheric mixing or should adopt small-scale mixing, similar to that in the global and local models.

The second restriction is a very long run for the GCMs even with the simplest chemistry. Therefore, similar to the local models, the mean abundances of H<sub>2</sub>, O<sub>2</sub>, and CO are adopted by the photochemical GCMs, and their chemistry should be tested by the global models on the consistency with the measured H<sub>2</sub>, O<sub>2</sub>, and CO. The models considered below are global mean and without nitrogen chemistry. This is

**Table 1.** Reactions of CO<sub>2</sub>-H<sub>2</sub>O chemistry on Mars and their rate coefficients

Reaction	Rate Coefficient
1 CO <sub>2</sub> + hν → CO + O	-
2 CO <sub>2</sub> + hν → CO + O( <sup>1</sup> D)	-
3 O <sub>2</sub> + hν → O + O	-
4 O <sub>2</sub> + hν → O + O( <sup>1</sup> D)	-
5 H <sub>2</sub> O + hν → H + OH	-
6 HO <sub>2</sub> + hν → OH + O	1.3×10 <sup>-4</sup>
7 H <sub>2</sub> O <sub>2</sub> + hν → OH + OH	2.1×10 <sup>-5</sup>
8 O <sub>3</sub> + hν → O <sub>2</sub> ( <sup>1</sup> Δ) + O( <sup>1</sup> D)	1.7×10 <sup>-3</sup>
9 O( <sup>1</sup> D) + CO <sub>2</sub> → O + CO <sub>2</sub>	7.4×10 <sup>-11</sup> e <sup>120/T</sup>
10 O( <sup>1</sup> D) + H <sub>2</sub> O → OH + OH	2.2×10 <sup>-10</sup>
11 O( <sup>1</sup> D) + H <sub>2</sub> → OH + H	1.1×10 <sup>-10</sup>
12 O <sub>2</sub> ( <sup>1</sup> Δ) + CO <sub>2</sub> → O <sub>2</sub> + CO <sub>2</sub>	10 <sup>-20</sup>
13 O <sub>2</sub> ( <sup>1</sup> Δ) → O <sub>2</sub> + hν	2.24×10 <sup>-4</sup>
14 O + CO + CO <sub>2</sub> → CO <sub>2</sub> + CO <sub>2</sub>	2.2×10 <sup>-33</sup> e <sup>-1780/T</sup>
15 O + O + CO <sub>2</sub> → O <sub>2</sub> + CO <sub>2</sub>	1.2×10 <sup>-32</sup> (300/T) <sup>2</sup>
16 O + O <sub>2</sub> + CO <sub>2</sub> → O <sub>3</sub> + CO <sub>2</sub>	1.3×10 <sup>-33</sup> (300/T) <sup>2.4</sup>
17 H + O <sub>2</sub> + CO <sub>2</sub> → HO <sub>2</sub> + CO <sub>2</sub>	1.7×10 <sup>-31</sup> (300/T) <sup>1.6</sup>
18 O + HO <sub>2</sub> → OH + O <sub>2</sub>	3×10 <sup>-11</sup> e <sup>200/T</sup>
19 O + OH → O <sub>2</sub> + H	2.2×10 <sup>-11</sup> e <sup>120/T</sup>
20 CO + OH → CO <sub>2</sub> + H	1.5×10 <sup>-13</sup>
21 H + O <sub>3</sub> → OH + O <sub>2</sub>	1.4×10 <sup>-10</sup> e <sup>-470/T</sup>
22 H + HO <sub>2</sub> → OH + OH	7.3×10 <sup>-11</sup>
23 H + HO <sub>2</sub> → H <sub>2</sub> + O <sub>2</sub>	1.3×10 <sup>-11</sup> (T/300) <sup>0.5</sup> e <sup>-230/T</sup>
24 H + HO <sub>2</sub> → H <sub>2</sub> O + O	1.6×10 <sup>-12</sup>
25 OH + HO <sub>2</sub> → H <sub>2</sub> O + O <sub>2</sub>	4.8×10 <sup>-11</sup> e <sup>250/T</sup>
26 HO <sub>2</sub> + HO <sub>2</sub> → H <sub>2</sub> O <sub>2</sub> + O <sub>2</sub>	3.2×10 <sup>-13</sup> e <sup>580/T</sup>
27 OH + H <sub>2</sub> O <sub>2</sub> → HO <sub>2</sub> + H <sub>2</sub> O	2.9×10 <sup>-13</sup> e <sup>-160/T</sup>
28 OH + H <sub>2</sub> → H <sub>2</sub> O + H	3.3×10 <sup>-13</sup> (T/300) <sup>2.7</sup> e <sup>-1150/T</sup>
29 O + O <sub>3</sub> → O <sub>2</sub> + O <sub>2</sub>	8×10 <sup>-12</sup> e <sup>-2060/T</sup>
30 OH + O <sub>3</sub> → HO <sub>2</sub> + O <sub>2</sub>	1.5×10 <sup>-12</sup> e <sup>-880/T</sup>

Photolysis rates and  $k_{13}$  are in s<sup>-1</sup>, second and third order reaction rate coefficients are in cm<sup>3</sup> s<sup>-1</sup> and cm<sup>6</sup> s<sup>-1</sup>, respectively. Photolysis rates for all species except CO<sub>2</sub>, O<sub>2</sub>, and H<sub>2</sub>O refer to the lower atmosphere, are calculated for λ > 200 nm and scaled to half values at 1.517 AU.

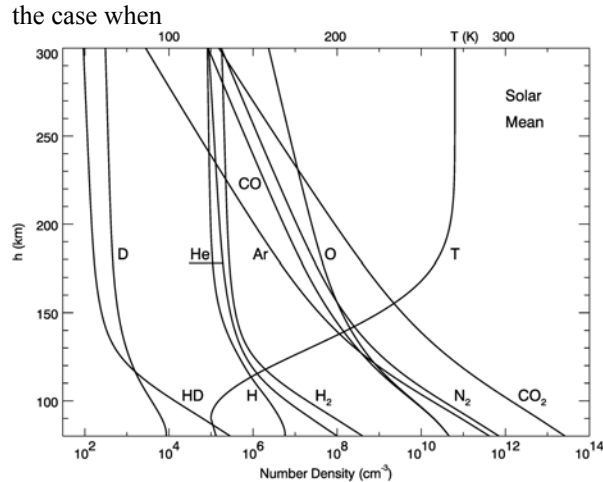


Figure 1. Model of Mars upper atmosphere at medium solar activity [13].

the production of N in the lower thermosphere exceeds the production of NO [1].

**Mars Model Upper Atmosphere and Ionosphere:** A detailed model for the upper atmosphere and ionosphere of Mars was recently developed [13]. This model includes 11 neutral (Figure 1) and 18 ion species (Figure 2), 32 photon and photoelectron dissociation, ionization, and dissociative ionization processes, and 54 reactions. Both thermal and nonthermal escape processes were considered at the upper boundary of 300 km. Therefore, our current model will cover the altitudes below 80 km, and we will apply the fluxes of H and H<sub>2</sub> at medium solar activity from that model at our upper boundary of 80 km.

**Boundary Conditions, Input Data, and Chemical Reactions:** The escape of H and H<sub>2</sub> should be perfectly balanced by the escape and/or loss of oxygen for the surface oxidation in the steady-state models of Mars photochemistry. The models diverge if this rule is broken. It does not matter for the model if oxygen escapes or is lost at the surface, and we assume the former.

The hydrogen escape flux and the H and H<sub>2</sub> velocities at the upper boundary were the input data in the previous models [3, 4]. A flux to velocity ratio is density, and we assign the H and H<sub>2</sub> fluxes and the H<sub>2</sub> density from [13] at 80 km in our model. Other boundary conditions reflect the CO<sub>2</sub> dissociation of  $1.4 \times 10^{11}$  cm<sup>-2</sup> s<sup>-1</sup> above 80 km and the O<sub>2</sub> dissociation velocity of 0.16 cm s<sup>-1</sup> at 80 km. Conditions at the lower boundary correspond to the chemically passive surface.

The MGS/TES data on the day- and nighttime temperature structure of Mars atmosphere at  $L_S = 0, 90, 180,$  and  $270^\circ$  were properly averaged to get a mean

temperature profile. The global-mean water abundance of 15 precipitable  $\mu\text{m}$  from the MGS/TES observations [9] results in the H<sub>2</sub>O mixing ratio of 260 ppm up to a condensation level at 18 km.

Table 1 presents a standard set of gas-phase reactions for the CO<sub>2</sub>-H<sub>2</sub>O chemistry on Mars. The reaction rate coefficients are taken mostly from the JPL compilations [14, 15] and some later publications. The photolysis rates have been calculated using the appropriate cross sections from the JPL compilations as well.

**Table 2.** Some Results of Modeling

Value	Obs	M1	M2	M3	M4
O <sub>2</sub> ( $\times 10^{-3}$ )	1.2	1.4	1.5	1.3	2.4
CO (0 km, $\times 10^{-4}$ )	8	0.8	1.0	0.9	2.4
CO (40 km, $\times 10^{-4}$ )	-	1.5	1.1	1.2	2.6
CO (80 km, $\times 10^{-4}$ )	-	66	7.6	7.7	9.1
O <sub>3</sub> ( $\mu\text{m-atm}$ )	1.5-3	0.63	0.66	0.52	2.6
$4\pi I_{1.27\ \mu\text{m}}$ (MR)	$\approx 4$	1.14	1.26	1.04	3.8
H <sub>2</sub> O <sub>2</sub> (ppb)	<4	20.2	21.3	23.8	3.1

See text for explanation.

**Results:** Some results of modeling are shown in Table 2. The second column (Obs) gives the observed values.  $4\pi I_{1.27\ \mu\text{m}}$  (MR) is the O<sub>2</sub>(<sup>1</sup> $\Delta$ ) 1.27  $\mu\text{m}$  dayglow brightness in megarayleighs. Models M1-M3 are for pure gas-phase chemistry with different eddy diffusion coefficient K. K is equal to  $10^6$  cm<sup>2</sup> s<sup>-1</sup> for M1, and the abundance of CO near the surface, O<sub>3</sub>, and the O<sub>2</sub> dayglow are much below the observed values, while H<sub>2</sub>O<sub>2</sub> is far above the upper limit. The CO mixing ratio is greater at 40 km than that near the surface by a factor of 2. If CO were equal to the observed value near the surface, that would occur for  $K = 10^5$  cm<sup>2</sup> s<sup>-1</sup>. CO is very abundant at 80 km because of the low eddy diffusion.

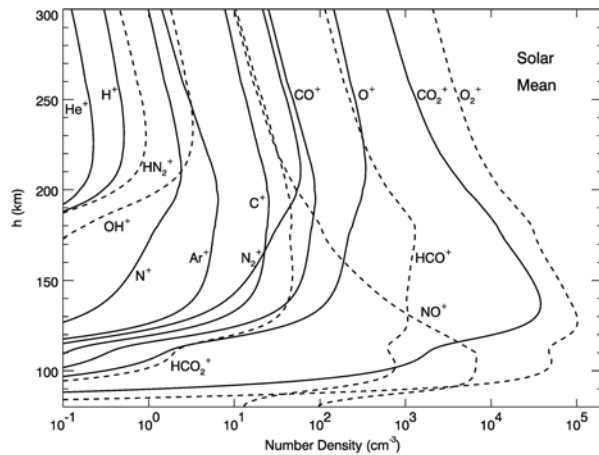


Figure 2. Model of Mars ionosphere at medium solar activity [13].

M2 is for  $K = 10^7 \text{ cm}^2 \text{ s}^{-1}$ , and it is similar to M1 in many aspects. The difference between M1 and M2 in  $\text{H}_2\text{O}_2$  is small. This difference was a factor of 2 in the local model [10], maybe, because the  $\text{H}_2$ ,  $\text{O}_2$ , and  $\text{CO}$  abundances were fixed in that model. M3 is a model for  $K$  increasing from  $10^5$  near the surface to  $10^7$  at 40 km and higher [3]. This profile of  $K$  is preferable.

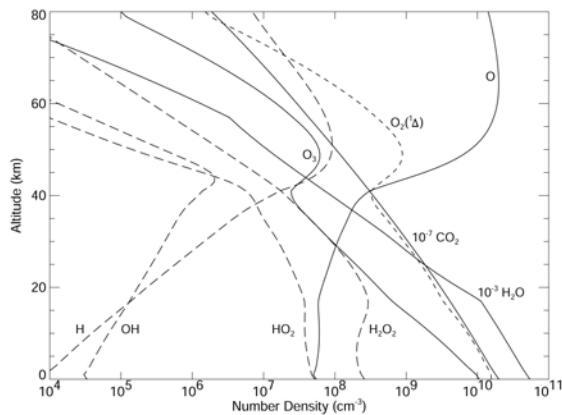


Figure 3. Model for Mars photochemistry (M4) with a heterogeneous sink of peroxide on ice and ice-covered aerosol particles.

All pure gas-phase chemistry models significantly disagree with the observations. However, laboratory data and studies of chemistry of the Earth's atmosphere show that ice particles are very effective in scavenging of all forms of odd hydrogen. Their sticking coefficients may be as high as 1, 0.2, 0.5, and 0.03 for OH,  $\text{HO}_2$ ,  $\text{H}_2\text{O}_2$ , and H, respectively [14, 15].

According to the MGS/TES observations [16], the mean optical depth of ice aerosol is  $\approx 0.05$  at  $12 \mu\text{m}$  and  $\approx 0.1$  in the visible at 2 p.m., i.e., near the diurnal minimum. Ice may cover some dust particles, and we

assume that the altitude distribution of ice and ice-covered particles is similar to that of dust, which is taken from [17]. Model M4 is similar to M3 but includes a heterogeneous sink of  $\text{H}_2\text{O}_2$  on ice with a probability of 0.025. The  $\text{O}_3$  and  $\text{H}_2\text{O}_2$  abundances and the  $\text{O}_2(^1\Delta)$  dayglow in M4 agree with the observations (Table 2), while  $\text{CO}$  is between the measured abundance and that from the gas-phase models. It is clear that the inclusion of heterogeneous chemistry provides a distinct possibility to fit all observational constraints. The calculated vertical density profiles for model M4 are shown in Figure 3.

Our simulations show that a major effect of heterogeneous chemistry is produced by the ice aerosol above  $\approx 5 \text{ km}$ . This aerosol opacity may be proportional to the  $\text{H}_2\text{O}$  abundance. Then both production and loss of odd hydrogen are proportional to the water vapor abundance. This helps to explain the low latitudinal variations of the  $\text{O}_2(^1\Delta)$  dayglow and ozone, in spite of the variations of water vapor by more than an order of magnitude.

**Conclusions:** (1) There are significant contradictions between the latest photochemical models and the observations.

(2) All these contradictions may be removed by the inclusion of heterogeneous chemistry.

(3) Heterogeneous chemistry is very effective in the Earth's atmosphere. It should exist in the Martian atmosphere, and Mars photochemical models are inadequate without heterogeneous chemistry.

**Acknowledgements:** I am grateful to Mike Smith who kindly offered the MGS/TES temperature data for this work. This work was supported by the Mars Data Analysis Program via grant NAG5-10492.

**References:** [1] Krasnopolsky V. A. (1993) *Icarus* 101, 313-332. [2] Atreya S. K. and Gu Z. G. (1994) *JGR* 99, 13133-13145. [3] Nair H. et al. (1994) *Icarus* 111, 124-150. [4] Krasnopolsky V. A. (1995) *JGR* 100, 3263-3276. [5] Clancy R. T. and Nair H. (1996) *JGR* 101, 12785-12790. [6] Clancy R. T. et al. (1996) *Icarus* 122, 36-62. [7] Krasnopolsky V. A. (2003) *JGR* 108, E2, 5010. [8] Krasnopolsky V. A. and Feldman P. D. (2001) *Science* 294, 914-917. [9] Smith M. D. (2002) *JGR* 107, E11, 5115. [10] Encrenaz Th. et al. (2002) *A&A* 396, 1037-1044. [11] Krasnopolsky V. A. (2003) *Icarus* (MS 108520). [12] Clancy R. T. et al. (1999) *Icarus* 138, 49-63. [13] Krasnopolsky V. A. (2002) *JGR* 107, E12, 10.29/2001JE001809. [14] DeMore W. B. et al. (1997) *JPL Pub.* 97-4. [15] Sander S. P. et al. (2000) *JPL Pub.* 00-3. [16] Smith M. D. et al. (2001) *GRL* 28, 4263-4266. [17] Korablev O. I. Et al. (1993) *Icarus* 102, 76-87.

**SPECTROSCOPY OF MARS ATMOSPHERE FROM ORBITING AND GROUND-BASED OBSERVATORIES: RECENT RESULTS AND IMPLICATIONS FOR EVOLUTION.** V. A. Krasnopolsky, Catholic University of America, Department of Physics, 200 Hannan Hall, Washington, D.C. 20064 (vkrasn@verizonmail.com).

**Introduction:** The basic data on the chemical composition of Mars' atmosphere were obtained by the Viking mass spectrometers a quarter of century ago. Spacecraft missions to Mars in the last decade have not been aimed to this field, and the current progress is related to high-resolution spectroscopy from orbiting and ground-based observatories.

**HDO:** Deuterated water was detected [1] using CFHT/FTS with resolving power  $\nu/\delta\nu = 9 \times 10^4$  (Fig. 1). Very low humidity (0.5 pr. mm) above Mauna Kea and a significant (by a factor of 6) enrichment of water in D on Mars facilitated the detection.

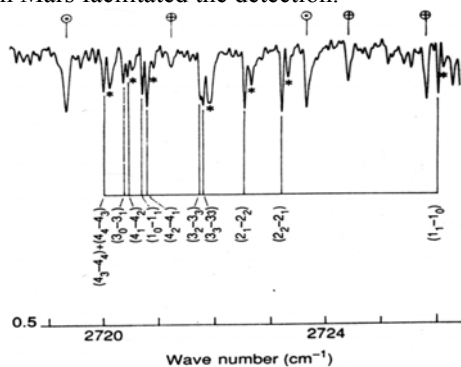


Fig. 1. HDO lines in the CFHT/FTS spectrum [1]. Telluric HDO (\*), CH<sub>4</sub> (+), and solar (o) lines are also seen.

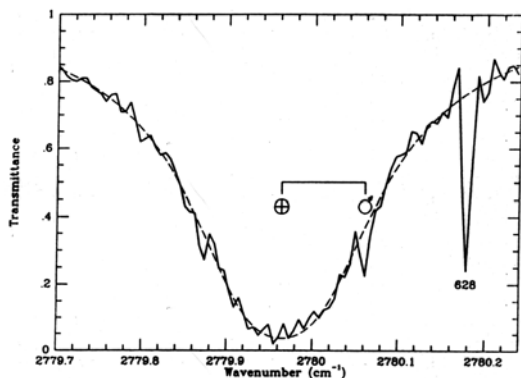


Fig. 2. One of ten HDO lines in the KPNO/FTS spectrum [2]. Telluric line is much stronger and broader than the Martian line. Dashed curve is a model fit to the telluric line, 628 is the CO<sup>18</sup>O line.

Ten HDO lines in the KPNO/FTS spectrum [2] were also used to measure the D/H ratio in water on Mars (Fig. 2). Despite the better spectral resolution ( $\nu/\delta\nu = 2.7 \times 10^5$ ), the HDO lines were less prominent

because of the much higher humidity (14 pr. mm) above Kitt Peak. Both observations agree and result in  $D/H = 5.5 \pm 1$  times the terrestrial value in the Martian water. The KAO observation of HDO [3] is still under revision.

**Atomic Deuterium:** The D Lyman- $\alpha$  line at 1215.34 Å is shifted from the H line by 0.33 Å and very much weaker than the H line. The Martian lines are Doppler-shifted by 0.06 Å maximum relative to the telluric lines. All four lines were detected and resolved (Fig. 3) in the HST/GHRS observation [4]. The instrument resolving power was  $1.6 \times 10^4$ . The observed D-line intensity of  $23 \pm 6$  R at solar minimum corresponds to  $[D] = 450 \pm 120 \text{ cm}^{-3}$  at 250 km.

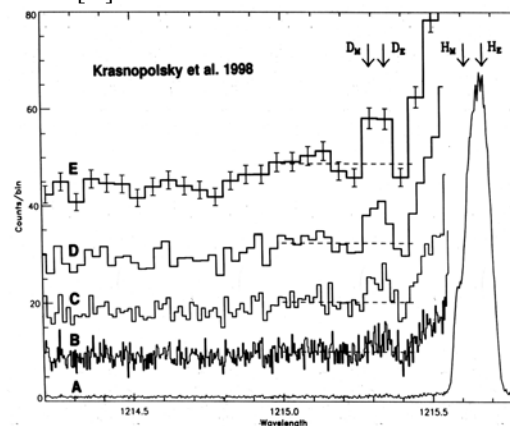


Fig. 3. Telluric and Martian (subscripts E and M, respectively) Lyman- $\alpha$  lines of H and D in the HST/GHRS spectrum [4] at five levels of binning.

**Molecular Hydrogen:** Vibrational and rotational transitions are strongly forbidden in H<sub>2</sub>. Despite the low dissociation energy of 4.48 eV, dissociation to the ground-state H atoms is parity-forbidden, and H<sub>2</sub> absorbs photons only below 1108 Å where the solar radiation is weak. Therefore, detection of H<sub>2</sub> presents a difficult problem. Fortunately, three absorption lines of H<sub>2</sub> coincide with the strong solar Lyman  $\beta$ ,  $\gamma$ , and C II lines and originate a few comparatively strong emission lines. These lines were observable (Fig. 4) in the FUSE spectrum of Mars [5]. The observation resulted in a column H<sub>2</sub> abundance of  $(1.71 \pm 0.13) \times 10^{13} \text{ cm}^{-2}$  above 140 km. The FUSE spectrum of Mars [6] covered a range of 904 to 1186 Å with spectral resolution of 0.2 Å. The spectrum is of high quality and provides a detection limit of  $\approx 0.1$  R. Many Martian lines and

ion species  $N^+$ ,  $C^+$ , and  $Ar^+$  have been observed for the first time in that spectrum. For example, two  $Ar^+$  and eight H lines of the Lyman series are among other lines in Fig. 5.

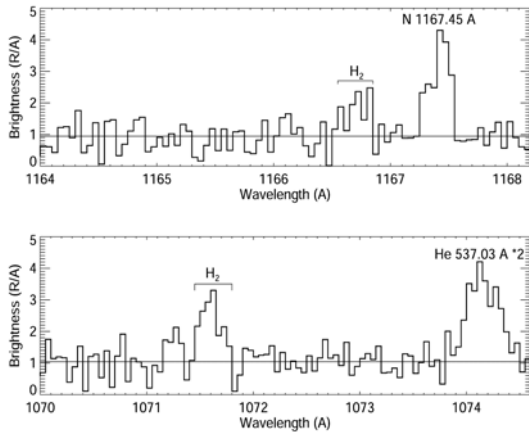


Fig. 4. Fragments of the FUSE spectrum [5] near the  $H_2$  lines at 1166.76 and 1071.62 Å.

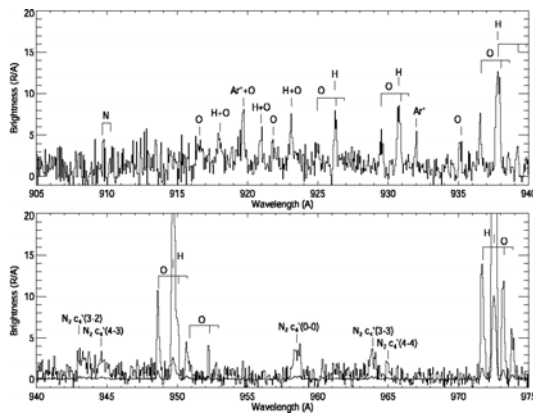


Fig. 5. A part of the FUSE spectrum [6].

### Interpretation of the Observed HDO, D, and $H_2$ :

Detailed photochemical modeling of Mars' upper atmosphere and ionosphere [7] to fit the observed D and  $H_2$  abundances results in the HD and  $H_2$  mixing ratios of  $11 \pm 4$  ppb and  $15 \pm 5$  ppm, respectively. Then

$$R = \frac{HD/H_2}{HDO/H_2O} = 0.4.$$

This agrees with the fractionation of D in chemical reactions ( $R \approx 1.6$  [8]), photolysis of  $H_2O$  ( $R \approx 0.4$  [9]), and the HDO depletion above the condensation level ( $R \approx 0.7$  [10, 11]). Finally,  $R = 1.6 \times 0.4 \times 0.7 \approx 0.4$ , and the controversial problem of deuterium fractionation in Mars' atmosphere looks solved. The observed HDO, D, and  $H_2$  require the escape fractionation factor

$$f = \frac{\phi_D / \phi_H}{D/H} = 0.105$$

averaged over the solar cycle.

**Implications for Evolution of Water:** Combining this fractionation factor with the water abundance in the polar caps (a global-mean layer of  $\approx 14$  m deep [12-14]) and the  $D/H = 1.9$  [15] at the end of the intense impact erosion of the atmosphere 3.8 Ga ago, this results in a loss of an ocean of water of 30 m deep for this period.

Hydrodynamic escape of  $H_2$  released in the reaction  $Fe + H_2O \rightarrow FeO + H_2$  could be effective for 0.1-0.3 Ga after Mars' formation. Using a fractionation factor of 0.8 for this escape [16] and a standard assumption of the terrestrial value for the initial  $D/H$  on Mars, the total loss of water by hydrodynamic escape was 1.2 km. Therefore Mars could initially be even more rich in water than Earth.

**Helium:** Helium was detected on Mars using the EUVE/LW spectrometer [17] that had a capability to detect the He 584 Å line against the strong geocoronal emission of this line. The observed line intensity of  $57 \pm 15$  R corresponds to the He mixing ratio of  $4 \pm 2$  ppm [18]. Helium is lost from Mars mostly by electron impact ionization above the ionopause and sweeping out of the ions by the solar wind. The total loss is equal to  $7 \times 10^{23} \text{ s}^{-1}$  and agrees with the Phobos measurements [19]. A source of He on the terrestrial planets is the radioactive decay in the uranium and thorium chains with subsequent outgassing. It is similar to the outgassing of  $^{40}Ar$  formed by the decay of potassium. A coupled model for the outgassing of He and  $^{40}Ar$  showed that (1) outgassing from Mars is weaker than that from Earth by an order of magnitude, (2) outgassing of He from Mars covers a third of its loss. An additional source of He is required, and that should be a capture of the solar-wind  $\alpha$ -particles with an efficiency of  $\approx 0.3$ . This is the first and probably the only case when a capture of the solar wind is critical to a

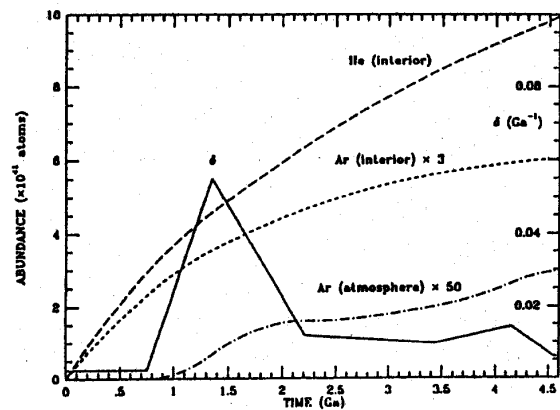


Fig. 6. Model [18] for evolution of  $^4He$  and  $^{40}Ar$  in Mars interior and atmosphere for outgassing coefficient  $\delta$  proportional to Mars volcanism rate from [20].

balance of atmospheric species. Later calculations of the solar wind capture efficiency by Mars [21] confirmed our conclusion and also gave the value of 0.3 for  $\alpha$ -particles.

**Ozone and O<sub>2</sub> 1.27  $\mu$ m Dayglow:** Ozone is a tracer of Mars photochemistry, and a latitudinal-versus-season mapping of O<sub>3</sub>, similar to that done for H<sub>2</sub>O by the Viking/MAWD [22] and MGS/TES [23], is the objective of ozone observations. Three tools are currently used. Infrared heterodyne spectroscopy at 9.6  $\mu$ m [24] gave the first data on the O<sub>3</sub> distribution at low and middle latitudes (Fig. 6). The instrument resolving power was 10<sup>6</sup> in the published observations. Another tool is the HST/FOS UV spectroscopy near Mars' limb [25, 26] (Fig. 7).

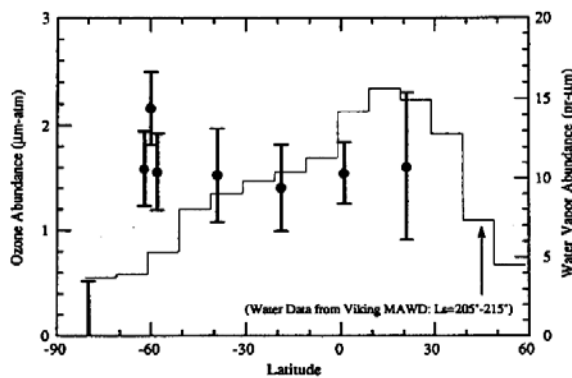


Fig. 6. Latitudinal distribution of ozone at  $L_S = 208^\circ$  [24].

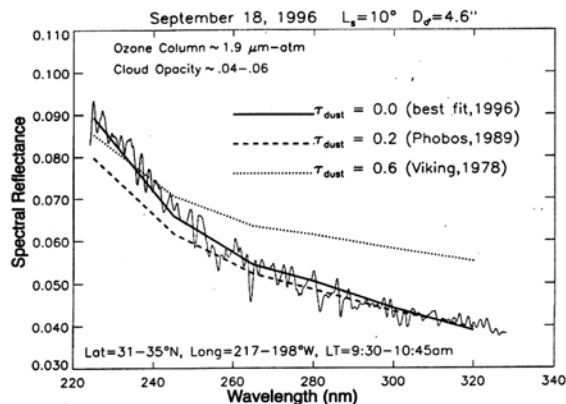


Fig. 7. Three-parameter fitting to the observed HST/FOS spectrum [26] near Mars' limb. The parameters are ozone column and cloud and dust opacities.

Ozone above 20 km is the most sensitive to seasonal variations of photochemistry at low and middle latitudes [27]. It was suggested in [28] to observe the O<sub>2</sub> 1.27  $\mu$ m dayglow using IRTF/CSHELL to map high-altitude ozone. This dayglow is excited by photolysis of O<sub>3</sub> and quenched by CO<sub>2</sub> below 15-20

km. Therefore it is the best tracer of Mars' photochemistry. The IRTF/CSHELL resolving power is  $4 \times 10^4$ , that is, 7.5 km/s, and the observations are feasible for the geocentric velocity  $\geq 10$  km/s. The dayglow spectrum observed at  $L_S = 112^\circ$  [29] is shown in Fig. 8. The retrieved dayglow intensities are corrected for airmass, surface reflectivity, and the instrument point spread function. (All these corrections are of a factor of  $\approx 1.5$  and cannot be ignored.) Latitudinal dependences of the dayglow intensity for three seasons [30] are shown in Fig. 9. The dayglow maps have a spatial resolution of 0.1-0.2 Mars radii. Analysis of the dayglow observation along one instrument slit was recently reported in [31].

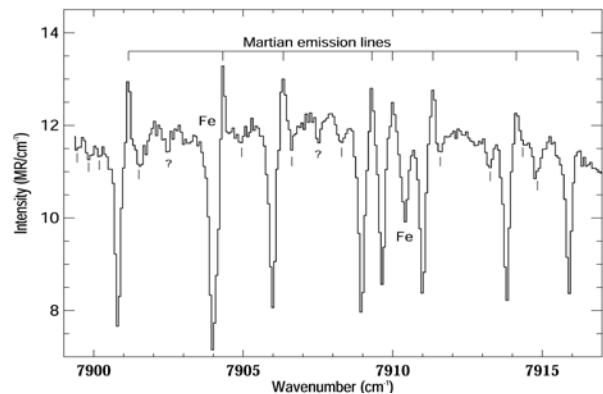


Fig. 8. One of 550 spectra of Mars observed with IRTF/CSHELL at  $L_S = 112^\circ$  [29]. The main features are the telluric absorption and Martian Doppler-shifted O<sub>2</sub> emission lines and two solar Fe lines.

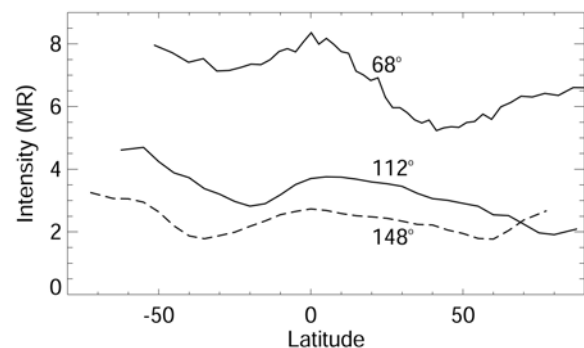


Fig. 9. Latitudinal dependences of the O<sub>2</sub> 1.27  $\mu$ m dayglow at three seasons [30].

**CO Mixing Ratio:** Low resolution spectroscopy from the Phobos orbiter [32] revealed a significant (by a factor of 5-8) decrease in the CO mixing ratio above the great Martian volcanoes. This decrease contradicts to gas-phase chemistry, which predicts a constant CO mixing ratio over Mars' globe and up to  $\approx 60$  km. Attempts to check this result by using ground-based observations were made in [33, 34] using the CO lines at

1.3 mm and 2.3  $\mu\text{m}$ , respectively. However, their fields of view were large, 1 and 0.5 Mars radii, respectively. No significant variations have been observed. A CO line shape at 1.3 mm [35] also favors a CO mixing ratio, which is constant with height.

The CO mixing ratio on Mars was mapped at  $L_S = 112^\circ$  [36] by observing both CO and CO<sub>2</sub> lines at 1.57  $\mu\text{m}$  (Fig. 10) using IRTF/CSHELL. The measured CO mixing ratio does not vary from place to place, with local time and elevation (in the range of -6 to 3 km) while the variation with latitude is substantial (Fig. 11). It is explained by the intense condensation of CO<sub>2</sub> at the South (winter) polar cap and the low meridional circulation in the southern winter [37]. An alternative explanation is the photochemical accumulation of CO due to freezing out of H<sub>2</sub>O. However, it is compensated by the low insolation in winter polar regions (polar night) and much smaller than the observed effect. The increase in the CO mixing ratio to the South and its extent to low latitudes is determined by atmospheric dynamics and should be simulated by GCMs.

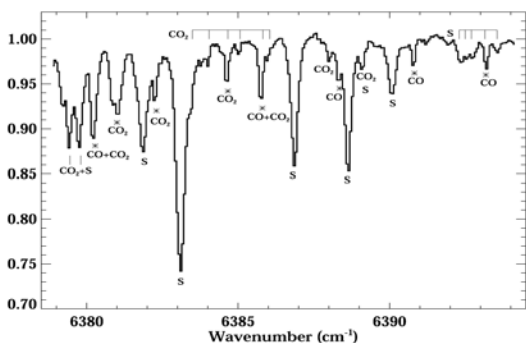


Fig. 10. One of 520 IRTF/CSHELL spectra at 1.57  $\mu\text{m}$  [36]. The spectrum consists of the CO, CO<sub>2</sub>, and solar (S) lines.

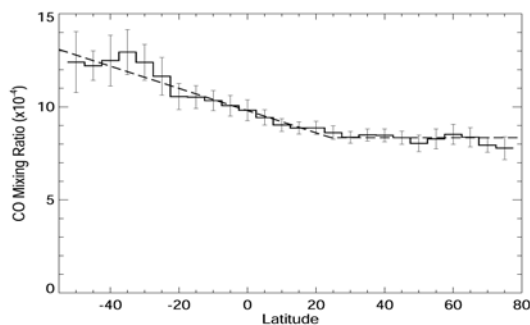


Fig. 11. Latitudinal dependence of the CO mixing ratio at  $L_S = 112^\circ$  [36].

**Upper Limits:** The most restrictive upper limit was obtained recently for H<sub>2</sub>O<sub>2</sub> using TEXES at 8  $\mu\text{m}$ . The instrument resolving power was  $7 \times 10^4$ , and the limit is 4 ppb [38], that is, below the model predictions

by an order of magnitude. Upper limits of 3 ppb to HCl and H<sub>2</sub>CO were extracted from the KPNO/FTS spectrum at 3.7  $\mu\text{m}$  [2]. The limit to HCl shows that chlorine chemistry is negligible on Mars.

Here I do not consider very fruitful and extensive MGS/TES observations of temperature profiles, H<sub>2</sub>O, dust and ice aerosol, and ground-based observations of water vapor, H<sub>2</sub>O and CO<sub>2</sub> ice, and dust, and microwave observations.

**Acknowledgment:** This work was supported by NASA Mars Data Analysis Program (grant NAG5-10575).

**References:** [1] Owen T. et al. (1988) *Science* 240, 1767-1771. [2] Krasnopolsky V. A. et al. (1997) *JGR* 102, 6525-6534. [3] Bjoraker G. L. et al. (1989) *BAAS* 21, 991. [4] Krasnopolsky V. A. et al. (1998) *Science* 280, 1576-1580. [5] Krasnopolsky V. A. and Feldman P. D. (2001) *Science* 294, 1914-1917. [6] Krasnopolsky V. A. and Feldman P. D. (2002) *Icarus* 160, 86-94. [7] Krasnopolsky V. A. (2002) *JGR* 107, E12, 10.1029/2001JE001809. [8] Yung Y. L. et al. (1988) *Icarus* 76, 146-159. [9] Cheng B. M. et al. (1999) *GRL* 26, 3657-3660. [10] Fouchet T. and Lellouch E. (2000) *Icarus* 144, 114-123. [11] Krasnopolsky V. A. (2000) *Icarus* 148, 597-602. [12] Jakosky B. M. (1990) *JGR* 95, 1475-1480. [13] Smith D. E. et al. (1999) *Science* 284, 1495-1503. [14] Head J. W. (2001) *JGR* 106, 10075-10080. [15] Leshin L. A. (2000) *GRL* 27, 2017-2020. [16] Zahnle K. et al. (1990) *Icarus* 84, 502-527. [17] Krasnopolsky V. A. et al. (1994) *Icarus* 109, 337-351. [18] Krasnopolsky V. A. and Gladstone G. R. (1996) *JGR* 101, 15765-15772. [19] Barabash S. et al. (1995) *JGR* 100, 21307-213016. [20] Greeley R. (1987) *Science* 236, 1653-1654. [21] Brecht S. H. (1997) *JGR* 102, 11287-11294. [22] Jakosky B. M. and Farmer C. B. (1982) *JGR* 87, 2999-3019. [23] Smith M. D. (2002) *JGR* 107, E11, 10.1029/2001JE001522. [24] Espenak F. et al. (1991) *Icarus* 92, 252-262. [25] Clancy R. T. et al. (1996) *JGR* 101, 12777-12783. [26] Clancy R. T. et al. (1999) *Icarus* 138, 49-63. [27] Clancy R. T. and Nair H. (1996) *JGR* 101, 12785-12790. [28] Krasnopolsky V. A. (1997) *JGR* 102, 13313-13320. [29] Krasnopolsky V. A. and Bjoraker G. L. (2000) *JGR* 105, 20179-20188. [30] Krasnopolsky V. A. (2003) *Icarus* (submitted). [31] Novak R. et al. (2002) *Icarus* 158, 14-23. [32] Rosenqvist J. et al. (1992) *Icarus* 98, 254-270. [33] Lellouch E. et al. (1991) *PSS* 39, 219-224. [34] Billebaud F. et al. (1998) *AA* 333, 1092-1099. [35] Encrenaz T. et al. (1991) *Ann. Geo.* 9, 797-803. [36] Krasnopolsky V. A. (2003) *JGR* 108, E2, 10.1029/2002JE001926. [37] Haberle R. M. et al. (1993) *JGR* 98, 3093-3123. [38] Encrenaz T. et al. (2002) *AA* 396, 1037-1044.

**NORTH-SOUTH SLOPE ASYMMETRY ON MARS.** *M. A. Kreslavsky*<sup>1,2</sup> and *J. W. Head*<sup>1</sup>, <sup>1</sup>Department of Geological Sciences, Brown University, Providence, RI, 02912-1846, USA, misha@mare.geo.brown.edu <sup>2</sup>Astronomical Institute, Kharkov National University, Kharkov, Ukraine.

**Abstract:** A map of north-south subkilometer-scale slope asymmetry on Mars obtained from statistical analysis of along-track MOLA topographic profiles reveals well-defined latitudinal bands of north-south slope asymmetry at 40-50° in both hemispheres. In these bands the equator-facing slopes are systematically steeper than pole-facing slopes. This asymmetry is especially pronounced for the steepest (>20°) slopes: equator-facing ones are three times more frequent. We interpret these bands to be related to insolation asymmetry. Particularly, we suggest that transient melting of ground ice at pole-facing slopes occurred during the periods of very high obliquity (~45°) in the past and favored downslope mass movement and elimination of steep pole-facing slopes. The map reveals also several other areas of pronounced north-south slope asymmetry. In these areas the asymmetry takes place for gentle slopes. It is interpreted to be caused by prevailing wind direction during formation and modification of surficial deposits.

**Introduction:** The Mars Orbiter Laser Altimeter (MOLA) onboard the Mars Global Surveyor (MGS) spacecraft produced a large homogeneous data set of precise elevation measurements along MGS tracks [e.g., 1] with uniform along-track spacing of 0.3 km. Except for narrow zones at very high latitudes, the gaps between the tracks are often wider than the along-track spacing.

Anisotropy of local slopes reflects the properties of topography-shaping processes. For example, asymmetry of opposite slopes is typical for eolian features. North-south slope asymmetry is also an important indicator of processes related to insolation and water mobility. For example, asymmetric troughs in the polar cap deposits have been interpreted to be due to insolation-related sublimation (producing steep equator-facing slopes) and deposition (producing shallow pole-facing slopes) [e.g., 2]. In this study we used the MOLA data set to map and analyze slope asymmetry on Mars.

**Data processing:** The direction of all MOLA tracks is close to meridional except in high-latitude regions. The deflection from the meridian is about 5° in a wide equatorial zone. Poleward from 60° latitude, the deflection slowly, then more rapidly increases, and reaches 17° at 80° latitude. Thus, sampling of the Mars surface with MOLA is strongly anisotropic. Track-to-track systematic errors in a wide equatorial zone are much greater than the noise of along-track measure-

ments even after cross-over analysis [3]. This means that kilometer-scale slopes derived from the gridded topographic map are affected by strongly anisotropic errors, and the data set does not allow complete study of the anisotropy of kilometer-scale slopes. The along-track slopes, however, are free of these errors, and the MOLA data can be used to study the north-south asymmetry of the slopes at kilometer- and hectometer-scale baselines.

The data processing technique we used was similar to that applied in [4, 5]. For each pair of consecutive MOLA shots, we calculated the differential slope, and noted the slope direction information (a positive sign was used for the south-facing slopes, and negative was used for north-facing slopes). The differential slope  $s$  was defined (Fig. 1, left) through slope  $\alpha$  at 0.3 km baseline (the shot-to-shot distance) and slope  $\beta$  at 0.9 km baseline as:  $\tan s = \tan \alpha - \tan \beta$ . The use of the differential slope instead of the ordinary slope was necessary to eliminate the influence of regional topography on slope statistics. The present definition of the differential slope is slightly different from that used in [4] and permits the use of the shortest possible baseline length of 0.3 km.

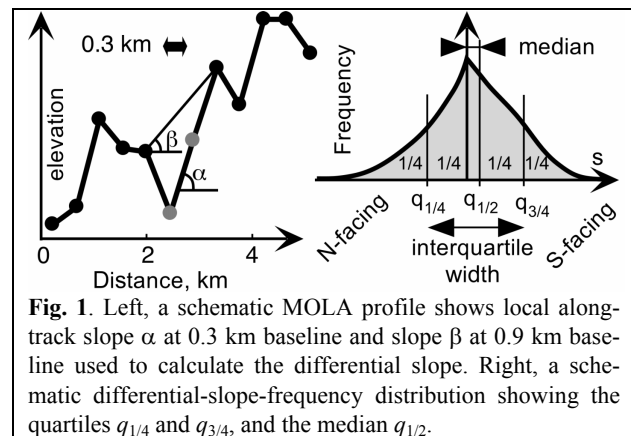


**Fig. 1.** Left, a schematic MOLA profile shows local along-track slope  $\alpha$  at 0.3 km baseline and slope  $\beta$  at 0.9 km baseline used to calculate the differential slope. Right, a schematic differential-slope-frequency distribution showing the quartiles  $q_{1/4}$  and  $q_{3/4}$ , and the median  $q_{1/2}$ .

All calculated slopes were binned into map cells in several map projections; for each cell we calculated the median slope and the quartiles  $q_{1/4}$  and  $q_{3/4}$  and the median  $q_{1/2}$  of the slope-frequency distribution (Fig. 1, right).

The difference between the quartiles  $r = q_{3/4} - q_{1/4}$  characterizes the width of the slope-frequency distribution, and serves as a measure of roughness. It is very similar to the median absolute value of the differential slope used in [4] as a measure of roughness. Fig. 2

shows the roughness map in a simple cylindrical projection obtained in this way; brighter shades denote rougher surfaces. Major geomorphic features are clearly distinguishable in the map; the latitudinal trend of roughness (smoother terrains at high latitudes) is pronounced even more clearly than in [4, Fig. 12], because the baseline used here is twice shorter. See [4] for further discussion of the roughness maps.

The median signed slope  $q_{1/2}$  can be used to quantify the deviation of the slope-frequency distribution from symmetric. The mean differential slope is almost always equal to zero. Nonzero median slope means a different balance of steep and gentle slopes for north- and south-facing surfaces. If the median slope is positive, this means that the area covered by south-facing slopes is greater than the area covered by north-facing slopes; in turn, since the mean slope is zero, this means that the north-facing slopes are generally steeper than south-facing slopes. Analogously, negative median slope means that south-facing slopes are steeper.

To eliminate roughness and characterize solely the distribution shape we normalized the median by the quartile difference and calculate the asymmetry parameter  $a = q_{1/2} / r$ . The map of this parameter is shown in Fig. 3; brighter shades denote positive  $a$ , that is that north-facing slopes are steeper, and darker shades denote that south-facing slopes are steeper.

**Regions of slope asymmetry:** The map of slope asymmetry (Fig. 3) shows clearly that most of the surface does not have any north-south slope asymmetry. Several distinctive areas, however, clearly show slope asymmetry. We repeated our calculations for 2 and 4 times longer baselines (0.6 km and 1.2 km) and obtained a spatial asymmetry distribution very similar to that shown in Fig. 3, but characteristic values of the asymmetry parameter  $|a|$  were systematically lower than for a 0.3 km baseline. For even longer baselines, the calculated parameter  $a$  reflects mostly steep regional slopes, like major graben, channel walls, crater walls, etc.

**Latitudinal Anomalous Bands.** One of the most prominent features of the map is a pair of narrow latitudinal anomalous bands at 40 - 50° in both hemispheres. The signs of the median slope in both hemispheres are opposite indicating that equator-facing slopes are steeper in these zones. The intensity of asymmetry varies along the bands. The characteristic values of the asymmetry parameter  $a$  in prominent parts of the bands is  $|a| \approx 0.8\%$ .

The low-slope ( $<1-2^\circ$ ) portion of the frequency distribution of the differential slopes for the anomalous bands is symmetrical, while the asymmetry is observed for steeper slopes (Fig. 4). To study the role of steep

slopes in the anomalous bands, we calculated the total number of steeply inclined MOLA profile segments in narrow latitudinal zones within typical southern heavily cratered highlands (Fig. 5). The number of equator-facing slopes steeper than  $20^\circ$  around  $45^\circ\text{S}$  latitude is a factor of three greater than the number of similar pole-facing slopes. The sharp decrease in the number of steep slopes from low to high latitudes occurs earlier for the pole-facing slopes and later for the equator-facing slopes. (Fig. 6).

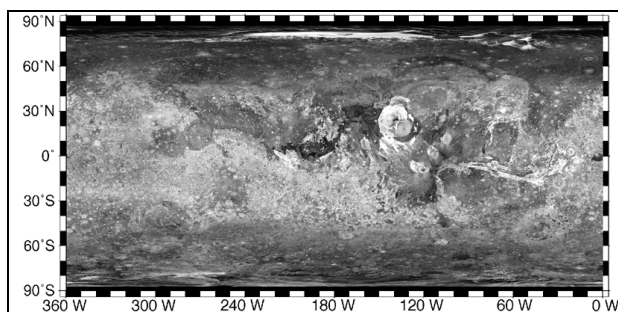


Fig. 2. Map of roughness at 0.3 km baseline. Brighter shades denote rougher surface.

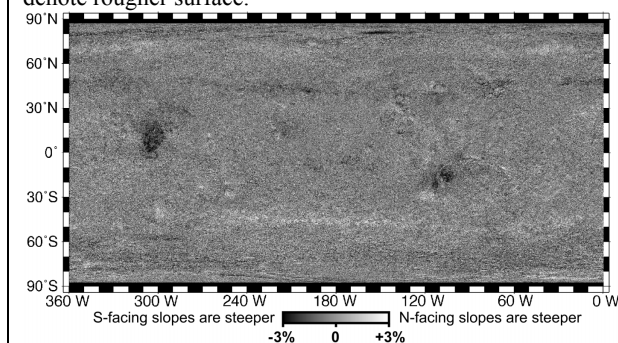
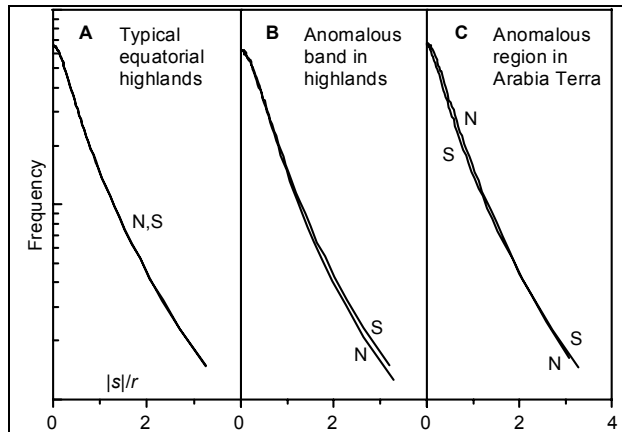


Fig. 3. Map of the north-south slope asymmetry parameter  $a$ . Brighter shades denote that north-facing slopes are steeper; darker shades denote that south-facing slopes are steeper.

**Anomalies Related to Regional Slopes.** Some even weaker but distinguishable deflection of the asymmetry parameter  $a$  from zero is associated with extended regional slopes of major volcanic constructs on Mars: their northern slopes show some prevalence of positive values of  $a$ , and their southern slopes show negative values. This effect is best expressed in Alba Patera and the Elysium rise. It is clear that these long smooth regional slopes do not bias the differential slope values. The downslope-facing small-scale slopes are steeper here.

At steep large-scale scarps on Mars (Valles Marineris walls, Olympus Mons scarps) the differential slope is unable to filter out regional topography well enough. Here the resolution of the MOLA data do not allow separation of the scarp topography and scarp face surface roughness.



**Fig. 4.** Frequency distributions of the differential slope  $s$  plotted against  $|s|/r$ . Normalization by  $r$  allows to compare the distributions for areas of different roughness. Use of  $|s|$  "folds" the distribution curve around the vertical axis. Letters N and S denote distribution branches for negative  $s$  (north-facing slopes) and positive  $s$  (south-facing slopes), respectively. Note the logarithmic scale along the frequency axis. **A**, typical equatorial highlands in Terra Cimmeria (20-30°S, 180-220°W); negative and positive branches coincide within the line width. **B**, the anomalous latitudinal band in Terra Cimmeria (43-47°S, 180-220°W); for relatively steep slopes  $|s| > \sim 1.5r$ , the positive branch goes above the negative one producing the positive median; for much steeper slopes, well outside the plot frame, the negative branch would exceed the positive one. **C**, the anomalous area in south-east Arabia Terra (250 km around 10°N, 305°W); for relatively gentle slopes  $|s| < \sim 2r$ , the negative branch goes above the positive one producing the negative median; for steeper slopes, the positive branch slightly exceeds the negative one.

*Other Anomalies.* The highest calculated absolute values of the asymmetry parameter  $a \approx -5\%$  are in a compact area at  $\sim 80^\circ\text{N}$  140-160°W (Fig. 3), where the MGS track direction deflects strongly from the meridian. This is due to the interference of the MGS track orientation with the strongly anisotropic topography of the transverse dunes in Olympia Planitia.

The next strongest asymmetry is observed in a few regions in the equatorial zone. The region in south-east Arabia Terra (10°N 305°W) just to the west of Syrtis Major, and Syria Planum (15°S 95°W) have an asymmetry parameter  $a \approx -2.5\%$ ; south-facing slopes are steeper in these areas. An anomaly of the same sign is observed in north-east Daedalia Planum (20°S 105°W), and of the opposite sign in south-east Daedalia Planum (30°S 105-115°W). The latter two areas are also known to be anomalous in another statistical characteristics of along-track MOLA topography: in this region there is a strong prevalence of concave topographic profiles [5]. There are several less pronounced local anomalies.

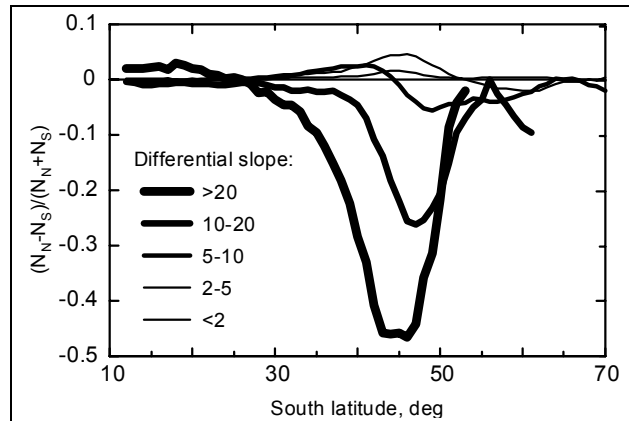


**Fig. 5.** Asymmetry of differential slopes calculated within 150-km wide latitudinal zones in Terra Cimmeria (180-220°W) and plotted against latitude. The measure of asymmetry is  $A = (N_N - N_S) / (N_N + N_S)$ , where  $N_N$  and  $N_S$  are numbers of steep N- and S-facing segments in all MOLA profiles. Different curves corresponds to different ranges of differential slopes in degrees, as shown.

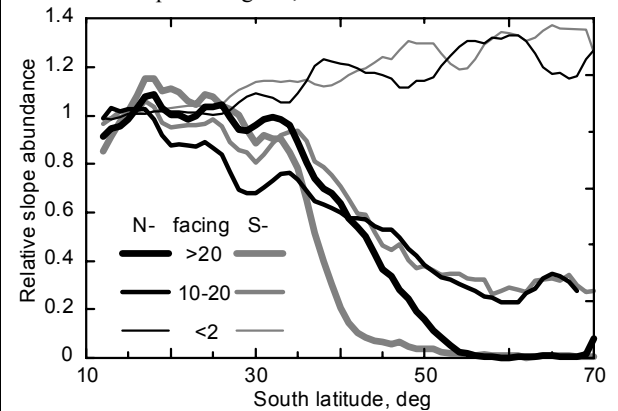


**Fig. 6.** Abundance of N- and S-facing slopes relative to that of the typical equatorial highlands plotted against latitude for Terra Cimmeria (180-220°W). Actually plotted quantity is the proportion of the MOLA profile segments of proper steepness and slope direction within given 150-km wide latitudinal zone normalized by the same proportion for 10°S - 20°S zone representing "typical equatorial highland". Different curves correspond to different ranges of slopes in degrees, as shown; black curves, N-facing slopes, gray curves, S-facing slopes.

Fig. 4C shows the differential-slope-frequency distribution asymmetry for the anomalous areas in Arabia Terra. It is seen that the nature of the anomaly differs from that of the latitudinal band (Fig. 4B): here the difference between north- and south-facing slopes is noticeable for gentle slopes, below  $r \approx 1^\circ$ , while only the steep slopes contributed to the asymmetry in the latitudinal bands. For the other local anomalous areas mentioned above the character of asymmetry is similar to that of the area in south-east Arabia: the gentle and

moderately steep slopes contribute to the observed asymmetry.

**Discussion:** The slope asymmetry data derived from MOLA altimetry presented here (Fig. 3) and high-resolution images illustrating individual examples of geological processes that might produce the statistical slope asymmetries, are at substantially different scales. This precludes the direct correlation of specific slope asymmetry values with individual geological features in specific MOC images, although regional characterizations and correlations can be made.

*Equatorial Anomalies:* High-resolution MOC images show that the whole of Arabia terra and the anomalous areas in eastern Daedalia Planum and Syria Planum are covered with dust or sand deposits [6]. Recent modeling of global atmospheric circulation at different obliquity [7] showed that Arabia Terra and the Tharsis rise are probable regions of dust deposition for all epochs in Martian history, which is consistent with the morphology observed in high-resolution images. Asymmetry of gentle slopes in this area could be caused by prevailing winds, a factor important in the formation of hectometer-scale topography. The fact that the asymmetry is observed only in a small part of Arabia could be because asymmetry in other parts is in an east-west direction or simply absent due to specific wind patterns. The anomalous areas in Daedalia and Syria are the only areas within Tharsis rise where extensive coverage of the surface with loose material is observed in high-resolution images.

The weak slope asymmetry at the regional slopes is easily explainable. Regional slopes themselves are an obvious natural cause of small-scale slope asymmetry. The observed asymmetry on the large shield volcanos is, at least partly, due to downslope-facing lava flow fronts.

*Latitudinal Anomalous Bands.* The approximate symmetry relative to the equator strongly suggests that the role of insolation was important in the formation of the anomalous bands. These bands lie within much wider zones in which the difference in the year-average insolation between pole- and equator-facing slopes is high. If the insolation asymmetry were the only reason for the effect, we would expect much wider zones.

The anomalous bands are within wider transitional zones between smoothed high-latitude to rougher low-latitude zones (see Fig. 2; also [5]). The same zones possess a number of peculiarities, and contain a number of different morphological features of zonal occurrence, including recent gullies [e.g., 6], which preferentially occur on pole-facing slopes. Costard et al. [8] have interpreted these gullies to be due to melting of ground ice at higher obliquity. Their calculations

showed that starting from  $\sim 35^\circ$  obliquity, the maximal day-average temperature reaches the ice melting point at high latitudes; for higher obliquity the day-average temperature exceeds  $0^\circ\text{C}$  at pole-facing slopes at lower latitudes, up to  $45^\circ$  latitude at  $45^\circ$  obliquity at  $20\text{-}30^\circ$ -steep slopes. Transient melting of ground ice in summer is responsible for formation of gullies and other features, promotes downslope movement of material and removes steep slopes. At midlatitudes, this process preferentially occurs at the pole-facing slopes, making these slopes less steep and producing the observed strong asymmetry of the steepest slopes. Summer-time creep (without melting) of thin sheets of ice-rich material on steep slopes can contribute to the observed effect in a similar way. During periods of moderately high obliquity, when the atmospheric water is abundant, but pole-facing slopes are still colder in summer, preferential  $\text{H}_2\text{O}$  frost and ice accumulation could occur at pole-facing slopes. This would favor glacial modification of these slopes. The latter effect, however, cannot be solely responsible for the observed asymmetry, because it would not have so narrow a latitudinal occurrence.

Our interpretation of the zonal bands of slope asymmetry as a result of transient melting at high obliquity indicates that transient melting of ground ice contributes to the latitudinal trend of roughness on Mars. Another obvious contributor is the high-latitude ice-rich mantle [5].

**References.** [1] Smith D. E. et al. (2001) *JGR*, 106, 23689 – 23722. [2] Howard, A. D. et al. (1982) *Icarus*, 50, 161-215. [3] Neumann, G. A., et al. (2001) *JGR*, 106, 23753-23768. [4] Kreslavsky, M. A., and J. W. Head (2000) *JGR*, 105, 26695 – 26712. [5] Kreslavsky, M. A., and J. W. Head (2002) *GRL*, 29, 10.1029/2002GL015392. [6] Malin M. C. and Edgett K. S. (2001) *JGR*, 106, 23429 - 23570. [7] Haberle, R. M., et al. (2003) *Icarus*, 161, 66-89. [8] Costard, F. F. et al (2002) *Science*, 295, 110-113.

**PRESSURE BALANCE AT MARS AND SOLAR WIND INTERACTION WITH THE MARTIAN ATMOSPHERE.** A. M. Krymskii<sup>1</sup>, N. F. Ness<sup>2</sup>, D. H. Crider<sup>3</sup>, T. K. Breus<sup>4</sup>, M. H. Acuna<sup>5</sup> and D. Hinson<sup>6</sup>.  
<sup>1</sup>Rostov State University, Rostov-on-Don, Russia, <sup>2</sup>Bartol Research Institute, University of Delaware, Newark, DE, USA, <sup>3</sup>The Catholic University of America, Washington, DC, USA, <sup>4</sup>Space Research Institute (IKI), Moscow, Russia, <sup>5</sup>NASA-Goddard Space Flight Center, Greenbelt, MD USA, <sup>6</sup>Center for Radar Astronomy, Stanford University, Stanford, CA, USA.

**Introduction:** The strongest crustal fields are located in certain regions in the Southern hemisphere. In the Northern hemisphere, the crustal fields are rather weak and usually do not prevent direct interaction between the SW and the Martian ionosphere/atmosphere. Exceptions occur in the isolated mini-magnetospheres formed by the crustal anomalies. Electron density profiles of the ionosphere of Mars derived from radio occultation data obtained by the Radio Science Mars Global Surveyor (MGS) experiment have been compared with the crustal magnetic fields measured by the MGS Magnetometer/Electron Reflectometer (MAG/ER) experiment. A study of 523 electron density profiles obtained at latitudes from +67° to +77° has been conducted. The effective scale-height of the electron density for two altitude ranges, 145-165 km and 165-185 km, and the effective scale-height of the neutral atmosphere density in the vicinity of the ionization peak have been derived for each of the profiles studied. For the regions outside of the potential mini-magnetospheres, the thermal pressure of the ionospheric plasma for the altitude range 145-185 km has been estimated. In the high latitude ionosphere at Mars, the total pressure at altitudes 160 and 180 km has been mapped. The solar wind interaction with the ionosphere of Mars and origin of the sharp drop of the electron density at the altitudes 200-210 km will be discussed.

**VOLUMETRIC/MORPHOMETRIC ANALYSIS OF IMPACT CRATERS IN THE NORTHERN HEMISPHERE LOWLANDS, MARS.** K. Kurita and Y. Ogawa, Earthq.Res.Inst., University of Tokyo, Yayoi 1-1-1, Bunkyo-ku, Tokyo 113-0031, Japan kurikuri@eri.u-tokyo.ac.jp.

**Introduction:** At the early stage of the martian history, a dense thick atmosphere has been suggested to exist. Considering the present state of thin atmosphere, large amount of CO<sub>2</sub> should be stored somewhere in the martian crust. To detect, characterize and quantify this volatile reservoir is one of the important tasks expected for the geomorphological study on the martian surface features. To determine the amount of this reservoir and to understand its formation process are the direct target of these researches.

Among several surface features morphology of impact craters is expected as an potential measure for the subsurface reservoir of the volatiles since excavation process associated with cratering efficiently plows the subsurface region. Several investigations have been conducted on rampart craters. Barlow and Bradley [1] suggest the target properties containing the volatiles control the lobate structure. Kuzmin[2] report spatial distribution of subsurface volatiles based on the onset size of rampart crater. Costard[3] focuses on the extent of fluidized ejecta to infer the volatile distribution. Here we will report results of volumetric/morphometric analysis of fresh impact craters in Utopia Planitia and south of Acidalia regions with an intention to characterize subsurface reservoir of volatiles.

**Data set:** The basic data sets are MOLA MEGDR (gridded 1/128 deg/pix data set) and Viking and MOC high resolution images. In the volumetric analysis we evaluated how the ejecta volume is partitioned around the cavity by subtracting the pre-cratering topography from the present one. The pre-cratering topography was estimated by interpolating the surrounding topography. We restricted the size of craters for the analysis between 8 to 20 km. 8 km is a minimum size for reliable estimate of ejecta volume based on the MEGDR MOLA data. We selected two regions in the northern hemisphere, region A; Utopia Planitia (225W-275W and 15N-45N) and region B; south of Acidalia (30W-75W and 15N-45N). Region A has been strongly suggested to stock the ground ice because the characteristic features such as polygons are exclusively observed on the surface[4]. Both regions cover the low elevation area where the water from the outflow channels could be inevitably ponded.

**Results:**

1) crater classification

In these two regions we could identify two different types of morphology as for the fluidized ejecta in the diameter range of 8 to 20 km. Fig. 1 represents typical features of these two types. Type A covers pedestal type craters and double-lobed rampart craters. The key feature of this type is existence of well-developed inner lobe with a faint trace of outer lobe.

The volume of the inner lobe is almost equivalent to the cavity volume except for the several cases at the high latitudes. Clear high resolution images indicate almost all pedestal type craters have aureole-like albedo change around the voluminous pedestal ejecta, which would be equivalent to the outer lobe of the double-lobed rampart craters in these regions. High resolution images also show radial striations/scours on the surface of the inner lobe, which are scratches caused by the flow event resulting in deposition of the outer lobe. This indicates the deposition sequence of two events; the inner lobe formed first and the outer lobe later. As a summary for the features of type A craters, double occurrence of ejecta deposition with different characteristics by a single impact event is a distinct nature. Particularly the existence of the delayed explosive event is remarkable. Type B on the other hand is basically single lobed rampart crater. In several cases multiple lobes are observed but they lack of well developed inner lobe.

2) Spatial distribution

We could classify craters into two types and their spatial distribution was determined. In the northern and low elevation regime in region A, Type A is dominant and in the southern and high elevation regime, Type B is dominant. Similar pattern can be seen in region B. Fig. 2 shows the histogram of crater counts in terms of the elevation. At the transition boundary of the elevation of -4000m the dominant type changes in both region A and B. It is interesting that this value coincides with the elevation of the Contact 1 of the paleo-shoreline in these regions proposed by Head et al[5]. If paleo-ocean existed, it can be said that Type A craters were formed in the region once water covered.

**Speculation on the formation of Type A crater:** To generate double deposition events by a single impact in the case of Type A craters, a process with time-delayed nature should be involved. Formation of vapor plume above the cavity[6] and segregation in the ejecta curtain[7] can explain time-delayed vapor-rich explosive event. Formation of striation/scours on the surface suggests icy blocks are contained in this gas-rich flow. Since Type A is dominant in the paleo-ocean region we suspect large and extensive development of subsurface reservoir of volatiles in this region.

**References:**

- [1] Barlow, N. and T.L. Bradley, (1990) *Icarus* 87, 156-179. [2] Kuzmin, et al., (1989) *Solar System Res.*, 22, 121-133. [3] Costard, F., (1989) *Earth Moon & Planets*, 45, 265-290. [4] Hiesinger and J. Head, (2000) *JGR* 105, 11999-12022. [5] Head et al., (1999) *Science* 286, 2134-2137.

[6] Stewart et al.,(2001) Lunar Planet.Sci. XXXII,2092,  
 [7] Scultz,P.(1992) JGR 97,975-1005,Barnouin-  
 Jha,O.S. and P.Scultz (1996) JGR 101,21099-21115

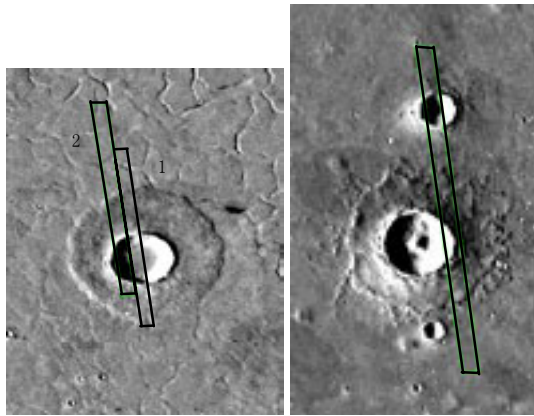


Fig 1a. Type A

Fig 1b. Type B

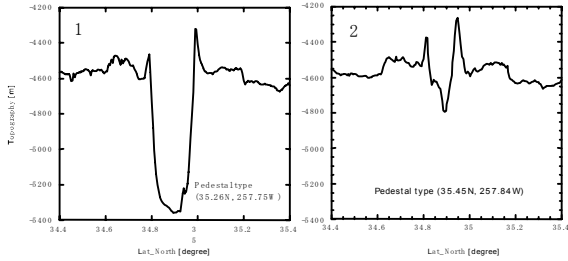


Fig.1c Topography profile of Type A along the inserted lines in Fig 1a.

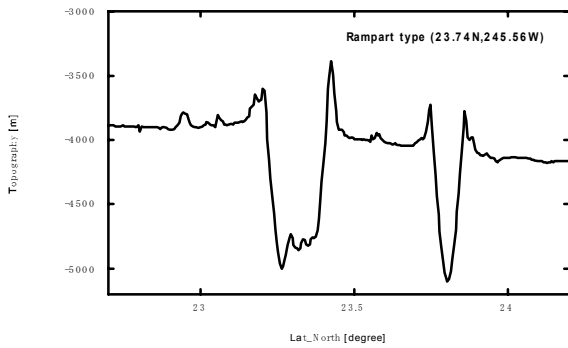


Fig.1d Topography profile of Type B along the inserted line in Fig 1b.

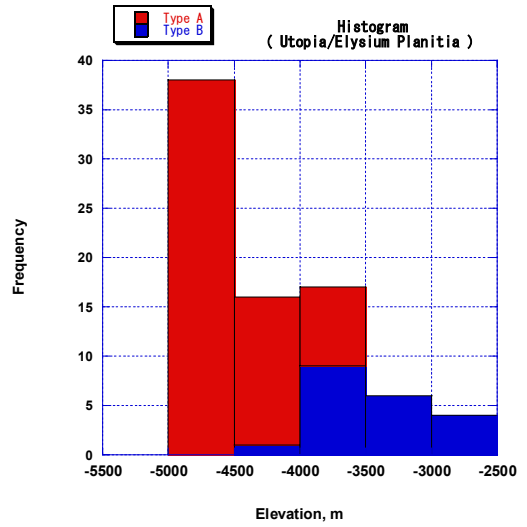


Fig.2a. Histogram of crater counts with elevation in region A

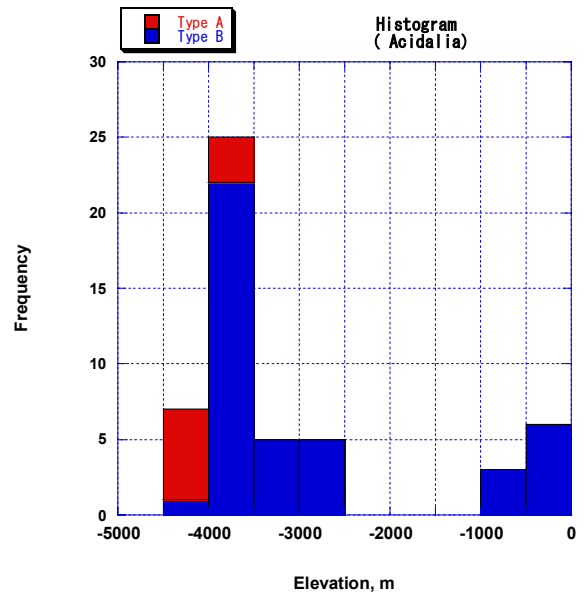


Fig 2b. Histogram of crater counts with elevation in region B

**CERBERUS PLAINS VOLCANISM: CONSTRAINTS ON TEMPORAL EMPLACEMENT OF THE YOUNGEST FLOOD LAVAS ON MARS.** P. D. Lanagan and A. S. McEwen; Lunar and Planetary Laboratory, University of Arizona, Tucson AZ 85721 (planagan@lpl.arizona.edu).

**Introduction:** The Cerberus Plains (CP) (Fig. 1) are located on the southeastern margin of the Elysium Rise and extend for over 3000-km from east to west and ~600-km from north-to-south. The plains are bounded to the northwest by the Athabasca Valles outflow channel and ridged Elysium lavas, to the north by cratered, knobby terrains, and to the south by the Medusae Fossae Formation and ridged plains. The Marte Valles outflow channel joins the eastern Cerberus Plains with the lower-elevation western Amazonis Planitia. A system of WNW-ESE trending fissures of the Cerberus Fossae cut across the Cerberus Plains, the northern knobby terrains, and portions of the ridged Elysium lavas.

Since the Cerberus Plains exhibit smooth surfaces at Viking image resolutions and few impact craters, [1] and [2] interpreted this region as being the youngest on Mars and defined this region as the referent for Upper Amazonian units. The presence of teardrop islands in Marte Valles and the smooth character of the plains led them to interpret the surfaces in this region as fluvial deposits from floods emanating from Cerberus Fossae. On the basis of USGS Viking-based topographic maps which indicate that the plains lay in a closed basin, Scott and Chapman [3] interpreted surfaces in the region as pluvial sediments deposited on top of volcanic surfaces by a paleolake which subsequently debouched through Marte Valles and westward in the southwestern plains. However, Plescia [4, 5] noted the presence of sparsely cratered, lobate, convex-ridged surfaces with morphologies consistent with unmodified lava flows and interpreted the surfaces to be lava flows filling pre-existing fluvial channel systems. MOC images confirmed that these plains are covered by lava flows, and that they are very similar to flows in Iceland [6]. Sakimoto [7] identified several shields, edifices, and lava flows and argued for a period of plains-style volcanism in this region.

We examine the spatial and stratigraphic relationships between Cerberus Plains volcanic units and surrounding units and derive constraints for volumes of volcanic materials extruded and the duration of volcanic activity within the Cerberus Plains.

**Major Features of the Cerberus Plains:** Both Mars Orbiter Laser Altimeter data and high-resolution Mars Orbiter Camera (MOC) images were used in this study. A digital elevation model (DEM) and shaded relief map of the Cerberus Plains and Amazonis Planitia were produced from MOLA data

using the natural-neighbor interpolation technique [8]. Mars Orbiter Camera (MOC) narrow angle images of the Cerberus Plains and Amazonis Planitia with resolutions up to ~1.5 m/pixel [9] were also examined. MOC images, while covering a very small fraction of the entire Cerberus Plains, are useful for examining meter-scale morphologies of surfaces.

**Lava Plains:** The MOLA DEM shows the Cerberus Plains exhibits extremely low gradients with regional slopes on the order 0.025 degrees. In some isolated locales, knobby terrains with relief on the order of 200-300 m, rims of large (> 20-km diameter) craters, and 100-m amplitude wrinkle ridges are visible. A low amplitude topographic divide trending roughly NE-SW southeast of Athabasca Valles splits the CP into the western Cerberus Plains (WCP) and eastern Cerberus Plains (ECP). In the ECP, surfaces generally slope downward to the east towards Marte Valles (MV).

Several shields measure up to ~100-km in basal diameter and rise up to ~100-m elevation above the surrounding plains. Linear edifices lie on portions of the trace of the Cerberus Fossae and measure up to several 100-km in length and have elevations of several 10's of meters above the surrounding terrains. Extending from many of these shields and linear edifices are large lava flows which extend downslope in length from 10's of kilometers to over 1000-km and in width from several kilometers to over 100-km. Several of these lobes extend into Marte Valles, truncate kilometer-wide, 20-m deep dendritic depressions near the proximal end of MV, and terminate in southwestern Amazonis Planitia (AP). The surfaces of some of the flow lobes exhibit a central depression down the long axis of the deposit. Many of these units overlap, suggesting they were emplaced at different times. The flow fronts within the ECP and southwestern AP are as high as 40-m. In the WCP, flow fronts, which often bound wrinkle ridges, are nearly undetectable in the shaded relief map; however, there are local variations of ~5-10-m in topography in places.

Narrow angle MOC images show that many of the surfaces within the Cerberus Plains are covered by platy-ridged surfaces, patterned surfaces, and surfaces exhibiting topography indicative of inflated lava flows (Fig. 2). Platy-ridged surfaces are comprised of plates 100-1000-m long which appear to have been rafted apart. These plates often appear to fit together like a jig-saw puzzle, exhibit shear structures around positive relief features, and have ridges ~10-m in height (as derived from shadow measurements).

Between plates are smooth areas (at MOC scales) covered by small-scale polygons approximately a few 10's of meters in diameter. Shading relationships indicate that the edges of the polygons appear to be depressions and do not show signs of warping upwards at their edges, as is typical from cooling and contraction of ponded lava.

The margins of some of the platy-ridged surfaces are bounded by surfaces which are composed of small, positive relief elongated bumps often a few 10's of meters across which exhibit a mottled appearance at MOC resolutions. In many places, the surface appears to have risen around positive topographic features such as small knobs, ridges, or crater rims, like inflated lavas.

Martian platy-ridged surfaces have been interpreted as insulated sheet lava flows based on comparisons with Icelandic flows with similar platy-ridged morphologies [6]. According to Keszthelyi et al. [6], insulated sheet flows initially form as inflated pahoehoe fields. A surge in the eruption rate forces more lava to be injected into the flow than the lava tubes can conduct; as a result, the surface of the pahoehoe flow is disrupted into large (100-m to km long plates) and rafted downslope. Such lava flows on Earth often show shear structures where lava flows around and over obstacles, compressional ridges, and lobate margins [6]. The martian surfaces in this region display each of these characteristics.

Patterned surfaces are consistent with chilled ponded lavas. As ponded lavas cool, tensional cracks form at the surface, thus resulting in a patterned appearance to these lavas. Terrestrial examples of such lavas occur in former lava lakes such as Kilauea Iki [10]. As noted previously, patterned morphologies are noted on the margins of insulated sheet flows. That suggests that lavas at the margins of the platy-ridged flows were ponded and stagnant as they cooled. Patterned lavas are also noted in intra-plate regions within insulated sheet flows. This suggests that, in these regions, an initially ponded lava was allowed to cool to the point where cooling cracks formed on the surface until a surge in the eruption rate caused the ponded surface to break into plates which were subsequently rafted.

The hummocky and mottled appearance of some surfaces is consistent with those expected of tube-fed inflated pahoehoe fields. During early emplacement of such lavas, small topographic barriers dam or divert initially thin lava flows. As the eruption continues, lava injected under the cooler, hardened surface via tubes lifts the surface of the flow above the initial barrier. In the Laki flow, inflated lavas are found near the margins of platy-ridge flows. A similar relationship is found within the Cerberus Plains.

*Medusae Fossae Formation:* The Medusae Fossae Formation (MFF) bounds the southern portions of the Cerberus Plains and Amazonis Planitia. The maximum elevation of these units is approximately 1-km over the CP. Large valleys are noted within the MFF with elevation excursions of several 100-m. MOC images of the MFF reveal massive friable deposits exhibit weak, large scale layering and yardangs. In several locations, most notably in southern Amazonis Planitia and south of Athabasca Valles, these friable materials clearly overlie nearly pristine platy-ridged surfaces [9]. However, lava flows appear to embay the lower members of the MFF in the extreme southwestern and southeastern portions of the CP. These observations suggest that periods of lava emplacement and MFF deposition are interweaved.

The lava surfaces eroding out from under the MFF are well-preserved and not noticeably eroded, thus suggesting that the MFF may be made of low density materials. Additionally, the MFF has been associated with regions of low radar backscatter, also consistent with low density materials. Radar-stealthy portions of the MFF may be reticulate, deposits of high porosity pyroclastic materials [6].

*Fluvial Channels:* Streamlined knobs, anastomosing channels, and longitudinal grooves are noted in both Athabasca Valles and Marte Valles [11]. The edges of several pristine flow lobes are visible on the banks of Athabasca Valles. In Marte Valles, while the channel appears to cut through older lavas, the channel floor is embayed by platy-ridged lavas.

**Discussion:** *Volume estimates for volcanics:* The areas covered by lava flows which postdate the last fluvial event in Marte Valles in the western Cerberus Plains is approximately  $1.7 \times 10^5$ -km<sup>2</sup>. Areas covered by post Marte Valles lavas originating in the ECP is approximately  $9.3 \times 10^5$ -km<sup>2</sup>. The total area of the Cerberus Plains lavas emplaced after the last Marte Valles fluvial episode is  $1.1 \times 10^6$ -km<sup>2</sup>. Identifiable individual flows vary widely in area, from several small flow lobes in the vicinity of the Cerberus Fossae with areas of  $\sim 1000$ -km<sup>2</sup> to a flow which terminates in the proximal end of Marte Valles with an area of  $\sim 72000$ -km<sup>2</sup>.

Estimates on the thicknesses of individual lava flows may be obtained through flow front height measurements, and estimates on the thicknesses of a package of overlapping lava flows may be obtained from an examination of craters embayed and partially filled by lavas. In the WCP, the few recognizable flow fronts are no larger than 10-m in height. However, wrinkle ridges with amplitudes of  $\sim 90$ -m disappear under the embaying lavas, so the total thickness of WCP lavas may be  $>100$ -m thick in some places.

In the ECP, individual flow fronts identified in the shaded relief map range in heights between 20-40 m. Based on partially filled craters, Plescia [4, 5] estimated that the average thickness of the eastern Cerberus Plains volcanics was approximately 200-m. However, as the post-MV flows may have been emplaced over pre-MV flows, this is likely an upper bound for total thicknesses of the ECP flow fields.

The 72000-km<sup>2</sup> flow identified above has a flow front thickness of ~25-m, which indicates that the flow would have a volume of 1800-km<sup>3</sup>. Assuming thicknesses of WCP lavas range between 10-100 m, likely volumes for WCP lavas range between 1.7x10<sup>3</sup>-1.7x10<sup>4</sup> km<sup>3</sup>. Assuming the total average thicknesses of post-Marte Valles flows in the ECP range from 25-200-m, the likely volumes for ECP lavas range between 2.3x10<sup>4</sup>-1.8x10<sup>5</sup> km<sup>3</sup>. The total volumes of post MV lavas in the CP would range between 2.5x10<sup>4</sup>-2.0x10<sup>5</sup> km<sup>3</sup>.

*Age of Most Recent Volcanism:* Statistics of small craters have indicated that these lava surfaces have model ages as young as 10 Ma [11, 12, 13]. However, most of the craters counted in all three of these studies may be secondary craters from a single 10-km primary crater [14]. Craters larger than 1-km diameter are much more reliable for age estimates. Plescia [4, 5] counted 89 craters larger than 1-km diameter over the plains, suggesting an age of 200-500 Ma. However, we concur with [12] that many of these large craters are embayed by the youngest lavas. In fact, we have not found a single large crater directly superimposed over the youngest lavas. There is one 0.5 km crater superimposed over the lava, seen from MOC images covering a total of 6600 km<sup>2</sup>. This single crater, if it is a primary crater, suggests an age for the lava of less than 100 Ma according to the chronology of either Hartmann or Neukum [15].

*Time to Emplace CP Volcanic Fields:* Modeling of insulated sheet flows suggest that the average eruption rates for CP lavas were likely on the order of 10<sup>4</sup>-m<sup>3</sup>/s [6]. At such a rate, a flow with a volume of 1800-km<sup>3</sup> would be emplaced in roughly 6 years. As this volume applies to one of the larger lava flows, this suggests that individual lava flows were em-

placed in time periods of less than a decade. Smaller lavas emplaced at this volumetric rate would correspondingly be emplaced in less time. For the volumes of all post-MV lava flows calculated in the previous section, all post-MV flows would be emplaced within roughly 30-300 years. Crater counts have been interpreted to indicate that there is an age difference of at least several 10's of millions of years between lavas in Marte Valles and Athabasca Valles [11]. If this is correct, then it is likely that there were significant periods of quiescence between volcanic events.

*Vent Migration:* Vent activity appears to migrate westward with time. Lava flows originating from western portions of the CF tend to overlie flows originating from more eastern portions of the CF. This trend echoes the conclusion of Burr et al. [11] that channels in the region tend to be younger the further west they are located. The migration of loci for volcanic eruptions, source regions for outflow channels, and the continued extension of the Cerberus Fossae suggest that the regional stress field is not static.

**References:** [1] Scott D.H. and Tanaka K.L. (1986) *USGS Misc. Invest. Ser. Map I-1802-A*. [2] Tanaka K.L. (1986) *JGR*, 91, E139-E158. [3] Scott D.H. and Chapman M.G. (1995) *USGS Misc. Invest. Ser. Map I-2397*. [4] Plescia J.B. (1990) *Icarus*, 88, 465-490. [5] Plescia J.B. (1993) *Icarus*, 104, 20-32. [6] Keszthelyi, L.P. et al. (2000) *JGR*, 105, 15027-15050. [7] Sakimoto, S.E.H. et al. (2001) *AGU FM 2001*, Abstract #P31B-09. [8] Abramov, O. and McEwen A.S. (2001) *AGU FM 2001*, Abstract # P42A-0567. [9] Malin, M.C. and Edgett, K.S. (2001) *JGR*, 106, 23429-23570. [10] Green, J. and Short N.M. (1971) *Volcanic Landforms and Surface Features*. [11] Burr D.B. et al. (2002) *Icarus*, 159, 53-73. [12] Hartmann, W.K., and Berman, D.C. (2000) *JGR*, 105, 15011-15026. [13] Berman, D.C. and Hartmann, W.K. (2002) *Icarus*, 159, 1-17. [14] McEwen, A.S. (this conference). [15] Neukum, G. et al. (2001) *SS.Rv.*, 96, 55-86.

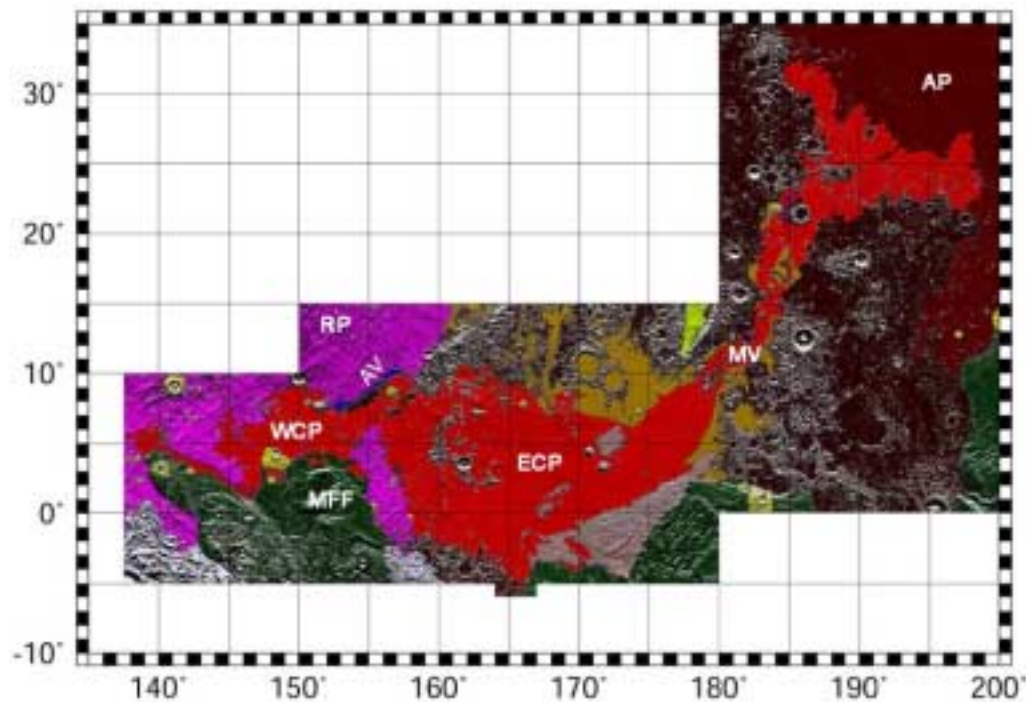


Figure 1: Shaded relief map of the Cerberus Plains and vicinity. Colors indicate geomorphic provinces. Units described in this paper are as follows: red - lavas emplaced after last Marte Valles fluvial episode; blue - fluvial surfaces; green - Medusa Fossae Formation; purple - ridged plains; brown - highland remnants. Abbreviations for regions are as follows: WCP - Western Cerberus Plains; ECP - Eastern Cerberus Plains; AV - Athabasca Valles; MV - Marte Valles; AP - Amazonis Planitia; MFF - Medusa Fossae Formation; RP - ridged Elysium Plains.

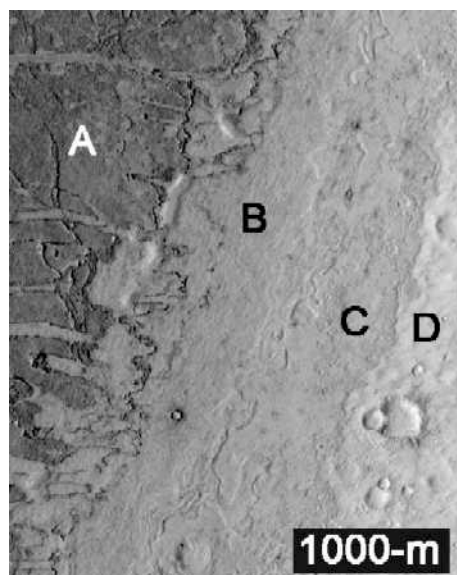


Figure 2: MOC image M07/02340 showing different morphologies of lava surfaces. A - platy-ridged lavas; B - patterned lavas; C - inflated lavas; D - cratered terrain.

**A STUDY OF MERIDIANI PLANUM, MARS, USING THEMIS DATA.** Melissa D. Lane<sup>1</sup>, Phillip R. Christensen<sup>2</sup>, William K. Hartmann<sup>1</sup>, and the THEMIS Science Team, <sup>1</sup>Planetary Science Institute, 620 N. 6<sup>th</sup> Avenue, Tucson, AZ 85705 (lane@psi.edu, hartmann@psi.edu), <sup>2</sup>Dept. of Geology, Box 871404, Arizona State University, Tempe, AZ 85287-1404 (phil.christensen@asu.edu).

**Introduction:** Recently two landing sites were selected for the upcoming Mars Exploration Rover (MER) missions that will be sent to the surface of Mars in the summer of 2003 and will land in early 2004. The chosen locations are Gusev Crater and Meridiani Planum. This work will focus on characterizing the Meridiani Planum landing site region using data from the Thermal Emission Imaging System (THEMIS) instrument aboard the currently orbiting Mars Odyssey spacecraft.

The Meridiani Planum region of Mars is known to host gray, possibly platy, hematite [1,2] in occurrence with basalt [3]. The THEMIS instrument operates in both the VIS and thermal IR wavelengths as a push-broom, multispectral imager. THEMIS hosts 5 VIS bands and 10 IR bands. THEMIS is a spacecraft-mounted, nadir-looking instrument whose IR and VIS camera focal planes have 320 and 1024 across-track picture elements (pixels), respectively. For additional details regarding the instrument characterization see [4].

This study utilizes single-band images from the visible (VIS), daytime infrared (IR), and nighttime IR data for crater population analyses and also multi-band daytime IR data for compositional analyses.

**Single-band Crater Population Studies:** Numerous crater population studies of various planetary bodies have been conducted to ascertain the relative ages of geologic units exposed at the surface [e.g., 5-13]. Spacecraft images from the Ranger, Lunar Orbiter, Surveyor, and Apollo missions (as well as the Soviet Luna and Zond missions) have provided views of the craters on the lunar surface. These craters have been correlated with age dates determined for the lunar samples that were returned during the Apollo and Luna missions. From those and other studies absolute ages for various lunar surfaces have been determined [e.g., 14-18]. For other planetary bodies, such as Mars, from which there has been no sample return from specific locations on the planet (i.e., within specific geologic units), estimated surface ages are ascertained by applying the lunar crater production curve using Martian crater scaling laws. Scaling laws account for various differences between the Moon and Mars, such as surface gravity, crustal strength, density and structure of the body, impact velocity, and proximity to the asteroid belt or the presence of a Martian atmosphere that may affect the production of secondary craters [e.g., 9,14,15,19].

To date, visible images (photographs) traditionally have been used for crater population studies. Currently the Mars Odyssey spacecraft Thermal Emission Imaging System (THEMIS) instrument is acquiring images both in the visible (VIS) and thermal infrared (IR) ranges of the electromagnetic spectrum. One focus of this study is the utilization of the recently acquired THEMIS data for determining ages of Martian surfaces, and especially the viability of using thermal images, in addition to visible images, to conduct such counts. The capability of utilizing the thermal images for crater population studies is advantageous because by the end of the Mars Odyssey nominal mission, THEMIS will provide unprecedented full global coverage at 100-m spatial resolution. Another focus of this work is to interpret the THEMIS crater counts in concert with a few additional Mars Orbiter Camera (MOC) counts to analyze the geological history of the Meridiani Planum landing site.

*Crater Counting Technique:* The craters in the THEMIS images used in this study were counted and their diameters were measured; no distinction was made on the basis of crater morphology or the possibility of being a secondary crater. These size-distribution results were compared to a known production function over a wide range of diameters,  $D$ . For this study the production function used was based on data of Hartmann and Neukum, as analyzed by [19]. This technique is limited to about 10% accuracy in crater-count numbers and an estimated factor of 2 to 4 in absolute age [20]. The plots used in this study are based upon  $R_{\text{bolide}}$  of 2.6, where  $R_{\text{bolide}} = (\text{bolides}/\text{km}^2 \cdot \text{yr on Mars}) / (\text{bolides}/\text{km}^2 \cdot \text{yr on the Moon})$  at a fixed bolide diameter. This is an average of  $R_{\text{bolide}} = 2.0$  from [19] and  $R_{\text{bolide}} = 3.15$  from Bottke [unpublished data]. Further discussions related to the determination of  $R_{\text{bolide}}$  can be found in [19-21].

*THEMIS Data Coverage:* The data of the Meridiani Planum landing site considered for the crater population portion of this study consist of orbits 968 through 2778. These orbits represent areocentric longitude  $L_s$  336 to 48, respectively, and were collected from 04 March 2002 to 31 July 2002. The spacecraft altitude was approximately 400 km, corresponding to a nadir data resolution of approximately 100 m/pixel for the infrared images and 18 m/pixel for the visible images. The images used in this study were all VIS-band

3 (centered at 0.652  $\mu\text{m}$ ) and IR-band 9 (centered at 12.57  $\mu\text{m}$ ) data because of the better image quality (e.g., atmospheric transparency).

The overlapping Meridiani Planum landing site ellipses (for either launch opportunity) are centered at 2.07 °S, 6.08 °W and are approximately 118-km long and 17-km wide, trending azimuthally at 86 and 88°. Within these ellipses data have been collected by the THEMIS instrument in order to support the landing site evaluation. This part of the study has focused on the THEMIS data that occur within the Meridiani Planum landing site to test the viability of using both VIS and IR images to conduct crater population studies and to determine the ages of the geologic units therein.

**Visible Imaging Data:** Four VIS THEMIS images were acquired of the Meridiani Planum landing site area: V01499001, V02585001, V01137001, and V01836001 (Figure 1). These images were all used for this crater population study. Within each image, only areas that occur within the landing site ellipses were analyzed in order to address the landing site characteristics specifically and all craters were counted. The crater counts for one representative area is shown in Figure 2 (crater counts for all four areas yielded similar results).

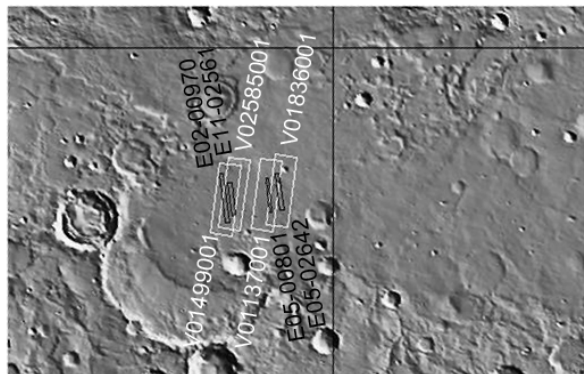


Figure 1: Map of the location of the THEMIS VIS images occurring within the proposed MER landing site in Meridiani Planum and related MOC images utilized in this study. The lat/lon lines represent 0°N and 5°W.

**Daytime Thermal Imaging Data:** The VIS images are nested within thermal IR daytime images acquired at the same time; however, the thermal images are 32-km wide whereas the visible images are only 18.4-km wide. Thermal IR daytime images that correspond to the above-mentioned visible data were analyzed for this study (i.e., I0498005, I02584004, I01136002, and I01835005, respectively). The areas counted in these data were restricted to the areas defined in the VIS

data discussed above (Figure 2) such that a direct comparison could be made.

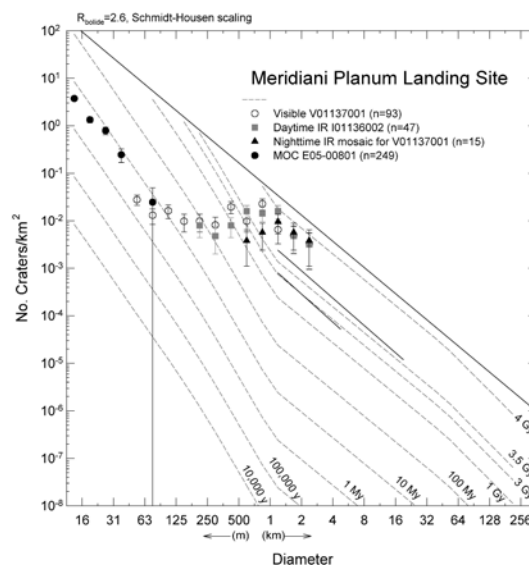


Figure 2. Crater diameter distributions for the VIS, daytime IR, and nighttime IR images within the landing ellipse. Error bars reaching the abscissa occur when there is only one crater for that size bin.

**Nighttime Thermal Imaging Data:** Seven nighttime images (I0099302, I01692007, I02416002, I02778002, I01330006, I01667003, I00968006) share areas within the Meridiani Planum landing site ellipses that are covered by the above-mentioned VIS and IR daytime images. The nighttime data tracks trend differently from the daytime tracks (i.e., NW-SE versus NE-SW), hence the single-track data do not exactly correspond to the restricted VIS and daytime IR areas counted and shown in Figures 1 and 2. Because of this difference, an image mosaic was constructed of the nighttime thermal IR images that allowed crater counts to be conducted in areas of the mosaic that do correspond to the areas covered by the VIS data (and related daytime IR data) shown in Figure 1. Nighttime count results are also plotted in Figure 2 for direct comparison of the visible/daytime IR/nighttime IR landing ellipse crater population study results.

**Results:** In each of the three THEMIS data sets (i.e., VIS, daytime IR, and nighttime IR) most craters of all diameters  $> \sim 63$  m have indistinct ejecta patterns in Meridiani Planum. There are few exceptions in the studied images. The lack of discrete ejecta likely is a result of physical weathering and degradation of the craters. The crater populations derived from the THEMIS data for the Meridiani Planum landing site area (Figure 2) do not follow any particular isochron,

but rather lie roughly horizontally on the plot, crossing many isochrons, in the diameter range of  $\sim 63 \text{ m} < D < 1 \text{ km}$ . This behavior suggests that the exposed surface does not represent a pristine, unaltered, single-aged surface, but rather suggests loss of craters by deposition and erosion in all but the largest size fractions. The largest craters ( $\sim 2\text{-km}$ -diameter) on the plots in Figure 2 approach the 4 Gy isochron. This relationship agrees with the counts of very old, degraded “fossil” craters in the broader Meridiani Planum area discussed by [22], which were found to cluster just below the saturation level. These data thus suggest that the landing site in Meridiani Planum is originally an ancient surface of approximately that age. Previous studies using higher resolution MOC data indicate that there exists a smaller-diameter (approximately 16 to 90-m), fresh, bowl-shaped crater population in the broader Meridiani Planum region that does follow the slope of the isochrons, suggesting a recent exposure age of this surface of approximately 10 My (perhaps in the range of 1-40 My) [22-24]. New counts of “fresh” craters were conducted for this work using MOC data (E02-00970, E11-02561, E05-00801, and E05-02642) that occur within the footprints of the VIS images (Figure 1,2). These new additional data trend with the production-function isochrons (between  $\sim 1$  and 10 My) implying that the smaller, younger craters in the Meridiani Planum landing site area have remained fairly pristine and that intense crater degradation was not occurring in this region in Mars’ recent geological history. It is possible that Mars is currently in a low-erosion era controlled by obliquity/climate variations as discussed by [25,26].

[5,7,11,13,27,28] discussed mathematical models of the effects of deposition and erosion on the Martian crater population, showing that prolonged erosion/deposition removes mid-sized craters and flattens the size distribution, but if that activity ends or dramatically declines, a new production-function size distribution will be established at small sizes. The shapes of the crater population curves generated for this study using THEMIS and MOC crater counts are essentially the same (Figure 2) and represent a dramatic example of this type of resurfacing history, supporting the early models.

Although the data resolution is different for the THEMIS VIS and IR images, the determined crater densities for the overlapping crater size bins in Figure 2 are similar between the visible and daytime IR counts. The nighttime IR counts, however, routinely plot at lower densities than the daytime IR counts because the number of craters are underestimated due to some thermal homogeneity of the surface at night; during the day solar illumination heats the crater walls

and other slopes allowing the warm areas and the thermal “shadows” to define the crater boundaries. Not only are some craters not identified using the nighttime IR data, but also, for several size bins where craters were identified using the daytime IR data, there were no craters identified using the nighttime data. Hence the age of the surface for any given size-fraction bin are underestimated in Meridiani Planum using the nighttime IR data.

The early Mars missions, such as Mariner 9 and Viking 1 and 2, provided fairly low resolution images of the planet, whereas the more recent Mars Global Surveyor mission provided high-resolution images from specific areas but lacked global coverage. By the end of the Mars Odyssey mission, the planet will be imaged globally in the midinfrared at 100-m/pixel resolution. There will be significant coverage at visible wavelengths, but likely not full global coverage. Hence the THEMIS images bridge the gap between the lower-resolution, global and higher-resolution, postage-stamp data sampled previously by earlier missions. It has been shown in this paper that the THEMIS IR data set can be used in the traditional manner for crater population studies (especially for the daytime images) and, because the thermal data set will be globally complete, it will be extremely useful for crater population studies of mid-sized craters on Mars. The shape of the crater population curves determined using THEMIS data show Meridiani Planum to be a dramatic example of an area on Mars that has had substantial crater obliteration (by erosion and deposition), followed by a cessation of crater degradation in the last  $\sim 10$  My.

**Multiple-band Compositional Analyses:** Figure 3 shows a mosaic of daytime IR images from the Meridiani Planum area of Mars. This mosaicked image is the result of a decorrelation stretch (DCS) of the data and assignment of bands 3, 5, and 8 to red, green, and blue, respectively.

The mosaic shows image-to-image color variations resulting from the DCS being performed for each image strip individually and because atmospheric correction has not been performed.

At this preliminary point, spectral emissivity studies are beginning and the varied colors in Figure 3 show that compositional differences are present. The area corresponding to the future landing site of the Mars Exploration Rover appears to be fairly homogeneous. The eroded, muted craters and other subtle geomorphic features seen in the Mars Observer Camera and THEMIS visible and daytime IR images of the landing site region support that this landing site area does not exhibit dramatic geology.

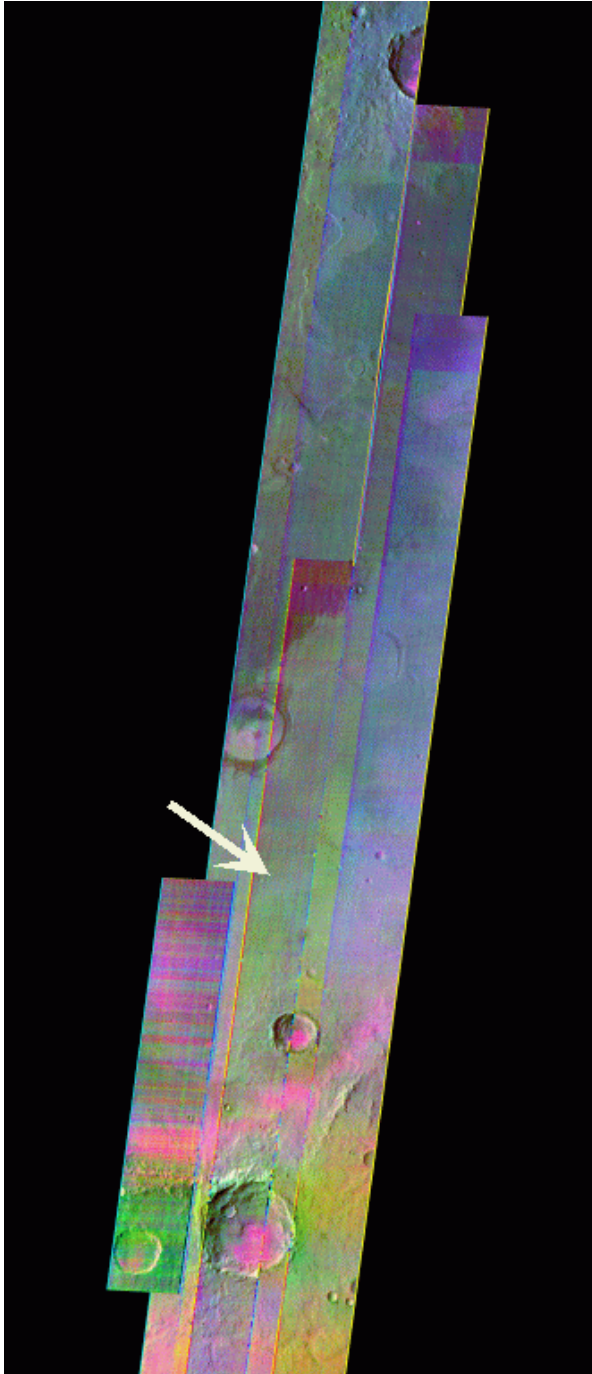


Figure 3: Mosaicked THEMIS daytime IR data of Meridiani Planum. The arrow points approximately to the western end of the Mars Exploration Rover landing site ellipse.

**References:** [1] Christensen, P. R. et al. (2000) *JGR*, 105, 9623-9642. [2] Lane, M. D. et al. (2002)

*JGR*, 107, doi:10.1029/2001JE001832. [3] Bandfield, J. L. et al. (2000) *Science*, 287, 1626-1630. [4] Christensen, P. R. et al. (2003) *Space Sci. Rev.*, in press. [5] Öpik, E. J. (1965) *Ir. Astron. J.*, 7, 92-104. [6] Hartmann, W. K. (1964) *Comm. Lun. Planet. Lab.*, 2, 197-203. [7] Hartmann, W. K. (1966a) *Icarus*, 5, 565-576. [8] Hartmann, W. K. (1966b) *Icarus*, 5, 406-418. [9] Hartmann, W. K. (1977) *Icarus*, 31, 260-276. [10] Hartmann, W. K. (1984) *Icarus*, 60, 56-74. [11] Chapman, C. R. (1974) *Icarus*, 22, 272-291. [12] Neukum, G. et al. (1975) *The Moon*, 12, 201-229. [13] Chapman, C. R. and K. L. Jones (1977) *Ann. Rev. Earth Planet. Sci.*, 5, 515-540. [14] Soderblom, L. A. et al. (1974) *Icarus*, 22, 239-263. [15] Neukum, G. and D. Wise (1976) *Science*, 194, 1381-1387. [16] Neukum, G. and K. Hiller (1981) *JGR*, 86, 3097-3121. [17] Neukum, G. et al. (2001) *Chron. and Evol. of Mars*, Kluwer Acad. Publ., 96, 55-86. [18] Stöffler, D. and G. Ryder (2001) *ibid*, 9-54. [19] Ivanov, B. A. (2001) *ibid*, 87-104. [20] Hartmann, W. K. and G. Neukum (2001) *ibid*, 165-194. [21] Hartmann, W. K. (1999) *Met. Planet. Sci.*, 34, 167-177. [22] Hartmann, W. K. et al. (2001) *Icarus*, 149, 37-53. [23] Kelsey, C. et al. (2000) *LPS XXXI*, Abstract #1524. [24] Lane, M. D. et al. (2001) *LPS XXXII*, Abstract #1984. [25] Mellon, M. T. and R. J. Phillips (2001) 106, 23165-23179. [26] Costard, F. et al. (2002) *Science*, 295, 110-113. [27] Hartmann, W. K. (1971) *Icarus*, 15, 410-428. [28] Chapman, C. R. et al. (1969) *J. Astron.*, 74, 1039-1051.

**Acknowledgments:** The isochron diagram corresponding to  $R_{\text{bolide}}$  value of 2.6 is available through the PSI website at [www.psi.edu/projects/mgs/cratering2.html](http://www.psi.edu/projects/mgs/cratering2.html). We thank Santa Barbara Remote Sensing (SBRS) of Goleta, CA for the development and construction of the THEMIS instrument and thank all of the staff at Arizona State University who have contributed to providing these data in a usable form. This work was funded through the Mars Data Analysis Program and the Mars Odyssey Participating Scientist Program.

**IN SITU NEUTRON SPECTROSCOPY ON THE MARTIAN SURFACE: MODELING THE HYDRA INSTRUMENT FOR DIFFERENT MISSION SCENARIOS.** D. J. Lawrence, R. C. Elphic, W. C. Feldman, K. R. Moore, T. H. Prettyman, and R. C. Wiens, Los Alamos National Laboratory, Mail Stop D466, Los Alamos, NM 87545 (djlawrence@lanl.gov).

**1. Introduction:** Planetary neutron spectroscopy has proven to be highly successful in remotely detecting and measuring the abundance of water on planetary surfaces such as Mars and the Moon [1,2]. Because of the central role played by water on Mars and the need to make in situ measurements of water abundances for landed missions, neutron spectroscopy is also being investigated as a technique for quickly determining the near-surface water abundance for future Mars missions, such as the Mars Smart Lander (MSL) [3,4,5].

We are currently developing a water- and hydrate-sensing instrument called “HYDRA” that is being supported by the NASA Mars Instrument Development Program (MIDP). Previous work has been supported by the NASA Planetary Instrument Design and Development (PIDDP) Program. A detailed description of the science justifications for the HYDRA instrument are given as a companion paper in this conference [5]. Here we focus on summarizing results of modeling work that demonstrates surface based neutron spectroscopy is indeed feasible and can be successfully carried for a wide variety of mission scenarios. In particular, we have investigated 1) the effects of mounting a neutron spectrometer (NS) on the body of a rover and/or lander; and 2) the effects of making neutron measurements in the presence of a radioactive thermal generator (RTG) that produces copious amounts of neutrons. In both of these situations, we have determined that robust measurements of water content can be made using the technique of neutron spectroscopy.

**2. Instrument Modeling** The most straightforward way to make neutron measurements on the Martian surface is to use  $^3\text{He}$  neutron detectors. These detectors are proportional counters filled with  $^3\text{He}$  gas that has a high probability for absorbing neutrons. Advantages of  $^3\text{He}$  detectors include a large efficiency for detecting neutrons, low mass ( $^3\text{He}$  sensors can be made for <100g), ruggedness ( $^3\text{He}$  sensors have survived shocks of up to 1500g's), and extensive space-flight heritage on NASA and Department of Energy based missions. Figure 1 shows a possible configuration of how a HYDRA instrument might be implemented. The configuration includes two  $^3\text{He}$  tubes where one is covered in a layer of Sn and the other is covered in a layer of Cd. As with the Lunar Prospector NS [6], the Cd covered tube measures epithermal neutrons and the Sn covered tube measures both thermal and epithermal neutrons. Thermal neutron measure-

ments are obtained by subtracting the Cd counting rates from the Sn counting rates.

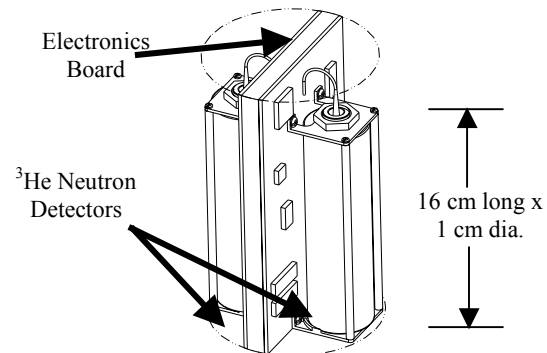


**Figure 1:** Schematic diagram of a rover based neutron detector.

Because HYDRA can be implemented on a variety of platforms (lander, rover, penetrator, borehole), the configuration of Figure 1 is only a template used for modeling purposes. The exact geometry of a particular instrument can be configured to the given application. We expect that a HYDRA instrument of the type shown in Figure 1 can be built having a mass of 500 g, power draw of 500 mW to 1W, and a data rate of ~1 bit per second.

For all portions of this study, we modeled the NS and its environment using the Monte Carlo code MCNPX [7]. MCNPX is being used extensively for the analysis of Mars Odyssey gamma-ray and neutron data [1,8].

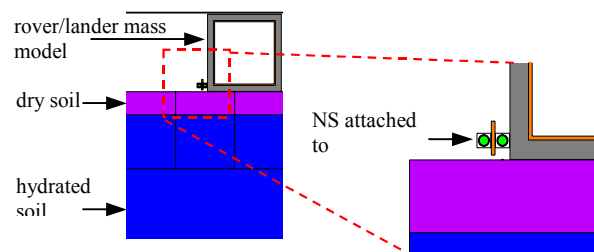


**Figure 2:** Drawing of the NS and environment used for the modeling of this study.

Figure 2 shows a drawing of the NS and surrounding environment used for this study. The NS shown in Figure 1 is mounted on a simplified rover/lander having a mass of 150 kg and is an approximation of the MER design [9]. For simplification, we have modeled the rover/lander mass as a  $(50\text{ cm})^3$  cube made of 90% aluminum and 10% computer board material. The computer board material is assumed to be 60% fiber-

glass and 40% epoxy. For the Martian surface, we have assumed a two-layer stratigraphy such that the top dry layer has a Pathfinder-type composition [10] and the semi-infinite bottom layer has the same soil composition with increasing admixtures of  $\text{H}_2\text{O}$ . Finally, we have modeled the Martian atmosphere as having a composition of 70.63 wt.% O, 26.48 wt.% C, 2.89 wt.% N, and a column thickness of  $16 \text{ g/cm}^2$ .

### 3. Modeling a NS on a rover/lander platform

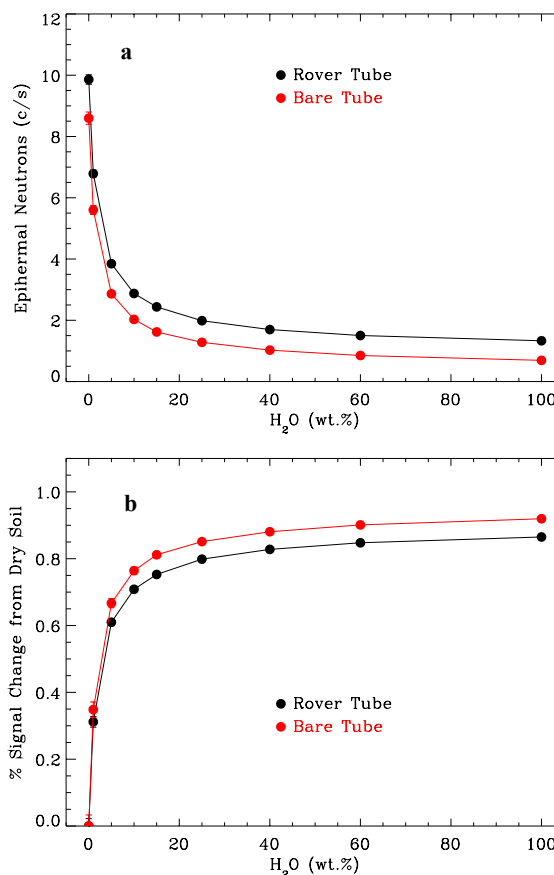
While the technique of planetary neutron spectroscopy is sufficiently well-developed to make robust measurements of water content from orbit, basic studies still need to be done to understand how well in situ neutron spectroscopy measurements can be made on the Mars surface. Issues we have studied include: 1) It is likely that any rover-based neutron detector will have to be mounted directly on the rover and/or lander. What is the effect of the rover/lander material, including hydrogen, on the hydrogen detection capabilities of a neutron detector? Will this material degrade the hydrogen detection capabilities of a rover based-neutron detector? 2) What is the expected counting rate for a in situ neutron spectrometer? 3) What is the influence of the Martian atmosphere on the hydrogen detection capabilities of a neutron detector system?

Figure 3 shows modeling results for bare  $^3\text{He}$  tubes on the surface and  $^3\text{He}$  tubes attached to a rover when the surface is bombarded by energetic galactic cosmic rays. Figure 3a shows the epithermal neutron counting rate for varying amounts of  $\text{H}_2\text{O}$  in soil buried under a 15 cm thick dry soil layer. As shown, epithermal neutrons are a strong indicator of  $\text{H}_2\text{O}$  content such that increasing amounts of  $\text{H}_2\text{O}$  show a lower epithermal neutron counting rate. Furthermore, the rover mounted tubes show a higher counting rate than bare tubes. For the most part, this is the result of neutrons from the surface being scattered and moderated by the rover material. Finally, compared to earlier results with no atmosphere [3], the absolute counting rates are a factor of 2 – 3 higher with an atmosphere than with no atmosphere. The qualitative counting rate profile, however, is very similar between the atmosphere and non-atmosphere cases.

Figure 3b shows the percentage change in counting rates for both the rover and bare tubes compared to a dry soil case. As in the previous study, rover based tubes show somewhat lower sensitivity to  $\text{H}_2\text{O}$  variations, but the variations are nevertheless significant. For example, when the lower layer has an abundance of 10 wt.%  $\text{H}_2\text{O}$ , the rover based counting rate change is only 8% lower than the bare case (71% signal change for a rover tube compared to a 77% signal change for a bare tube). The rover body, therefore, has a small ef-

fect on the ability of using neutron spectroscopy to measure  $\text{H}_2\text{O}$ .

Finally, we can estimate the amount of time needed for making high precision measurements with good statistics for rover based tubes. For example, if there is a location with 10 wt.%  $\text{H}_2\text{O}$  underlying 15cm of dry soil, the epithermal neutron counting rate is 2.9 counts per second (c/s). To achieve a counting rate uncertainty of 10% takes 35 seconds (where uncertainty is defined as  $1/\sqrt{\text{counts}}$ ); an uncertainty of 5% is achieved in 2.3 minutes, and an uncertainty of 1% is achieved in 58 minutes. These counting rate times are a function of the size of the  $^3\text{He}$  tubes and will scale roughly as the volume of the tubes. Therefore, if smaller tubes are used, the required counting times will be correspondingly longer.



**Figure 3:** (a) Modeled epithermal neutron counting rates as a function of  $\text{H}_2\text{O}$  for a semi-infinite layer buried underneath 15cm of dry soil; and (b) percentage signal change from dry soil. The black symbols show results for  $^3\text{He}$  tubes attached to a rover/lander; the red symbols show results for bare  $^3\text{He}$  tubes on the surface.

**4. Modeling an NS in the Presence of an RTG Power Source.** In order to extend the surface life of a future rover/lander for the upcoming Mars Smart Lan-

der (MSL), it has been stated that the MSL will be powered with a radioactive thermal generator (RTG) [11]. While such a power source will extend the life of the rover mission, the intense radiation environment of an RTG-based MSL also raises questions regarding the NS measurement technique: 1) Will the background radiation from the RTG's be too intense and overwhelm the NS sensors, thereby preventing a measurement of surface hydrogen content? 2) Conversely, is it possible to use the RTG radiation as a source that enables the measurement of the surface hydrogen content?

In order to answer these questions, we have modeled the NS and rover/lander environment in the presence of a Cassini-like RTG power source, which is being considered for the MSL mission [12]. Figure 4 shows the energy dependent neutron flux emitted from such an RTG. The total energy-integrated flux is  $1.2 \times 10^{11}$  n/cm<sup>2</sup> s<sup>-1</sup>. We note that there is also a substantial gamma-ray flux in the vicinity of the RTG. However, we will ignore the gamma-ray component in this study for two reasons: 1) gamma-rays are more easily shielded than neutrons, thereby decreasing their flux at the neutron sensor; 2) <sup>3</sup>He neutron sensors are highly insensitive to gamma-rays [13], therefore reducing the effect of gamma-rays on the neutron measurements.

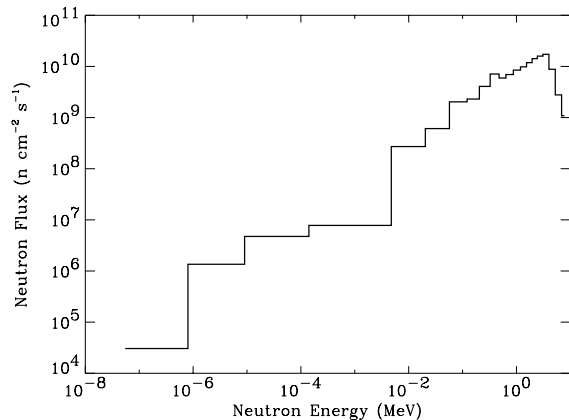


**Figure 4:** Energy dependent neutron flux that is emitted from a Cassini-like RTG being considered for the MSL mission.

Figure 5 shows the modeling results for thermal versus epithermal neutrons for various H<sub>2</sub>O contents and burial depths. Figure 5a shows the results for neutrons produced by galactic cosmic rays (GCR) and Figure 5b shows the results for neutrons produced by an RTG. A number of conclusions from these plots can be made. First, for a given soil composition, H<sub>2</sub>O content and burial depth can be determined with thermal and epithermal neutron measurements for both GCR and RTG produced neutrons. However, the counting rate profiles between the two cases are quite

different. These differences are mainly due to differences in thermal neutron fluxes (see Figure 6). Finally, the counting rates for RTG produced neutrons are much larger than for GCR produced neutrons. For example, for a soil of 10 wt.% H<sub>2</sub>O buried under 15 cm of dry soil, measurements with 1% statistical uncertainty can be obtained in 1 – 2 minutes for RTG produced neutrons compared to ~1 hour for GCR produced neutrons.

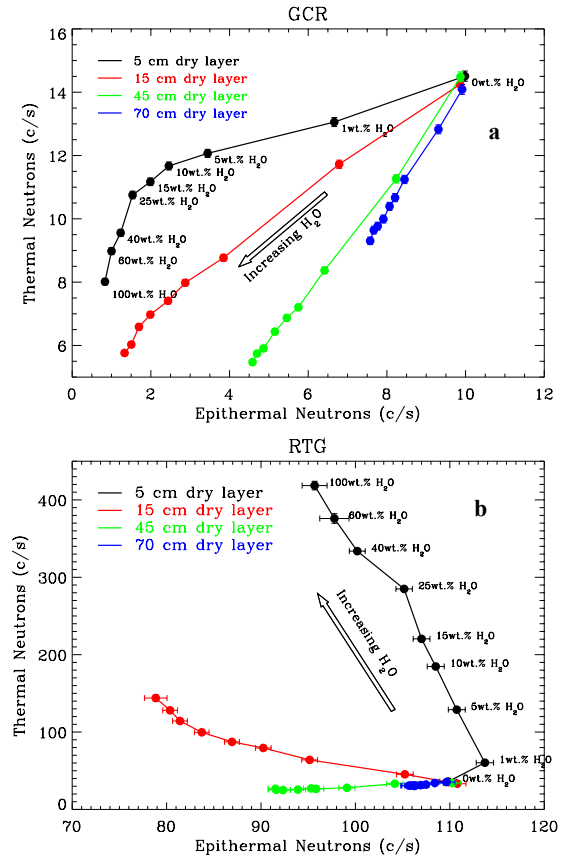


**Figure 5:** Thermal neutrons versus epithermal neutrons for various H<sub>2</sub>O contents and burial depths for both (a) cosmic ray and (b) RTG produced neutrons.

Figure 6 gives more detail regarding the differences in counting rate profiles between the GCR and RTG cases. Figure 6a shows thermal neutrons versus H<sub>2</sub>O content for GCR produced neutrons with both a thin (15 cm) and thick (70 cm) dry layer. As shown, for both thicknesses, the thermal neutrons show a decrease in the counting rate for increasing H<sub>2</sub>O content. In contrast, Figure 6b shows thermal neutrons versus H<sub>2</sub>O content for RTG produced neutrons. Here, for a thin layer, there is a strong increase in thermal neutrons versus H<sub>2</sub>O content; for a thick layer, there is almost no change in thermal neutrons for increasing H<sub>2</sub>O content. RTG produced thermal neutrons are therefore highly

sensitive to near surface H<sub>2</sub>O. This sensitivity is due to the short penetration depth of RTG primary neutrons compared to cosmic rays, and to the large moderation of primary RTG neutrons to thermal energies from the near surface H<sub>2</sub>O.

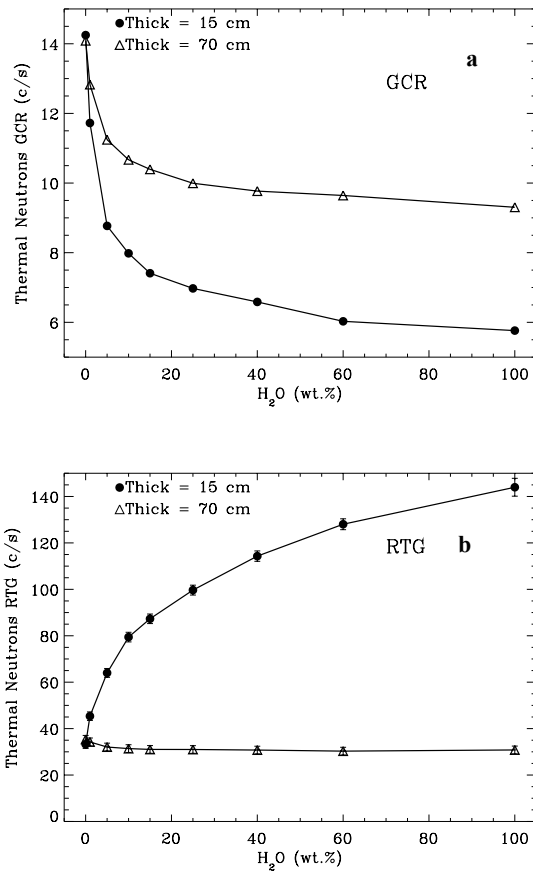


**Figure 6:** Thermal neutrons versus H<sub>2</sub>O content for (a) GCR and (b) RTG produced neutrons.

**5. Summary and Conclusions:** Based on these modeling studies, we can arrive at a number of conclusions. 1) Mounting a NS on a rover/lander increases the neutron counting rate, but does not dramatically decrease the hydrogen detection sensitivity. 2) Water abundance measurements of moderate precision (5 – 10%) can be made in minutes using only galactic cosmic rays as a source of the neutrons. High precision measurements (<1%) can be made in an hour, again only using cosmic rays as the source of the neutrons. 3) Figure 5a shows that even small amounts of H<sub>2</sub>O can be detected even when buried under 70 cm of dry soil. 4) In situ neutron spectroscopy at the surface of Mars is feasible even in the presence of an RTG power source. In fact, RTG-produced neutrons provide a good means of measuring the near-surface H<sub>2</sub>O content with high

counting rates. These high counting rates increase the operational flexibility for a MSL rover by allowing high-precision (<1% statistical uncertainty) to be made in minutes. 5) RTG produced thermal neutrons enable a very sensitive measurement of near surface (5 –15 cm) H<sub>2</sub>O content.

**References:** [1] Feldman et al., *Science*, 297, 75, 2002; [2] Feldman et al., *J. Geophys. Res.*, 105, E2, 4175, 2000; [3] Lawrence et al., *33rd LPSC*, Abstract #1597, 2002; [4] Lawrence et al., *34th LPSC*, Abstract #1763, 2003; [5] Elphic et al., *this conference*, 2003; [6] Feldman et al., *Nuc. Inst. and Meth. A*, 422, 562, 1999; [7] Waters, *MCNPX Users Manual*, LA-UR 02-2607, 2002; [8] Boynton et al., *Science*, 297, 81, 2002; [9] Sevilla, D., JPL, pers. comm., 2002; [10] Bruckner et al., *32nd LPSC*, Abstract #1293, 2001; [11] Hartman, C., NASA Headquarters Briefing, *34th LPSC*, 2003; [12] Jun I., JPL, pers. comm., 2002; [13] Hahn et al., *IEEE Trans. Nuc. Sci.*, submitted, 2002.

**A THREE-DIMENSIONAL PHOTOCHEMICAL-TRANSPORT MODEL OF THE MARTIAN ATMOSPHERE.** F. Lefèvre, *Service d'Aéronomie, CNRS/Univ. Paris 6, 75252 Paris Cedex 05, FRANCE, (franck.lefevre@aero.jussieu.fr)*, S. Lebonnois, F. Forget, *Laboratoire de Météorologie Dynamique, CNRS/Univ. Paris 6, 75252 Paris Cedex 05, FRANCE.*

## Introduction

This paper presents preliminary results of the first three dimensional simulations of the Martian photochemistry. Up to now only one-dimensional models (e.g., [1], [2], [3], [4]) have generally been used to determine the vertical profiles of trace constituents in the Mars atmosphere. These models have been very useful to estimate the globally averaged distribution of chemical species as a function of height, and have emphasized the role of water vapor to explain the classical problem of the stability of the Martian CO<sub>2</sub> atmosphere. However, one-dimensional models cannot represent the dramatic meridional variations of the distribution of trace species caused by the usually strong pole-to-pole gradient of atmospheric temperature and water vapor. The effects of the meridional transport of chemical species are also ignored, and a highly uncertain eddy diffusion coefficient is used to represent the vertical transport and mixing. The only two-dimensional simulations published by *Moreau et al.* [5] provided a better description of the interaction between dynamics, radiation, and chemistry, although the model did not include a consistent representation of the water cycle nor a treatment of the dynamics near the surface where the topographical effects are important.

In the present work, a new chemical model of the Martian atmosphere has been coupled to the general circulation model (GCM) developed at LMD for the last 10 years [6]. Trace constituents are transported by the three-dimensional winds and convective processes calculated by the GCM. Their chemical evolution is computed by the chemical module as a function of the pressure and temperature fields, solar zenith angle, heliocentric distance, and the amount of water vapor, which is also affected by condensation and sublimation processes. The evolution of the chemical species is therefore computed in three dimensions over the Martian globe and is fully interactive with the GCM dynamics, radiation field, and water cycle. Presently, we use a rather low horizontal resolution ( $11.25^\circ \times 7.5^\circ$ ), with 32 vertical layers, from the surface up to 120 km.

## The photochemical module

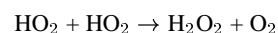
The first version the chemical model used in the present work describes the chemistry of oxygen, hydrogen, and CO. Eleven species are taken into account and individually transported by the coupled model (O, O(<sup>1</sup>D), O<sub>2</sub>, O<sub>3</sub>, H, OH, HO<sub>2</sub>, H<sub>2</sub>O<sub>2</sub>, H<sub>2</sub>, H<sub>2</sub>O, CO). Photolysis rates are calculated from the model of *Madronich and Flocke* [7] adapted to the Martian conditions. Calculations are performed off-line at high spectral resolution (0.1 nm), in spherical geometry, and take into account the vertical distribution of CO<sub>2</sub>, H<sub>2</sub>O, O<sub>2</sub>, and O<sub>3</sub> to determine the atmospheric opacity in the UV region. The most recent absorption cross-section datasets were used and include temperature dependence for CO<sub>2</sub>, O<sub>2</sub>, O<sub>3</sub>, and H<sub>2</sub>O<sub>2</sub>. Once calculated

from 0 to 95° the vertical profiles of photolysis rates are stored in a three-dimensional lookup table as a function of the solar zenith angle and the slant columns of CO<sub>2</sub> and O<sub>3</sub>. At each chemical time step of the coupled model, the actual photolysis rate for each sunlit gridpoint is retrieved by interpolating the value inside the lookup table. Gas-phase reaction rate coefficients were in general taken from *Sander et al.* [8]. Rate coefficients of three-body reactions are increased by a factor of 2.5 to account for the higher efficiency of CO<sub>2</sub> as a third body in comparison with N<sub>2</sub> and O<sub>2</sub>. Temperature and pressure values used to compute the reaction rates are provided for each grid point by the GCM. In order to reduce the computational cost of the integration, a family approach was adopted (O<sub>x</sub> = O + O<sub>3</sub>; HO<sub>x</sub> = H + OH + HO<sub>2</sub>), and photochemical equilibrium is assumed for O<sub>3</sub>, O(<sup>1</sup>D), OH, and HO<sub>2</sub>. The chemical evolution of long-lived species (O<sub>2</sub>, H<sub>2</sub>, H<sub>2</sub>O, H<sub>2</sub>O<sub>2</sub> and CO) and chemical families is solved by the iterative method described by *Shimazaki* [9].

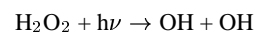
## Hydrogen peroxyde cycle

Hydrogen peroxyde, H<sub>2</sub>O<sub>2</sub>, is an important product of the odd-hydrogen chemistry in the Martian atmosphere. Being a very strong oxidizing species, it has been suggested that H<sub>2</sub>O<sub>2</sub> might be responsible for the absence of organic compounds on the surface [10]. In addition to the large intensities of several of its fundamental bands in the infrared, H<sub>2</sub>O<sub>2</sub> is predicted by the models to be the most abundant HO<sub>x</sub> species near the surface, and should therefore be certainly less difficult to measure remotely than OH or HO<sub>2</sub>. However, observations have so far failed to detect H<sub>2</sub>O<sub>2</sub> in the Martian atmosphere. Recently *Encrenaz et al.* [11] could derive from their observations an upper limit for the H<sub>2</sub>O<sub>2</sub> vertical column of  $9 \times 10^{14}$  to  $1.2 \times 10^{15}$  cm<sup>-2</sup> which appears to be considerably lower than the estimates of previous 1D model simulations. We will report here preliminary results of the first 3D simulations of hydrogen peroxyde on Mars, and will compare the obtained values to the upper limit given by *Encrenaz et al.* [11].

Atmospheric hydrogen peroxyde is mainly formed by the reaction involving two HO<sub>2</sub> radicals:



HO<sub>2</sub> is an indirect product of the H<sub>2</sub>O photolysis and therefore a strong correlation is expected between the water vapor and hydrogen peroxyde abundances. The main H<sub>2</sub>O<sub>2</sub> loss mechanism occurs by photolysis:



with a characteristic time of about 6 hours in the lower atmosphere. H<sub>2</sub>O<sub>2</sub> has therefore a much longer lifetime than

H, OH, and HO<sub>2</sub>, and has no loss mechanism at night. This implies that photochemical equilibrium cannot be assumed in a model including the diurnal cycle. This species is individually integrated and transported in our model. Another important process included in the model is the condensation of H<sub>2</sub>O<sub>2</sub>, which may occur in the regions of very low temperatures. The calculated number densities are constrained to lie at or below the local saturation number density given from the expression by Lindner [12].

Fig. 1 displays the seasonal evolution of the H<sub>2</sub>O<sub>2</sub> and H<sub>2</sub>O column density zonal means. As expected hydrogen peroxide is clearly correlated with the amount of water vapor available to produce HO<sub>x</sub> radicals by photolysis. A strong seasonal variability of H<sub>2</sub>O<sub>2</sub> is calculated by the model: the column abundance varies by a factor larger than 10 at high latitudes and a factor of about 3 at low latitudes, in phase with the water vapor changes caused by condensation, sublimation, and transport processes. Interestingly the maximum amount of H<sub>2</sub>O<sub>2</sub> ( $1.8 \times 10^{16}$  mol cm<sup>-2</sup> in late fall at 20N) does not correspond to the absolute maximum of water vapor, reached at the end of northern spring at high latitudes (about 100 precipitable microns), in good agreement with the observations. Examination of the evolution of the vertical distribution of H<sub>2</sub>O at the Equator (Fig. 3) reveals that the hydrogen peroxide maximum calculated near aphelion is a consequence of the variation of the saturation altitude of water vapor, leading to the production of large amounts of HO<sub>x</sub> radicals over a domain of altitude almost twice as high as during the rest of the year.

Fig. 2 shows the calculated H<sub>2</sub>O<sub>2</sub> vertical column at the same solar longitude ( $L_s = 112$ ) when *Encrenaz et al.* [11] derived their upper limit of  $9 \times 10^{14}$  to  $1.2 \times 10^{15}$  cm<sup>-2</sup> in the northern hemisphere. The model distribution shows a strong hemispheric contrast, linked to the abundance of water vapor which is maximum in the northern hemisphere at this time of the year. The topography also plays a significant role in the longitudinal and latitudinal variations of H<sub>2</sub>O<sub>2</sub>, as shown by the absolute maximum reached in the Utopia Planitia basin, whereas lower amounts are calculated at the same latitude over regions of higher elevation. Overall the quantities given by the model are larger than the upper limit by a factor 5 to 15. Several possible reasons for this overestimation are currently under investigation: the large uncertainties existing on crucial processes such as the H<sub>2</sub>O photolysis in the Martian conditions, the choice of the rate constants of some key reactions involving OH or HO<sub>2</sub>, as well as the possible loss of HO<sub>x</sub> radicals to the surface of Mars. The results of sensitivity studies on these different parameters will be presented during the conference.

### Ozone cycle

Atomic oxygen is produced in Mars atmosphere through the photodissociation of CO<sub>2</sub>. It recombines to form molecular oxygen, and then ozone. Ozone is lost through photolysis, and through the reaction with HO<sub>x</sub> radicals (OH, HO<sub>2</sub>). Therefore, it is expected to be in strong anticorrelation with water vapor. As seen previously, it seems that our model overpredicts the

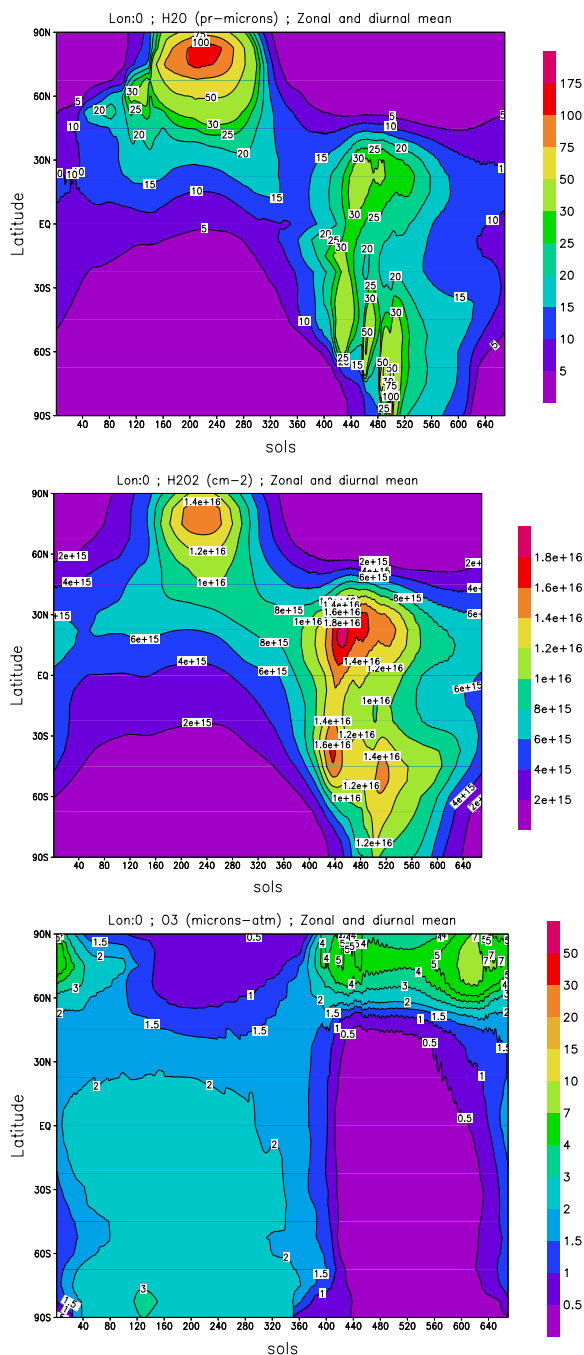


Figure 1: Seasonal cycles of water, hydrogen peroxide and ozone: zonal and diurnal mean column densities as a function of latitude and days counted from northern spring equinox.

abundance of these radicals. It is therefore not surprising that when we compare the distribution of ozone obtained in the model with available observations of ozone column densities ([13], [14], [15]), it seems that our model underpredicts ozone concentrations by a factor 2 to 5. Nevertheless, this three

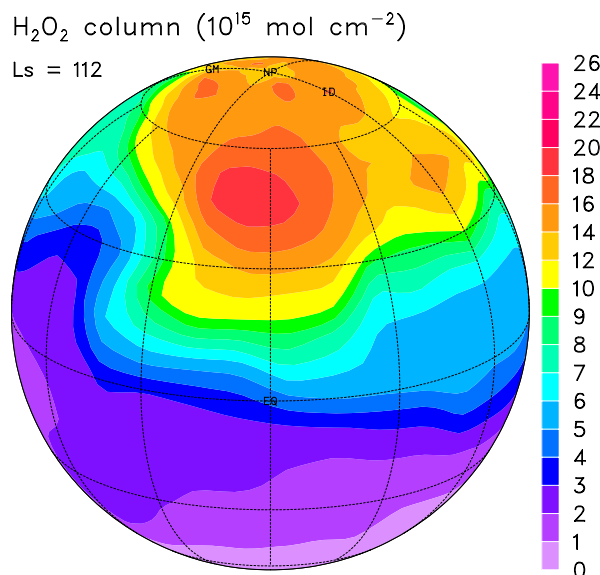


Figure 2: instantaneous  $\text{H}_2\text{O}_2$  column ( $10^{15}$  molecule  $\text{cm}^{-2}$ ) distribution calculated at  $L_s = 112$ . The observer is facing the meridian at  $120^\circ\text{W}$  longitude (local time = 8PM).

dimensional model allows a close study of the seasonal and diurnal variations of ozone and other related chemical species, in relation with the water cycle. We will develop here some first examples of the possibilities of this tool.

The seasonal evolution of the ozone column density is shown in Fig. 1, together with water vapor and hydrogen peroxide. The anticorrelation is clear, but the asymmetry between the southern and northern winters must be noted: related anticorrelations between ozone and water vapor are strongest for northern winter. This asymmetry is linked to the hygropause altitude, which varies significantly as a function of season, in correlation with the variations of the distance to the sun (aphelion around southern winter solstice, and perihelion around northern winter solstice) and with the dust load of the atmosphere (which has an impact on temperature). These variations are shown at equator in Fig. 3, for water vapor and ozone mixing ratios.

The diurnal cycle of ozone also displays remarkable seasonal ( $L_s$ ) variations. To illustrate this, Fig. 4 shows maps of ozone column density at two opposite seasons: southern winter and northern winter solstices. In southern winter, ozone abundance is larger on the night side than on the day side, and therefore exhibits a strong diurnal cycle, with a clear footprint of the terminator. At the opposite season, the behavior is very different. The ozone abundance is much lower on almost all the planet, except around the winter pole, and no diurnal cycle is visible. These differences are linked to the global abundance of the  $\text{HO}_x$  radicals, in relation with the water vapor seasonal cycle. In the Northern winter polar vortex, condensation of water vapor on the surface suppresses the source of  $\text{HO}_x$ , leading to large  $\text{O}_3$  maximum in good qualitative agreement with the observations. At all other latitudes, the increase

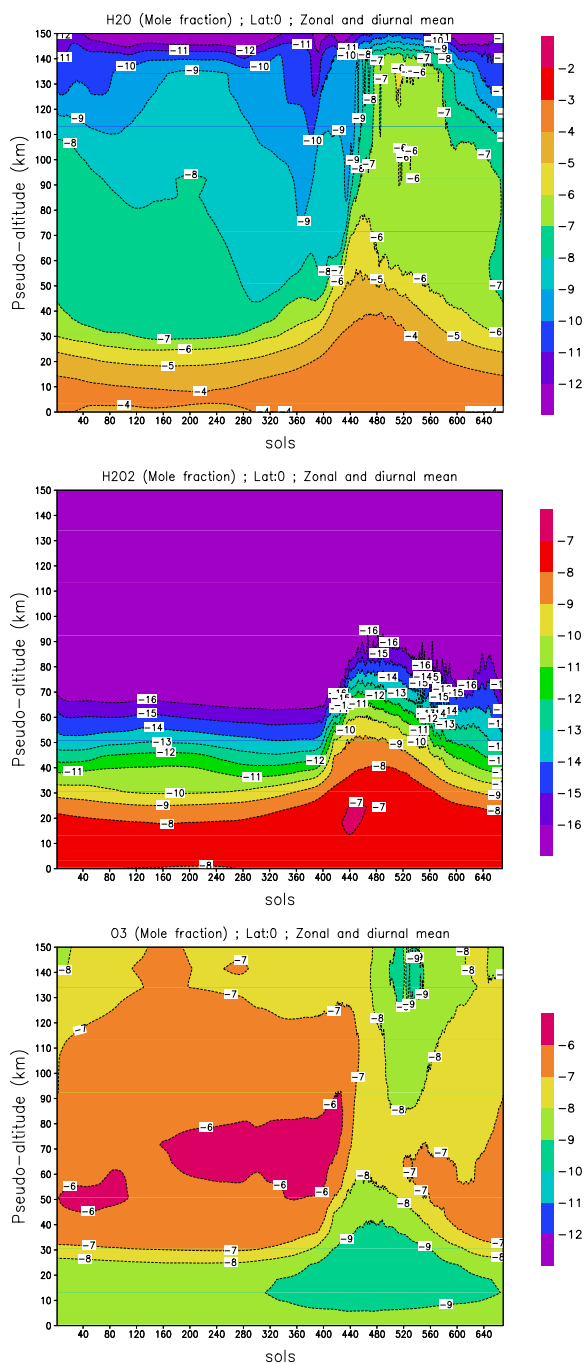


Figure 3: Seasonal variations of water vapor, hydrogen peroxide and ozone at equator: zonal and diurnal mean mixing ratios (log) as a function of altitude and days counted from northern spring equinox.

of water vapor and the uprise of the hygropause calculated by the model near perihelion is responsible for the increased loss of  $\text{O}_x$  species by the  $\text{HO}_x$  radicals and the disappearance of

the ozone diurnal cycle.

### Conclusion

We have developed the first three-dimensional photochemical-transport model of the Martian atmosphere. A photochemical module including 11 species and 38 photochemical reactions has been coupled to the LMD-GCM. Despite our use of the most recent photochemical data, the model appears to overestimate the abundance of hydrogen peroxy and in the same time, to underestimate the observed ozone column density. These biases suggest that the amount of  $\text{HO}_x$  is too large in the model or/and the  $\text{HO}_x$  chemistry is too efficient at destroying odd oxygen. We plan to investigate carefully the reasons for this discrepancy, by analyzing the various sources of uncertainties in the currently recommended reaction rate coefficients and in our knowledge of absorption cross-sections of  $\text{CO}_2$  and  $\text{H}_2\text{O}$  in the Mars conditions.

Nevertheless this new generation of model allows detailed studies of the spatial, seasonal and diurnal behavior of the composition of the Martian atmosphere. It will be applied to the analysis of the data of the SPICAM instrument onboard Mars-Express, for which stringent tests of our quantitative understanding of the Martian photochemistry will be possible by the comparison of the model results to the simultaneous observations of ozone and water vapor.

In the following months, we will improve the model along the following lines:

- the model resolution will be increased,
- the transport scheme for the water ice clouds developed for the LMD-GCM by Franck Montmessin will be taken into account to improve the water cycle,
- dust will be included in the UV radiative transfer calculations,
- nitrogen compounds will be added,
- interactions with the surface will be investigated,
- our photochemical model will be coupled with the version of the LMD-GCM extended to the thermosphere, developed by Monica Angelats-i-Coll.

### References

[1] Parkinson, T.D., and D.M. Hunten, *J. Atmos. Sci.*, 29, 1380-1390, 1972. [2] McElroy, M.B., and T.M. Donahue,

*Science*, 177, 986-988, 1972. [3] Krasnopolsky, V.A., *Icarus*, 101, 313-332, 1993. [4] Nair, H., et al., *Icarus*, 111, 124-150, 1994. [5] Moreau, D., L.W. Esposito, and G. Brasseur, *J. Geophys. Res.*, 96, 7933-7945, 1991. [6] Forget, F., et al., *J. Geophys. Res.*, 104, 24155-24176, 1999. [7] Madronich, S., and S. Flocke, in *Handbook of Environmental Chemistry* (P. Boule, ed.), pp. 1-26, Springer-Verlag, Heidelberg, 1998. [8] Sander, S.P., et al., *JPL publication 02-25*, 2003. [9] Shimazaki, T., *Terra Scientific Publishing*, Tokyo, 1985. [10] Klein, H.P., N.H. Horowitz, and K. Biemann, in *Mars*, University of Arizona Press, 1992. [11] Encrenaz, T., et al., *Astronomy and Astrophysics*, 396, 1037-1044, 2002. [12] Lindner, B.L., *Planet Space Sci.*, 36, 125-144, 1988. [13] Espenak, F., et al., *Icarus*, 92, 252-262, 1991. [14] Clancy, R.T., M.J. Wolff, and P.B. James, *Icarus*, 138, 49-63, 1999. [15] Novak, R.E., et al., *Icarus*, 158, 14-23, 2002.

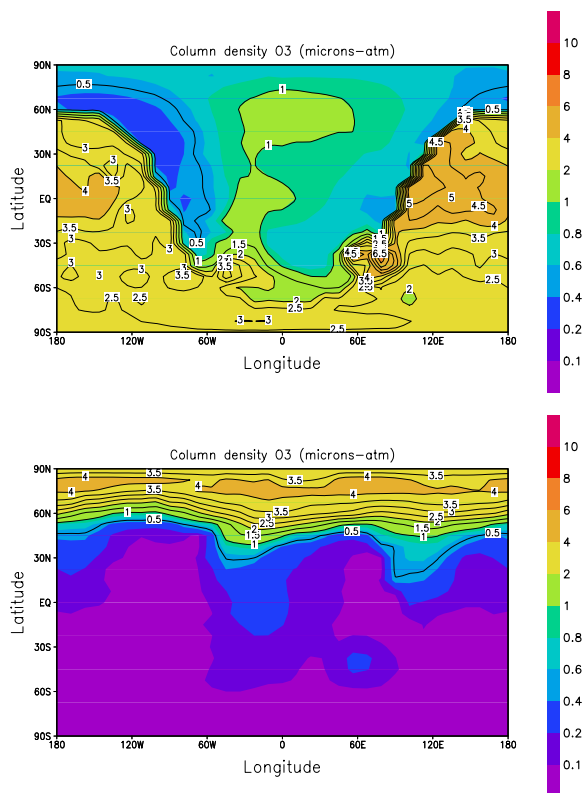


Figure 4: Instantaneous maps of column ozone (micron-atmosphere) for southern winter solstice (top) and northern winter solstice (bottom).

**WIND AND WATER AT THE SURFACE OF MARS.** C. B. Leovy<sup>1</sup> and J. C. Armstrong<sup>2</sup>, <sup>1</sup>Dept. of Atmospheric Sciences, Box 351640, University of Washington, Seattle WA 98195 (conway@atmos.washington.edu), <sup>2</sup>Dept. of Astronomy, Box 351580, University of Washington, Seattle WA 98195.

**Introduction:** It is widely assumed that the surface of Mars has been exposed to massive flows of liquid water. These flows are supposed to have taken place both near the end of the early intense bombardment period under a warm wet climate regime and in massive outburst floods, mainly around the periphery of large low latitude volcanic complexes such as Tharsis. However, these scenarios do not adequately account for several lines of evidence that point toward a smaller role for flowing water and a larger role for wind in surface modification. With the aim of broadening the terms of discussion of martian surface history, these lines of evidence are reviewed and interpreted here.

**Thermal Inertia Distribution:** Over a wide range of scales, thermal inertia is negatively correlated with elevation. Since very high thermal inertia corresponds to high rock abundances or bedrock, and very low thermal inertia corresponds to fine dust particles, this relationship indicates that fine particles have been systematically transported from low areas to high areas, in marked contrast to the usual direction of fine particle transport on Earth. This up-gradient sediment transport can be accounted for only by wind action.

**Atmospheric Circulation Models and Dust Storms:** General circulation models predict a distribution of potential erosion and deposition that is remarkably consistent with the distribution of thermal inertia on large scales. The predicted wind erosion pattern also coincides well with the observed pattern of dust storm occurrences. Mesoscale models of atmospheric flows show a strong tendency for channeling of strong winds by topography, in agreement with the observed association of thermal inertia with topography on small scales. General circulation models also show that the spatial distribution of erosion and deposition is stable with respect to orbital parameter variations and surface pressure changes. These models also predict that erosion rate would have been much higher than at present with as little as 2-4 times the present mean surface pressure.

**Surface Geomorphology:** Very low areas such as the northern plains and the floor of Hellas have unique surface features suggestive of very rapid resurfacing, and of long-term sedimentation and erosion. These include paucity of small craters (diameters < several hundred meters), highly degraded large craters and "ghost" craters with diameters > 100km. These features are widely assumed to be due primarily to sedimentation, but, in view of the evidence cited above, it is likely that erosion is a more important factor than sedimentation for the observed degradation of craters at all scales in the northern plains and Hellas.

Another important piece of evidence is the observation of widespread surface exposures of sedimentary layers. These layers indicate past sub-aqueous or sub-aerial sedimentation. It is equally significant that many of these layer remnants appear to be undergoing rapid erosion in the present climate regime. Only wind can account for this erosion. The widespread occurrence of partially eroded sedimentary layers also indicates that burial and exhumation of surfaces is a common phenomenon that obscures surface modification processes and sequences.

**Greenhouse Models:** The most recent and complete greenhouse models have not been able to produce enough warming of the surface to account for a warm wet early climate regime with any plausible combination of greenhouse gases.

**Surface Mineralogy:** No large deposits of carbonates that could correspond to the residue of an early dense carbon dioxide atmosphere have been identified. It is sometimes assumed that such deposits could be buried beneath the northern plains, but in view of the evidence cited above that these plains are primarily erosional rather than depositional surfaces, this is unlikely. Crystalline hematite indicative of weathering by liquid water has been identified, but only in a few relatively small areas.

**Implications:** Taken together, these lines of evidence suggest that the surface of Mars has been systematically and massively modified by wind erosion and dust redistribution over geological time. They cast doubt on interpretations of surface geomorphology that fail to take wind modification of the surface into account. These interpretations include deep sedimentary layers in the northern plains, lakebeds in crater floors and basins, and fluvial origins of some channel features that may have been streamlined as well as widened and deepened by wind action.

Wind action, by itself, does not seem capable of accounting for the initial formation as distinct from the subsequent modification of channel features, and it does not seem capable of accounting for the geomorphology of gully features that may be due to the localized release of water from near-surface ice. However, the observational evidence for massive wind modification of the surface and the theoretical and observational evidence against an early warm climate regime implies that Mars may have been cold and dry with only modest amounts of water ice (a few tens of meters) available at the surface since early in the Noachian period.

## NON-EQUILIBRIUM THERMODYNAMIC CHEMISTRY AND THE COMPOSITION OF THE ATMOSPHERE OF MARS

J. S. Levine<sup>1</sup> and M. E. Summers<sup>2</sup>

<sup>1</sup>NASA Langley Research Center, Hampton, VA 23681, joel.s.levine@nasa.gov

<sup>2</sup>School of Computational Sciences and Dept. of Physics and Astronomy, George Mason University, Fairfax, VA 22030, msummers@gmu.edu

A high priority objective of the Mars Exploration Program [1] is to “Determine if life exists today” (MEPAG Goal I, Objective A). The measurement of gases of biogenic origin may be an approach to detect the presence of microbial life on the surface or subsurface of Mars. Chemical thermodynamic calculations indicate that on both Earth and Mars, certain gases should exist in extremely low concentrations, if at all [2]. Microbial metabolic activity is an important non-equilibrium chemistry process on Earth, and if microbial life exists on Mars, may be an important non-equilibrium chemistry process on Mars. The non-equilibrium chemistry of the atmosphere of Mars is discussed in this paper.

Chemical thermodynamic equilibrium calculations indicate that certain trace gases in the Earth’s atmosphere, such as methane (CH<sub>4</sub>), ammonia (NH<sub>3</sub>), nitrous oxide (N<sub>2</sub>O), and carbon disulfide (CS<sub>2</sub>) should be at atmospheric concentrations many orders of magnitude below their actual atmospheric concentrations (Table 1). The role of microbial metabolic activity for establishing this chemical non-equilibrium is well known [3,4,5].

Chemical thermodynamic equilibrium calculations for certain trace gases in the atmosphere of Mars have been performed. As input parameters for these calculations, the following atmospheric composition was used: carbon dioxide (CO<sub>2</sub>): 95.32%, nitrogen (N<sub>2</sub>): 2.7%, argon (Ar): 1.6%, oxygen (O<sub>2</sub>): 0.13%, carbon monoxide (CO): 0.07% [6]. The mean atmospheric surface pressure was assumed to be 6.4 mb and a surface temperature range from

148K (polar winter) to 290K (southern summer) was assumed [6]. The calculated equilibrium concentration of methane, ammonia, and nitrous oxide in the atmosphere of Mars is summarized in Table 2.

**Table 1. Some Trace Gases in the Earth’s Atmosphere**

<u>Gas</u>	<u>Thermo-Dynamic Equilibrium (Mole Fraction)</u>	<u>Measured Concentration</u>	<u>Atmospheric Enhancement</u>
Methane (CH <sub>4</sub> )	10 <sup>-145</sup>	1.7 x 10 <sup>-6</sup>	10 <sup>139</sup>
Ammonia (NH <sub>3</sub> )	2 x 10 <sup>-60</sup>	10 <sup>-10</sup>	10 <sup>50</sup>
Nitrous oxide (N <sub>2</sub> O)	2 x 10 <sup>-19</sup>	3 x 10 <sup>-7</sup>	10 <sup>12</sup>
Carbon disulfide (CS <sub>2</sub> )	0	10 <sup>-11</sup>	

**Table 2. Calculated Trace Gases in the Atmosphere of Mars Based on Thermodynamic Equilibrium Calculations (Unit: Mixing Ratio)**

<u>Gas</u>	<u>T = 100K</u>	<u>T = 200K</u>	<u>T = 300K</u>
Methane (CH <sub>4</sub> )	<10 <sup>-100</sup>	<10 <sup>-100</sup>	<10 <sup>-100</sup>
Ammonia (NH <sub>3</sub> )	<10 <sup>-100</sup>	2 x 10 <sup>-89</sup>	4 x 10 <sup>-62</sup>
Nitrous oxide (N <sub>2</sub> O)	6 x 10 <sup>-54</sup>	4 x 10 <sup>-30</sup>	5 x 10 <sup>-23</sup>

Sulfur on the surface of Mars may prove to be an interesting raw material for microbial appetites. Viking lander measurements found that the surface sulfur concentrations at both landing sites ranged from 10 to 100 times higher

than in the terrestrial crust. The source of sulfur on Mars is believed to be volcanic emissions in the form of sulfur dioxide (SO<sub>2</sub>). Microbial communities on Mars, if they exist, could utilize the widespread and readily available surface sulfur and produce atmospheric reduced sulfur species. Chemical thermodynamic equilibrium calculations indicate that reduced sulfur species should not exist in the atmosphere of Mars in detectable levels in the absence of microbial metabolic activity. Chemical thermodynamic equilibrium calculations of reduced sulfur species in the atmosphere of Mars are summarized in Table 3. These calculations assume an atmospheric sulfur dioxide partial pressure of 10<sup>-9</sup> atm.

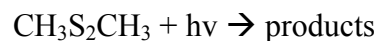
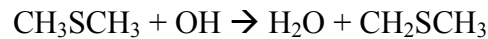
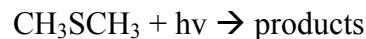
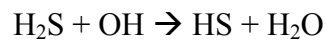
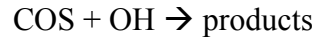
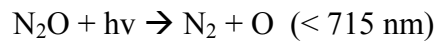
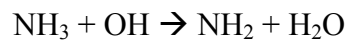
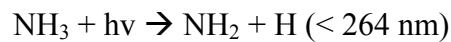
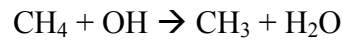
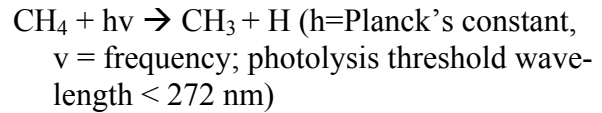
**Table 3. Trace Sulfur Gases in the Atmosphere of Mars Based on Thermodynamic Equilibrium Calculations (In terms of partial pressure of sulfur species to partial pressure of sulfur dioxide, assumed to be 10<sup>-9</sup> atm, for T = 200K)**

<u>Gas</u>	<u>Partial Pressure of Gas/ Partial Pressure of SO<sub>2</sub></u>
Carbonyl sulfide (COS)	10 <sup>-83</sup>
Hydrogen sulfide (H <sub>2</sub> S)	10 <sup>-84</sup>
Carbon disulfide (CS <sub>2</sub> )	10 <sup>-180</sup>
Methane thiol (CH <sub>3</sub> SH)	10 <sup>-197</sup>
Dimethyl sulfide (CH <sub>3</sub> SCH <sub>3</sub> )	10 <sup>-307</sup>
Dimethyl disulfide (CH <sub>3</sub> S <sub>2</sub> CH <sub>3</sub> )	10 <sup>-364</sup>

Based on thermodynamic equilibrium calculations, the carbon, nitrogen, and sulfur species in Tables 2 and 3 should be present in very small concentrations and they are expected to be destroyed efficiently and rapidly by photochemical and chemical processes. These species are destroyed by photolysis by both solar ultraviolet radiation and by chemical reaction with the hydroxyl radical (OH), which is formed by the photolysis of water vapor (H<sub>2</sub>O) (except for nitrous oxide (N<sub>2</sub>O), which is destroyed via reaction with excited atomic

oxygen (O(<sup>1</sup>D))), rather than by OH). The photochemical processes that lead to the destruction of these gases are summarized in Table 3.

**Table 4. Photochemical and Chemical Processes that Destroy the Gases in Tables 2 and 3 [7, 8,9].**



The lifetime of these gases with respect to chemical destruction by the hydroxyl radical (OH) may be calculated using temperature-dependent reaction rates given in [8]. For these calculations, an atmospheric temperature of 200K and a surface OH number density of 1 x 10<sup>5</sup> cm<sup>-3</sup> [10] were assumed. The calcu-

lated lifetime against destruction by reaction with the hydroxyl radical for some of these species is very short, i.e., dimethyl disulfide: 14 days, dimethyl sulfide: 35 days, hydrogen sulfide: 3 months. Given a vertical eddy mixing timescale on the order of 3 months near the surface of Mars and a horizontal transport timescale on the order of several days [9], these gases will not diffuse far from their location of origin before they are destroyed via reaction with the hydroxyl radical. It is important to remember that these very short atmospheric lifetimes are only based on reaction with the hydroxyl radical and do not include the effect of photolysis by solar ultraviolet radiation on the lifetimes of these species.

Assuming the presence of gases of biogenic origin in the atmosphere of Mars, the very short atmospheric lifetime of these gases and their possible non-uniform source, most likely associated with surface and/or subsurface sites of liquid water, suggest their detection is a very difficult and challenging measurement problem. A mass spectrometer on a powered and controlled airplane flying 1 to 2 kilometers above the surface of Mars and capable of traversing regional scale distances over potential water sites, is an ideal platform to search for the presence of non-equilibrium gases resulting from microbial metabolic activity in the atmosphere of Mars.

### References

- [1] Greeley, R. (Editor), 2001: Mars Exploration Program Scientific Goals, Objectives, Investigations, and Priorities, 31 pages.
- [2] Levine, J. S., C. P. Rinsland, W. L. Chameides, P. J. Boston, and P. Brimblecombe, 1989: Trace Gases in the Atmosphere of Mars: An Indicator of Microbial Life. The Case for Mars III: Strategies for Exploration-Technical (C. Stoker, Editor), American Astronomical Society, San Diego, CA, 277-282.
- [3] Lovelock, J. E. and L. Margulis, 1974: Homeostatic Tendencies of the Earth's Atmosphere. Origins of Life, 5, 93-103.
- [4] Margulis, L. and J. E. Lovelock, 1974: Biological Modulation of the Earth's Atmosphere. Icarus, 21, 471-489.
- [5] Margulis, L. and J. E. Lovelock, 1978: The Biota as Ancient and Modern Modulator of the Earth's Atmosphere. Pure and Applied Geophysics, 116, 239-243.
- [6] Barth, C. A., 1985: The Photochemistry of the Atmosphere of Mars. The Photochemistry of Atmospheres: Earth, The Other Planets, and Comets. Academic Press, Inc., San Diego,, 337-392.
- [7] Levine, J. S. (Editor), 1985: The Photochemistry of Atmospheres: Earth, The Other Planets, and Comets. Academic Press, Inc., San Diego, CA, 518 pages.
- [8] DeMore, W. B., S. P. Sander, D. M. Golden, R. F. Hampson, M. J. Kurylo, C. J. Howard, A. R. Ravishankara, C. E. Kolb, and M. J. Molina, 1992: Chemical Kinetics and Photochemical Data for Use in Stratospheric Modeling. JPL Publication 92-20, 239 pages.
- [9] Summers, M. E., B. J. Lieb, E. Chapman, and Y. L. Yung, 2002. Atmospheric Biomarkers of Subsurface Life on Mars. Geophysical Research Letters, 29.
- [10] Yung, Y. L. and W. B. DeMore, 1999: Photochemistry of Planetary Atmospheres. Oxford University Press, New York, 456 pages.

**4-D MODEL OF CO<sub>2</sub> DEPOSITION AT NORTH AND SOUTH OF MARS FROM HEND/ODYSSEY AND MOLA/MGS.** M.L. Litvak<sup>1</sup>, I.G. Mitrofanov<sup>1</sup>, A.S. Kozyrev<sup>1</sup>, A.B. Sanin<sup>1</sup>, V. Tretyakov<sup>1</sup>, D.E. Smith<sup>2</sup>, M.T. Zuber<sup>2,3</sup>, W.V. Boynton<sup>4</sup>, D.K. Hamara<sup>4</sup>, C. Shinohara<sup>4</sup>, R. S. Saunders<sup>5</sup>, D. Drake<sup>6</sup>, <sup>1</sup>Space Research Institute, RAS, Moscow, 117997, Russia, max@cgrsmx.iki.rssi.ru, <sup>2</sup>Laboratory for Terrestrial Physics NASA/Goddard Space Flight Center, MD, 20771, USA, <sup>3</sup>Massachusetts Institute of Technology, Cambridge, MA, 02139-4307, USA, <sup>4</sup>University of Arizona, Tucson, AZ 85721, USA, <sup>5</sup>Jet Propulsion Laboratory, Pasadena, CA 91109, USA, <sup>6</sup>Lansce 3, Los Alamos Nat'l Lab. Los Alamos, NM and TechSource Inc, Santa Fe, NM 87594, USA.

**Introduction:** The first 1.5 year of neutron mapping measurements onboard Mars Odyssey spacecraft are presented based on High Energy Neutron Detector (HEND) observations. HEND instrument is a part of GRS suite responsible for registration of epithermal and fast neutrons originating in Mars subsurface layer [4,6]. The scattering of fast neutrons in Mars surface caused by primary cosmic rays is strongly sensitive to presence of hydrogen atoms. Even several percents of subsurface water significantly depress epithermal and fast neutron flux [1,2]. It turns orbit neutron spectroscopy into one of most efficient methods for finding distribution of subsurface water.

The Mars Odyssey observations revealed huge water-ice regions above 60N and 60S latitudes[3-6]. It was founded that distribution of subsurface water has layered structure at these regions. It is thought that more than 50% wt water ice covered by relatively dry layer with different thickness[6,9].

The mentioned South and North areas are highly affected by seasonal CO<sub>2</sub> global circulation process. Thus the CO<sub>2</sub> snow depth varied from tens of cm up to ~1m at the latitudes above 60 degrees [7]. Taking into account that maximal sensitivity of neutrons measurements happened at depths less then 2-3 m one may expect significant variations of neutron signal trough martian seasons. It occurs because CO<sub>2</sub> frost hides upper surface layer from the orbit observations. The first search of seasonal effects in neutron data reveals that possible variation of neutron flux between summer and winter time may vary from several percents at 55<sup>0</sup>-60<sup>0</sup> latitudes up to several times for near polar regions[8,9]. In this study we used more large dataset gathered for the first 1.5 year successful operation of Mars Odyssey mission. It covered time period from late winter up to early fall in Northern hemisphere. It gives the possibility to follow the history of sublimation process of CO<sub>2</sub> frost on the North and its accumulation on the South.

**Instrument:** HEND consists of four detectors to provide measurements of neutron signal from red planet in broad energy range. Three proportional counters coated by different thickness of moderator have maximal efficiency in 1eV- 1keV, 10eV-100keV and 10ev - 1meV energy ranges correspondingly. The organic

scintillator created with using stilben crystal guarantee registrations of very energetic neutrons from 1MeV up to 10 MeV. The spectral shape of signal from this detector is measured with 16-channels resolution which allow to select high energy neutrons with energy more then several MeV for farther analysis. There is direct correspondence between energy of registered neutron and depth where it was produced. The production rate of fast neutrons has maximum at depths less than tens of centimeters while the epithermal neutrons originate in layer placed 1-3 m below the surface. Combining measurements in proportional counters with counts accumulated in different parts of fast neutron spectra measured in stilben detector one may reconstruct the water abundance distribution at different depths starting from thin subsurface layer and going down to several meters depths.

**Data analysis:** Using this approach we tried to create simple model to describe layered structure of regolith. At first step the summer measurements of Mars surface on South and North regions were extracted from full set of data. It helps to split the task of finding subsurface water distribution from task of measuring thickness of CO<sub>2</sub> frost. In this study we restrict ourselves only by studying regions near Mars poles above 60 degrees for each hemisphere. It was done because the main goal of this research to look at evolution of CO<sub>2</sub> deposits at different near pole areas with time. Deposition of CO<sub>2</sub> below these latitudes is either absent or so thin that counting statistic cannot provide reliable results. More detail analysis of equatorial regions where presence of water was founded surprisingly high will be considered in other presentations[10].

The surfaces of North and South regions were divided into the network of pixels with 5x5 degree. Each pixel was treated independently in terms of estimation the best parameters of regolith model in given pixel. This choice provides the appropriate space resolution from one side and the reliable statistic (>10 sigmas for each pixel) from another one.

For describing Mars soil we suggest to use two-layers model. It consists of upper relative dry(<3% wt H<sub>2</sub>O) layer with variable thickness and bottom semi-infinite ice-rich (>20% wt H<sub>2</sub>O) layer. Applying the fitting procedure to the real neutron data in wide en-

ergy range the best fit parameters have been estimated for this type of model for each selected pixel.

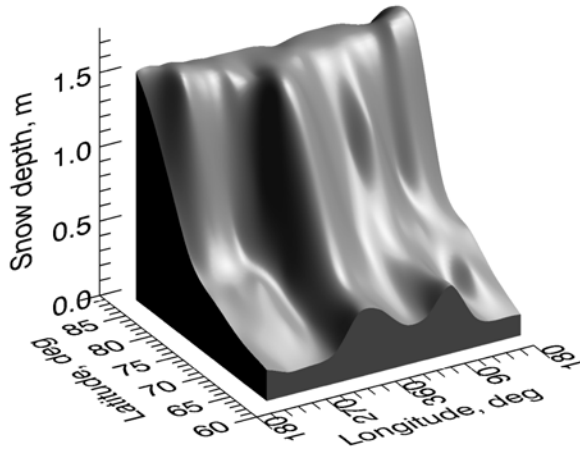


Fig 1a. Map of CO<sub>2</sub> deposit at North region of Mars for Ls=345°.

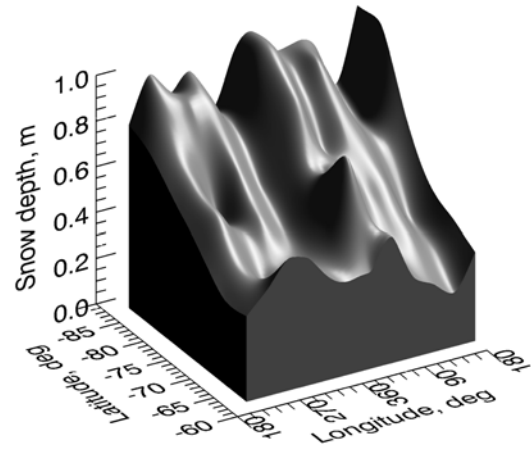


Fig 2a. Map of CO<sub>2</sub> deposit at South region of Mars for Ls=125°.

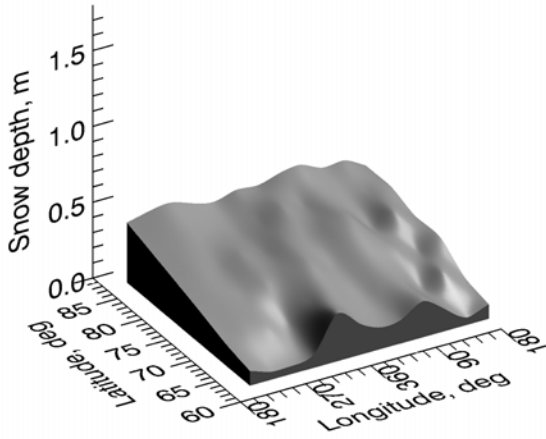


Fig 1b. Map of CO<sub>2</sub> deposit at North region of Mars for Ls=40°.

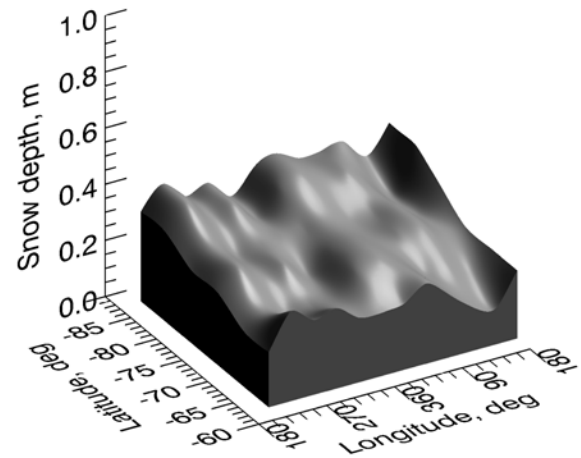


Fig 2b. Map of CO<sub>2</sub> deposit at South region of Mars for Ls=70°.

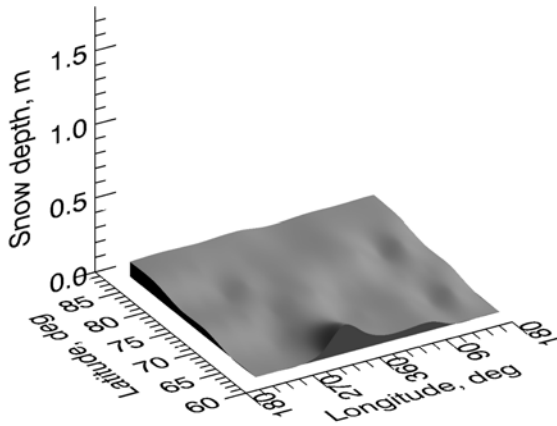


Fig 1c. Map of CO<sub>2</sub> deposit at North region of Mars for Ls=95°.

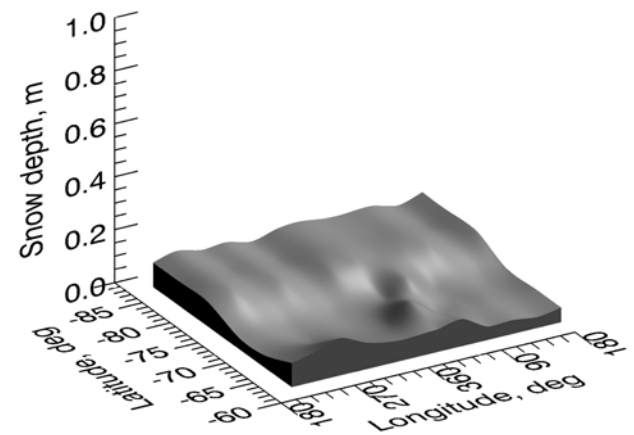


Fig 2b. Map of CO<sub>2</sub> deposit at South region of Mars for Ls=15°.

To take into account scattering and production of epithermal and fast neutrons in the atmosphere the necessary corrections has also been done in this approach. Here we fixed the thickness of atmosphere for each pixel based on CGM prediction at summer period of time. All calculations have been done by help using radiation transport code MCNPX. The soil composition was taken from Mars Pathfinder observation with corrections for surface stones distribution and results obtained with GRS.

The best fit model parameters such as thickness of upper layer, H<sub>2</sub>O content in upper and bottom layers were implemented for the next step to perform estimation of CO<sub>2</sub> frost thickness. Before starting this procedure the whole period of observations was divided into episodes with different Ls to follow the evolution of CO<sub>2</sub> coverage in time. Taking into account that global redistribution of CO<sub>2</sub> mass causes significant changes of Mars atmosphere CGM predictions have been added to program to correct the atmosphere thickness for particular period of time. The final results are presented as time sequence of maps for North and South regions. Some of them are shown on fig 1(a-c) and fig2(a-c).

For the previous martian year there were direct measurements of CO<sub>2</sub> snow depth made at different latitudes by MOLA(MGS). It is good possibility to perform additional calibration of suggested regolith model. We have done comparison between HEND data and MOLA observations for the north latitude belts during the same martian seasons. It was found that there is good correlation between two sets of data[8]. Using obtained results we have checked two-layer model of regolith at north near polar latitudes. It turned out that subsurface of Mars may be described by approximately 75% wt water ice covered by 10-20 g/cm<sup>2</sup> of dry soil at this region. This result is in good agreement with estimations based on HEND data only.

**Conclusions:** The time sequence of maps of CO<sub>2</sub> snow depth were created at north and south regions poleward 60N and 60S latitudes. In fact it presents 4-D model which describes the space distribution of CO<sub>2</sub> frost and its evolution in time between summer and winter seasons. It was found that CO<sub>2</sub> caps on south and north significantly differ from each other. The thickness of CO<sub>2</sub> coverage on the north has achieved maximal values up to 1.5 m which is more than at South pole. It is also observed that the structure of carbonate dioxide deposit on north is more smooth and regular than in South region.

#### References:

- [1] Drake D.M. et al. (1988) *JGR*, V.93, 6353-6368. [2] Feldman W.C. et al. (1993) *JGR*, V.98, 20855-20870. [3] Boynton W.V. et al. (2002) *Science*, 297, 81-85. [4] Mitrofanov I.G. et al. (2002) *Science*, 78-81. [5] Feldman W. C. et al, *Science*, 75-78. [6] Mitrofanov I.G. et al. (2003) *LPS XXXIV*, Abstract # 1104. [7] Smith D.E. et al. (2001) , 294, 2141-2146. [8] Litvak et al. (2003) *LPS XXXIV*, Abstract # 1103. [9] Feldman W.C. et al. (2003) *LPS XXXIV* Abstract # 1854. [10] Mitrofanov I.G. et al. (2003) *this conference*.

**RATIONALE FOR SEISMIC MEASUREMENTS ON MARS BY A SINGLE STATION** Ph. Lognonné and W.B. Banerdt <sup>1</sup>Institut de Physique du Globe de Paris (Département de Géophysique Spatiale et Planétaire, 4 Avenue de Neptune, 94100 Saint Maur des Fossés, France, lognonne@ipgp.jussieu.fr). <sup>2</sup>Jet Propulsion Laboratory, California Institute of Technology (Mail Stop 183-501, 4800 Oak Grove Drive, Pasadena, CA 91109, bruce.banerdt@jpl.nasa.gov),

**Introduction:** We present here some of the scientific objectives which can be achieved by a single seismic station on Mars, equipped with a 3 axis VBB seismometer and a 3 axis Short Period Seismometer [1]. We assume that this station is also equipped with meteorological sensors, including infra-sound and pressure, in order to perform a complete meteorological noise correction. The science objectives are listed in order of increasing difficulty.

**Seismic source localization:** A VBB seismometer will allow the detection of seismic waves in the teleseismic frequency range (0.05-1Hz), for which diffraction effects might be reduced, especially at the lowest frequencies. The determination of the polarization of these waves will therefore be possible, providing the azimuth of the event. Together with the difference of arrival times between P and S waves, it will be therefore possible to determine an approximate epicentral distance and to propose two possible locations. With additional hypothesis on the focal mechanism and on the Martian tectonics, it will be possible to favor one of the two locations. Such information will be crucial for the future landing sites of a Long Lived Network.

**Receiver function:** The crustal thickness is an important parameter for all Martian geophysical models. The joint use of the altimeter and radio-science experiment on MGS allowed the determination of the lateral variations of the Martian crust, but no absolute determination of its volume was possible due to the non-uniqueness of gravity inversions. Indeed, only a seismic determination of the crustal thickness can provide the necessary anchor for such inversions, as demonstrated by recent Lunar models [4].

The receiver method technique is based on a spectral ratio between the vertical and horizontal components. As such, this ratio allows the cancellation of the effect of the seismic source radiation. Moreover, the probable regolith structure on Mars will provide a low velocity zone near the surface, which will straighten seismic rays and reduce therefore the azimuth dependence of the short period data. This method was successfully applied to the Lunar Apollo data [2].

**Local 3D subsurface and crustal structure:** By using the '09 MSL rover, the deployment of explosive active seismic sources might be considered. Alternatively, impactors mounted on the MSL carrier and re-

leased a few days before landing can be used. The activation of these sources can provide a set of seismic profiles, recorded by the Short Period seismometers, which can be used to study the subsurface structure, especially the existence liquid water [3].

Water will affect both the seismic velocities and especially the attenuation of short period seismic waves. Meteorite impacts occurring at a larger distance can also be used, if detected, at longer periods. The isotropic character of the seismic source, polarization of the body waves and travel times of P and S waves can indeed be used to provide a determination of the position of the impact, while Lg and Rg surface waves can be used to constrain the crustal structure.

**Gravity Love number determination:** To measure gravity variations, the very long period gravity output of the seismometer might be used. Due to contamination with the solar thermal effect at the main diurnal and semi-diurnal periods, the Sun tide will not be detected. However, the Phobos-induced tides, of the order of 0.5  $\mu\text{gal}$ , are subdiurnal with typical periods shorter than 6 hours, unrelated to the solar periods. Given the much lower noise level at these periods, they can be accurately measured by the experiment with a stack of about 1 year of data. The measurement accuracies are most likely sufficient to be able to distinguish between different hypotheses concerning the core of Mars, and thus to better constrain the core [5]. For example, the difference between a solid and a liquid core in the main Phobos-induced tide is about 5 times larger than the measurement accuracy, taken here to be 1 nGal, and a change in the gravity signal equal to the accuracy corresponds to a change in core radius of about 60 km

**Free oscillations:** The determination of the free oscillations of Mars allow, without the knowledge of the source position, the determination of the interior structure of the planet [6]. Quakes large enough to excite normal modes are expected at a rate of a few every Martian year and can therefore be detected if a long lived power system is used. These data will provide a precise model of the Martian mantle, especially in term of shear waves.

**Number 5:** In addition to its pathfinder role, the seismic measurement onboard MSL might be a potential number 5 station for a 4-station network, either Netlander, if a launch scenario is found for 2009, or for a future 2011 mission. It can be shown that this 5<sup>th</sup> station will strongly improve the detection efficiency of the network. A 4-station network is able to detect the direct P and S waves generated by quakes, distributed globally on Mars, with an efficiency of ~60%. A 5-station network can achieve an efficiency up to 90%. 50% more events will therefore be useful for the determination of the seismic velocities of the mantle. This improvement is even stronger for the detection of the PKP core-sensitive seismic phases, and allow a doubling of the number of events used in the final inversion of the internal structure. In conclusion, a MSL '09 geophysical station may almost double the science return of a 4-station network for seismology in terms of quake detection, while decreasing by two the risk of failures in the achievement of a network with 3 or more operational stations.

**References:** [1] P. Lognonné, D. Giardini, B. Banerdt, J. Gagnepain-Beyneix, A. Mocquet, T. Spohn, J.F. Karczewski, P. Schibler, S. Cacho, W.T. Pike, C. Cavoit, A. Desautez, J. Pinassaud, D. Breuer, M. Campillo, P. Defraigne, V. Dehant, A. Deschamp, J. Hinderer, J.J. Lévêque, J.P. Montagner, J. Oberst, The NetLander Very Broad band seismometer, *Planet. Space Sc.*, **48**,1289-1302, 2000, [2] Vinnick L, H. Chenet, J. Gagnepain-Beyneix, and P. Lognonné, First seismic receiver functions on the Moon, *Geophys. Res. Lett.*, **28**, 3031-3034, 2001, [3] Lognonne, P., Banerdt, B; Giardini, D; Costard, F, An idea for an active seismic experiment on Mars in 2008, LPI Contribution, Report: 1095, pp.66-67, 2001, [4] P. Lognonné , J. Gagnepain-Beyneix and H. Chenet. A new seismic model of the Moon: implication in terms of structure, formation and evolution, *Earth Plan. Sci. Let.*, 2003, [5] T. Van Hoolst, V. Dehant, F. Roosbeek and P. Lognonné, Tidally induced surface displacements, external potential variations, and gravity variations on Mars, *Icarus*, **161**, 281-296, 2003, [6] Lognonné, P., J. Gagnepain-Beyneix, W.B. Banerdt, S. Cacho, J.F. Karczewski, M. Morand, An Ultra-Broad Band Seismometer on InterMarsnet, *Planetary Space Sciences*, **44**, 1237-1249, 1996.